Surface-wave analysis and its application to determining crustal and mantle structure beneath regional arrays

Ge Jin

Submitted in partial fulfillment
of the requirements for the degree of
Doctor of Philosophy
in the Graduate School of Arts and Sciences

COLUMBIA UNIVERSITY

2015

ABSTRACT

Surface-wave analysis and its application to determining crustal and mantle structure beneath regional arrays

Ge Jin

We develop several new techniques to better retrieve Earth's structure by analyzing seismic surface waves. These techniques are applied in regional studies to understand a variety of tectonic structures and geodynamic processes in Earth's crust and upper mantle.

We create an automated method to retrieve surface-wave phase velocities using dense seismic arrays. The method is based on the notion of using cross-correlation to measure phase variations between nearby stations. Frequency-dependent apparent phase velocities are inverted from the phase-variation measurements via the Eikonal equation. The multi-pathing interference is corrected using amplitude measurements via the Helmholtz equation. The coherence between nearby-station waveforms, together with other data-selection criteria, helps to automate the entire process. We build up the Automated Surface-Wave Measuring System (ASWMS) that retrieves structural phase velocity directly from raw seismic waveforms for individual earthquakes without human intervention. This system is applied on the broad-band seismic data recorded by the USArray from 2006-2014, and obtain Rayleigh-wave phase-velocity maps at the periods of 20-100 s. In total around half million seismograms from 850 events are processed, generating about 4 million cross-correlation measurements. The maps correlate well with several published studies, including ambient-noise results at high frequency. At all frequencies, a significant contrast in Rayleigh-wave phase velocity between the tectonically active western US and the stable eastern US can be observed, with the phase-velocity variations in the western US being 1-2 times greater. The Love wave phase-velocity maps are also calculated. We find that overtone interference may produce systematic bias for the Love-wave phase-velocity measurements.

We apply surface-wave analysis on the data collected by a temporary broad-band seismic

array near the D'Entrecasteaux Island (DI), Papua New Guinea. The array comprises 31 inland and 8 off-shore broad-band seismic sensors, and were operated from March 2010 to July 2011. We adopt the ASWMS to retrieve phase velocities from earthquake signals, and apply the ambient-noise analysis to obtain the Rayleigh-wave phase velocities at higher frequencies. The multi-band phase velocities are inverted for a three-dimensional shear-velocity model of the crust and the upper mantle. The result reveals localized lithosphere extension along a rift-like axis beneath the DI, with a shear-velocity structure similar to an adiabatic upwelling mantle. West of the DI, very slow shear velocities are observed at shallow mantle depth (30-60 km), which we interpret either as the presence of in situ partial melt due to inhibited melt extraction, or as the existence of un-exhumed felsic crustal material embedded within the surrounding mantle.

Love waves contain important information to constrain the upper-mantle radial anisotropy. However, Love-wave fundamental-mode phase-velocity measurements are often contaminated by overtone interference, especially within regional-scale arrays. We evaluate this problem by analytically and numerically evaluating the behavior of synthetic wavefields consisting of two interfering plane waves with distinct phase velocities but comparable group velocities. The results indicate large phase variance due to the interference that can explain the systemic bias observed in data. We develop a procedure that utilizes amplitude measurements to correct for the interference effect. The synthetic tests show the correction can significantly reduce the phase-velocity variance and the bias generated by the interference.

Contents

List of Figures

Page

List of Tables

Page

ACKNOWLEDGMENTS

I always feel fortunate to be able to spend my last five years at Lamont-Doherty Earth Observatory. This has been the best five years in my life: learning from the top scientists in the field, making friends and collaborating with the excellent fellow students from all over the world, enjoying the abundant education resources from Columbia University... From an impudent Chinese student who spoke broken English, to a young scientist who finds the field he loves, I have grown at a speed that even surprises myself.

Special thanks to my advisor Professor James Gaherty, who is a great mentor with patience and an outstanding scientist with keen sense. For years you inspire me when I am confused, guide me when I am lost, remind me when I make mistakes, and praise me when I improve. You lead me to enjoy the fun of exploring the unknown, support me to find my own interest, and teach me how to be a scientist. There are not enough words to express my gratitude. I also thank my other committee members, Professor Geoff Abers and Professor Roger Buck. Geoff teaches me the importance of meticulosity, and provides many helpful suggestions on my projects. Roger helps me to build up the systematic understanding of geodynamic process, and instructs me how to extract the key factors from a complicated system. I would like to say thank you to my other defense committee members: Dr. Ben Holtzman and Professor Colleen Dalton. Ben opens a new artistic world to me in seismology, and helps me to build up the link between seismic observations and rock mechanisms. Colleen helps a lot in our methodology development, and provides me the opportunities of collaboration. Many thanks to Göran Ekström for your patient instructions and insightful comments, to Meredith Nettles for your great suggestions, to Bill Menke for your brilliant ideas, to Philipp Ruprecht for your accompany and instructions in the field. Thank you to Felix Waldhauser, Paul Richards, Spahr Webb, Mark Anders, Won-Young Kim, Einat Aharonov, and all the other staffs at Lamont who helped me to learn. Many thanks to Patty Lin, YoungHee Kim and Mathias Obrebski, whom I have the great pleasure to work with.

I am thankful for my fellow students: Yang Zha, Zach Eilon, Raj Moulik, Anna Foster, Jiyao Li, Natalie Accardo, John Templeton, Claire Bendersky, Mike Howe, Steve Veitch, Celia Eddy, Hannah Robinowitz, Helen Janiszewski, Kira Olsen, and many others... Thank you for the company during

this challenging journey, the encouragement and comforts you give me, the help in organizing the student workshop, the discussions in which we learn from each other, the trips we make together, the parties we all have fun with... Thank you all.

Finally, I would like to extend my deepest gratitude to my family. To my wife, who knows me from childhood, thank you for the years of love and support and understanding. You make me a better person, I cannot image a life without you. Thank you to my parents, for your unconditional love and support. You make me who I am, and I hope I can make you proud.

吾生也有涯，而知也無涯。

以有涯隨無涯，智之始。

My life is limited, while knowledge has no limit.

To use my limited life exploring the unlimited,

that's the beginning of my wisdom.

Chapter 1

Introduction

Earthquakes are like lightning, each strike lighting up the darkness of Earth's interior. Over a century scientists have studied the propagation of the seismic waves, which is the elastic energy released by earthquakes, and used them to explore the deep structures and the dynamic processes of the planet that we all live on.

Among the different types of seismic waves, surface waves draw the attention of many seismologists as the late-arriving phases which usually have the largest amplitude. They propagate along the shallow part of the earth, and carry information about heterogeneities in crust and upper mantle that is complementary to that provided by seismic body waves. Surface waves are dispersed, since different frequencies are sensitive to structures at different depths, which makes it more challenging to quantitatively describe their propagation. They can be measured by different means. One of the most common methods is to estimate phase velocity, the speed at which the phase of each individual frequency varies along the path. The frequency-dependent phase velocities can then be converted into the shear velocities at depth through a non-linear inversion.

Based on the particle-motion direction, surface waves can be divided into two categories: Rayleigh waves and Love waves. Although they sample similar parts of the earth, the structures they each suggest are not always consistent. This so-called Love-Rayleigh discrepancy is an important constraint on the earth's radial anisotropy, which is related to mantle flow pattern, crystal alignment, and melt geometry, among other processes (e.g. *Gaherty*, 2004;

Gaherty and Dunn, 2007; *Holtzman and Kendall*, 2010).

The estimation of surface-wave phase velocity depends on single-station phase measurements. Several techniques have been developed to estimate surface-wave frequency-dependent phase, from utilizing basic Fourier transform (*Forsyth and Li*, 2005), to applying multi-channel narrow-band filters (e.g. *Levshin et al.*, 1992), to cross-correlating the waveform with either synthetic waveforms (e.g. *Gee and Jordan*, 1992; *Ekström et al.*, 1997), or the waveform from another station on the same great-circle path (e.g. *Landisman et al.*, 1969).

The phase variations at stations can then be inverted for two-dimensional phase-velocity maps. At this stage, several methods are developed under different assumptions. The first category of methods is based on the straight-ray theory, in which the phase observations are represented as integral of phase slowness along the source-receiver path (e.g. *Nettles and Dziewoński*, 2008), or between the two stations on the same great-circle path (e.g. *Yao et al.*, 2005; *Foster et al.*, 2014a). The second category attempts to account for ray-bending and finite-frequency effects, which can be substantial for surface waves (e.g. *Evernden*, 1954; *Zhou et al.*, 2005). These methods include the application of arrival-angle corrections to two-station measurements (*Foster et al.*, 2014a), Eikonal tomography (*Lin et al.*, 2009), and finite-frequency kernel estimation (*Zhou et al.*, 2006). The final type of phase-velocity inversion methods utilize amplitude measurements to reduce the multi-pathing interference, including the two-plane-wave method (*Forsyth and Li*, 2005) and the recently developed Helmholtz tomography (*Lin and Ritzwoller*, 2011).

Many of these methods are based on array analysis, which improves our ability to focus on a specific region of interest, regardless of the location of the source. With dense observations, it allows some techniques to increase result resolution by accounting for waveform complexity (e.g. *Forsyth and Li*, 2005; *Lin and Ritzwoller*, 2011). However, array analysis is limited in resolution at long periods due to the finite frequency effect, and it is susceptible to biases associated with limited propagation distances.

The deployment of large, dense arrays has become common in seismic experiments. Substantial amount of data are collected in real time and open to the public. Among the experiments, the Transportable Array (TA) under the USArray program stands out by its data volume and coverage area. The TA project includes more than 400 broad-band seismic sensors deployed with ∼70-km grid spacing, spanning from the west coast to the east to cover the entire US continent. The communication system installed at the sites allows for real-time data collection and archiving. Such a large and growing dataset is ideal for surface-wave analysis, however an automated system is required to accommodate the speed of data growth.

We develop a new technique to meet the challenge in Chapter 2. The Automated Surface-Wave phase-velocity Measuring System (ASWMS) is based on the cross-correlation technique to measure frequency-dependent phase delays between all possible nearby station pairs. Coherence between the waveforms is used to identify low-quality measurements. The measured phase delays, together with single-station amplitude measurements, are then inverted for two-dimensional phase-velocity maps at each frequency.

We successfully automate the entire process. By combining the cross-correlation analysis with an automated data-fetching interface from IRIS Data Service program, we develop a program that can operate by itself and update the US Rayleigh-wave phase-velocity results on a weekly basis. The program has been adopted by IRIS as a data product (`http://ds.iris.edu/ds/products/aswms/`). The phase velocity results, together with the ASWMS, are available for the public to download through the IRIS website.

After the methodology development, we turn our focus to its regional application. In Chapter 3, we apply the surface-wave analysis in the region near the D'Entrecasteaux Islands (DI), Papua New Guinea (PNG). The DI are located at the tip of the Woodlark rifting system, where the continental rift is actively transforming into sea-floor spreading (e.g. *Taylor et al.*, 1999; *Ferris et al.*, 2006). Previous studies show the crust beneath the DI has been thinned by 30-50%, while the body-wave tomography results suggest a upwelling mantle

(*Abers et al.*, 2002; *Ferris et al.*, 2006). The islands expose high-pressure (HP) terranes comprised of several gneiss domes with diameters of 20-30km. These gneiss domes are mostly felsic in composition (quartzofeldspathic), and one bears the youngest-known ultrahigh-pressure (UHP) coesite eclogite (*Baldwin et al.*, 2004, 2008; *Little et al.*, 2011). The HP/UHP rocks have a composition similar to continental crust. The isotropic analysis reveals an exhumation history at plate-tectonic rates (few cm/year) from ∼100-km depth since 5-8 Ma (e.g. *Baldwin et al.*, 2008; *Gordon et al.*, 2012).

The exhumation mechanism of the UHP rocks remains debated, with two competing families of models: low-angle extensional unroofing of previously subducted UHP rocks, perhaps associated with subduction reversal along a paleo-subduction channel (*Hill et al.*, 1992; *Webb et al.*, 2008), and thinning of overlying crust to allow diapiric penetration of buoyant continental rocks to the surface (*Ellis et al.*, 2011; *Little et al.*, 2011).

In order to provide better constrains on the geodynamic process in this area, we deployed 31 land-based and 8 ocean bottom broad-band seismometers, with ∼20-km station spacing, to cover a $2.5^\circ \times 2.5^\circ$ area around the DI. The stations collected seventeen months of data, and the project team has applied a wide range of observational techniques to these data to image crust and mantle structure in the region.

Here we present the surface-wave analysis on these data, which provides a three-dimensional shear-velocity model of the curst and upper-most mantle. We applied ASWMS to 93 teleseismic earthquakes recorded on the array, and obtained phase-velocity maps across the region within the band between 20-60 s period. In order to better constrain the shallow structure, we apply the ambient-noise technique to obtain phase velocities at higher frequencies. The idea of applying cross correlation on ambient noise to recover the green function between two simultaneously recording stations can be traced back as early as *Aki* (1957). It was not until fifty years later that the method became popular because of the availability of dense seismic networks (e.g. *Shapiro et al.*, 2005; *Bensen et al.*, 2007). In the PNG case, we perform the ambient-noise measurements in the frequency domain, following the algorithm developed *Ek-*

ström et al. (2009) and *Ekström* (2013). A new Bessel-function waveform fitting technique is developed to better estimate the phase delays between the stations (*Menke and Jin*, 2015). The phase delays are later inverted for phase-velocity maps using a ray-theory tomography method.

The ambient-noise analysis produces high resolution phase-velocity maps at the 10-17 s periods. Together with the earthquake measurements from the ASWMS, we retrieve the robust phase velocities of Rayleigh waves in a wide frequency range (10-60 s in period), which provide good constraint on the crustal and upper mantle structure down to ∼100 km.

For each grid on the map, the phase-velocity dispersion curve is then extracted to invert for the shear-velocity structure independently, and the individual 1D models are combined together to produce the three-dimensional model. This inversion is non-linear and non-unique (*Herrmann and Ammon*, 2004), and the output can strongly depend on the starting model (e.g. *Foti et al.*, 2009). In order to produce reliable shear-velocity results, we adopt the receiver function results (*Abers et al.*, 2012) to constrain the crustal thickness, apply a grid-search technique to find the best initial models, and use a Monte-carlo like procedure to estimate the starting model dependence. The shear-velocity results show a slow anomaly in the shallow mantle west of Goodenough island, suggesting the existence of un-exhumed continental crust material and/or partial melt.

Although we successfully apply our methods on Rayleigh waves, systematic bias is found in the phase-velocity measurements when the same techniques are applied on Love waves. The bias is mainly generated by overtone interference, which needs to be handled with special care for the Love-wave single-mode measurements (e.g. *Thatcher and Brune*, 1969; *Forsyth*, 1975; *Gaherty et al.*, 1996).

The overtone interference is more acute for Love waves due to the similar group velocities of the fundamental- and higher-mode Love waves, especially for oceanic structures (*Nettles and Dziewoński*, 2011). It can produce large phase and amplitude variations for single-branch measurements. Such variations do not significantly affect long-path measurements, since the

interference pattern is periodical and the bias can be averaged out over the path (*Nettles and Dziewoński*, 2011). But they may introduce large bias in the array-based regional studies which involve the estimation of local phase gradient. In the USArray application, *Foster et al.* (2014b) show that the bias due to the interference is profound at middle-band frequencies (60-150 s), even though the array is located in the center of the continent and only shallow events are selected. Based on the global and the regional observations, *Nettles and Dziewoński* (2011) and *Foster et al.* (2014b) both suggest the bias is mainly controlled by the interference between the Love-wave fundamental mode and its first overtone.

In Chapter 4 we construct a series of synthetic tests to simulate the pattern of overtone interference and its influence on the single-branch phase-velocity measurements. A correction technique that has the potential to correct this bias is developed and tested on synthetic data.

The target of this dissertation is to better retrieve earth's structure from surface waves, so that we can provide more constraint on geodynamic processes. We develop robust and automatic phase-velocity measuring methods for both earthquake and ambient-noise based data. These techniques are successfully applied on the data from USArray and a regional temporary array at the D'Entrecasteaux Islands, Papua New Guinea. Based on the measurement results, we shed light on the effect of thermal and compositional variations on the upper-mantle shear velocities, and the geodynamic process of continental rift extension and UHP rocks exhumation. We also propose a correction scheme that can reduce the phase-velocity bias due to overtone interference in Love-wave studies, so that mantle radial anisotropy can be better constrained.

Chapter 2

Surface-Wave Phase-Velocity Measurement Based on Multi-Channel Cross Correlation

Note: A slightly modified version of this chapter has been submitted to Geophysical Journal International (2014). [1]

Abstract

We have developed a new method to retrieve seismic surface-wave phase velocity using dense seismic arrays. The method measures phase variations between nearby stations based on waveform cross correlation. The coherence in waveforms between adjacent stations results in highly precise relative phase estimates. Frequency-dependent phase variations are then inverted for spatial variations in apparent phase velocity via the Eikonal equation. Frequency-dependent surface-wave amplitudes measured on individual stations are used to correct the apparent phase velocity to account for multipathing via the Helmholtz equation. By using coherence and other data selection criteria, we construct an automated system that retrieves structural phase-velocity maps directly from raw seismic waveforms for individual earthquakes without human intervention. The system is applied to broadband seismic

[1]AUTHORS: Ge Jin[a]*, James Gaherty[a]
[a] Lamont-Doherty Earth Observatory, Columbia University, 61 Route 9W, Palisades, NY 10964, USA
* corresponding author: ge.jin@ldeo.columbia.edu

data from over 800 events recorded on EarthScope's USArray from 2006-2014, systematically building up Rayleigh-wave phase-velocity maps between the periods of 20 s and 100 s for the entire continental United States. At the highest frequencies, the resulting maps are highly correlated with phase-velocity maps derived from ambient noise tomography. At all frequencies, we observe a significant contrast in Rayleigh-wave phase velocity between the tectonically active western US and the stable eastern US, with the phase velocity variations in the western US being 1-2 times greater. The Love wave phase-velocity maps are also calculated. We find that overtone contamination may produce systemic bias for the Love-wave phase-velocity measurements.

2.1 Introduction

Seismic surface waves represent one of the primary means for scientists to probe the structure of Earth's crust and upper mantle. Surface waves provide direct constraints on both absolute velocity and relative velocity variations, and analysis of waves with different periods provides sensitivity to different depths. These velocity variations in turn provide some of the best available constraints on a variety of geodynamic parameters, including absolute and relative variations in temperature, crust and mantle composition, the presence or absence of fluid (melt) phases, and the distribution and orientation of flow-induced mineral fabric. In many cases, however, resolution of these properties is limited by uncertainties in observed surface-wave velocities due to complexity in the seismic wavefield. Because they sample the highly heterogeneous outer shell of the Earth, surface waves often contain waveform complexity (Fig. 2.1) caused by focusing and defocusing effects (often termed scattering or multipathing) that makes measurement of wave velocity uncertain.

In recent years, a number of investigators have developed data-analysis schemes designed to more robustly estimate surface-wave velocities in the presence of multipathing (e.g. *Friederich and Wielandt*, 1995; *Forsyth and Li*, 2005; *Yang and Forsyth*, 2006; *Lin*

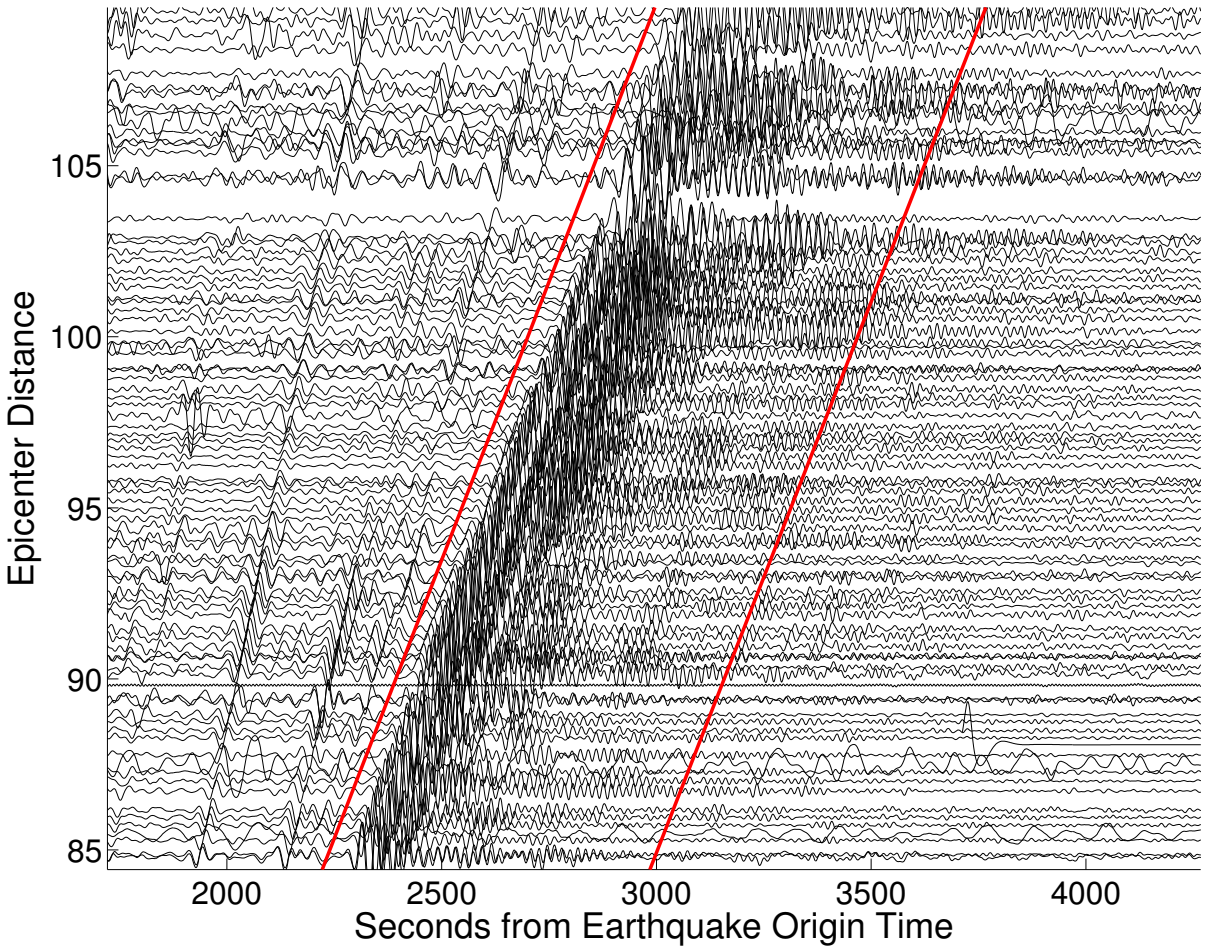

Figure 2.1: USarray vertical component records for the January 18th, 2009 earthquake near Kermadec Islands, New Zealand (Mw=6.4). Red lines show the auto-selected window function W_S to isolate the fundamental Rayleigh wave energy. The variations of the coda length and amplitude indicate the scattering effect caused by lateral heterogeneities.

et al., 2009; *Pollitz and Snoke*, 2010; *Lin and Ritzwoller*, 2011; *Yang et al.*, 2011). These techniques exploit arrays of seismic stations to better quantify the detailed character of the surface wavefield, specifically by combining measurements of both phase and amplitude between stations. These observations can be modeled in the context of wavefield character, for example local plane-wave propagation direction (e.g., *Forsyth and Li*, 2005) or apparent velocities (*Lin et al.*, 2009), as well as the structural phase velocity associated with the underlying media. The techniques are particularly useful for estimating structural velocities in localized regions spanning a receiver array, as opposed to along the entire path from the source to the receiver employed in global (e.g., *Levshin et al.*, 1992; *Li and Romanowicz*, 1996; *Ekström et al.*, 1997) and some regional (e.g., *Chen et al.*, 2007; *Tape et al.*, 2010; *Zhu et al.*, 2012) analyses. The estimates of structural phase or group velocities across the array can then be inverted for models of seismic velocity through the crust and mantle beneath the array, with greater confidence and accuracy than when using phase information alone (e.g., *Pollitz and Snoke*, 2010; *Yang et al.*, 2011; *Rau and Forsyth*, 2011; *Lin and Ritzwoller*, 2011). Among the studies, *Lin and Ritzwoller* (2011) first demonstrate the feasibility of using the Helmholtz equation to improve the accuracy of surface-wave phase-velocity measurements using a dense array.

One of the challenges of the array-based approaches is to efficiently process large datasets that are now available in many regions, with the EarthScope USArray Transportable Array (TA) representing an excellent example. Between 2004 and March 2014, USArray occupied more than 2700 locations with broadband seismic stations that were operated for at least 18 months, and recorded more than 800 shallow earthquakes with magnitude 6 or larger. This large dataset is ideal for surface-wave analysis. Several studies have published surface-wave results based on a subset of this database (e.g. *Yang and Ritzwoller*, 2008; *Pollitz and Snoke*, 2010; *Lin and Ritzwoller*, 2011; *Rau and Forsyth*, 2011; *Bailey et al.*, 2012; *Foster et al.*, 2014a). The communication system installed at the sites allows for real-time data collection and archiving. Such a growing dataset requires an automated system to accommodate the

speed of data growth.

We have developed a new algorithm to accurately and automatically estimate structural phase velocities from broadband recordings of surface waves propagating across an array of receivers. The analysis is based on the notion that waveform cross-correlation provides a highly precise and robust quantification of relative phase between two observed waveforms, if the waveforms are similar in character. This notion is routinely exploited in body-wave analyses for structure (e.g., *VanDecar and Crosson*, 1990) and source (e.g., *Schaff and Beroza*, 2004) characteristics.

In surface-wave analysis, the application of cross-correlation (e.g., *Landisman et al.*, 1969) has been mainly applied between two stations on or close to the same great circle with the earthquake (e.g. *Knopoff et al.*, 1966; *Brisbourne and Stuart*, 1998; *Yao et al.*, 2005). This restriction significantly limits the number of usable measurements, and assuming great-circle propagation can lead to systemic bias in the presence of multipathing and other realistic wave-propagation effects (e.g., *Foster et al.*, 2014a). We avoid these limitations by applying a multi-channel approach, measuring frequency-dependent phase delays between all possible nearby station pairs, without assuming surface-wave propagation following the great-circle path. The measured phase delays form a ideal dataset that can be modelled to retrieve both phase velocities and propagation directions via the Eikonal equation (*Lin et al.*, 2009).

We build our cross-correlation technique upon the Generalized Seismological Data Functional (GSDF) analysis of *Gee and Jordan* (1992), which utilizes cross-correlation between observed and synthetic seismograms to quantify phase and amplitude behavior of any general seismic waveform, including surface waves (e.g. *Gaherty et al.*, 1996). By applying this quantification to cross-correlation functions between surface waves observed at two nearby stations, we generate highly robust and precise estimates of relative phase delay times between the stations, due to the similar nature of the recorded waveforms. The procedure is applicable to arrays across a variety of scales, from the continental scale of EarthScope's TA, to the few 100's km spanned by a typical PASSCAL experiment, to 100's of meters in indus-

try experiments, and is amenable to automated analyses with minimal analyst interaction. The resulting delay times and associated amplitudes can be modeled in the context of both wave-propagation directions and structural velocities via the Helmholtz equation. Here we outline the analysis, demonstrate the automated data processing while applying it on the USArray data (including a brief discussion of the continental-scale phase velocity results), and discuss its comparison to the existing methods. The automated procedure we described here is adopted by IRIS as a data product to provide weekly updated phase-velocity maps of US continent (`http://www.iris.edu/ds/products/aswms/`).

2.2 Methodology

2.2.1 Inter-station phase delays

The methodology is based on the GSDF work flow presented by *Gee and Jordan* (1992), and subsequently utilized for regional upper-mantle and crustal modeling (e.g., *Gaherty and Jordan*, 1995; *Gaherty et al.*, 1996; *Gaherty*, 2001, 2004; *Chen et al.*, 2007; *Gaherty and Dunn*, 2007). In those analyses, the starting point consists of an observed broadband seismogram containing all seismic phases of interest, and a complete synthetic seismogram relative to which the phase delays and amplitude anomalies can be measured. Here, we substitute a seismogram from a nearby station for the synthetic waveform, and measure phase and amplitude differences between phases of interest recorded at the two stations. Waveforms from these two stations are presented as S_1 and S_2 here (Fig. 2.2). Because this is the first application of GSDF to an multi-channel analysis, we summarize the steps in some detail. *Gee and Jordan* (1992) provides a full theoretical presentation of GSDF.

The first step is to isolate the signal of interest in the time domain. In the USArray application, we applied a window function W_S that includes the primary surface wave (Rayleigh on vertical-component record, and Love on the transverse component) and most of its coda. Including the coda is useful, in that it is often highly correlated at stations within

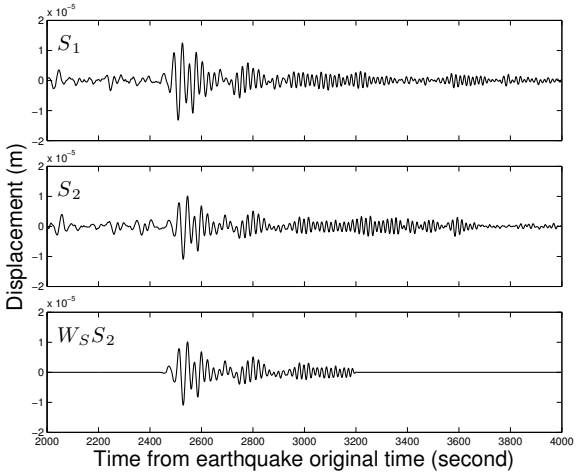

Figure 2.2: Sample waveforms from a nearby station pair for the Kermadec Islands earthquake shown in Fig.2.1. Record S_1 is from the station W17A, and record S_2 is from the station W18A. The two stations are 89 km apart. The third panel demonstrates the effect of window function W_S to isolate the energy of fundamental Rayleigh waves.

1-2 wavelengths, as shown in Fig. 2.2. We then calculate the cross-correlation function $C(t)$ (cross-correlogram) between S_1 and $W_S S_2$, defined as:

$$C(t) = S_1 \star W_S S_2 \tag{2.1}$$

$C(t)$ contains the delay or lag information of all coherent signals, with the peak corresponding roughly to a wide-band group delay between the two stations, with a center frequency defined by the dominant energy in the data, typically around the period of 30 s for teleseismic Rayleigh waves. We further isolate the dominant energy in the cross-correlation function in the time domain by applying a window function W_c around the peak of the cross-correlation function, producing $W_c C(t)$. The window function we apply here has a total length of 300 s with 75s Hanning taper at both ends.

We then isolate the signals of interest in the frequency domain by convolving a sequence of Gaussian, narrow-band filters with $W_c C(t)$, forming a set of filtered correlograms $F_i(\omega_i) * W_c C(t)$, where $F_i(\omega_i)$ corresponds to each filter at center frequency ω_i (Fig. 2.3). These filtered correlograms provide information of the frequency-dependent group and phase

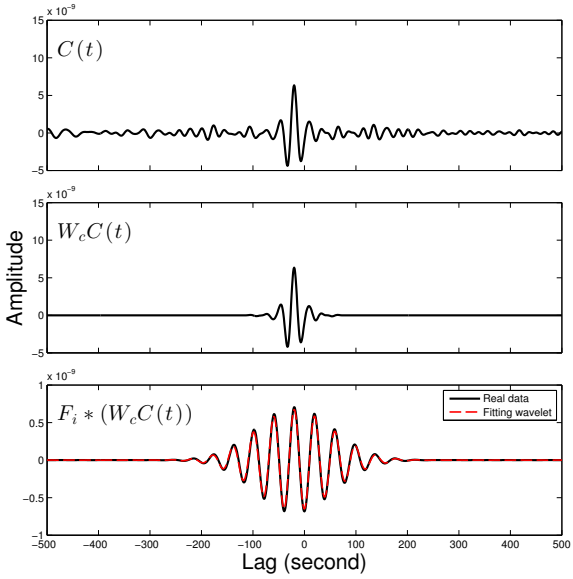

Figure 2.3: The cross-correlation procedures for the station pair shown in Fig. 2.2. Top: the original cross-correlogram. Middle: the windowed cross-correlogram. Bottom: the narrow-band filtered cross-correlogram (40 s) with the five-parameter wavelet.

delays between the two stations, as well as the coherence between the two signals. The frequency-dependent delays provide the fundamental data for determining the phase-velocity characteristics of the wavefield and the structure being sampled. In the application presented here, we are interested in characterizing the phase velocity of fundamental-mode surface waves in the 20-100 s period band, and so we apply a sequence of 8 narrow-band, zero-phase Gaussian filters with a band-width of approximately 10% of the center frequency.

The narrow-band filtered cross-correlation function can be well approximated by a five-parameter wavelet which is the product of a Gaussian envelope and a cosine function:

$$F_i * W_c C(t) \approx AGa[\sigma(t - t_g)]cos[\omega(t - t_p)] \tag{2.2}$$

(*Gee and Jordan*, 1992). In this equation, t_g and t_p represent the frequency-dependent group and phase delays between the two stations, respectively, Ga is the Gaussian function, A is a positive scale factor, σ is the half-bandwidth and ω is the center frequency of the

narrow-band waveform. These parameters are obtained by minimizing the misfit between the predicted wavelet and the observed narrow-band cross-correlogram using a non-linear least-squares inversion.

The raw phase delays are then checked and corrected for cycle-skipping. This is a particular important problem for the higher-frequency observations, and/or for station pairs with relatively large separation, for which the phase delay between the two stations may approach or exceed the period of the observation, and the choice of cycle can be ambiguous. This problem is naturally avoided by only estimating the phase delays between relatively close station pairs. In the USArray application, we only measure station pairs within 200 km, which is less than 3 wavelengths of the shortest period (20 s). As a result, a very rough estimation of reference phase velocity allows for unambiguous selection of the correct phase delay.

The window function W_S may also introduce bias in the measurement, simply by altering the input seismograms at the edges of the window. To account for this, we calculate the cross-correlation between S_2 and the isolation filter, $W_S S_2$.

$$\tilde{C}(t) = S_2 \star W_s S_2 \tag{2.3}$$

$$F_i * W_c \tilde{C}(t) \approx \tilde{A} Ga[\tilde{\sigma}(t - \tilde{t_g})] cos[\tilde{\omega}(t - \tilde{t_p})] \tag{2.4}$$

Since S_2 and $W_S S_2$ are similar within the window of interest, $\tilde{C}(t)$ is similar to the auto-correlation function of $W_S S_2$ with the group delay and phase delay close to zero. Any non-zero phase change corresponds to a delay associated with the windowing process, and by assuming that this windowing delay will be similar for the cross correlation $C(t)$, we calculate a final set of bias-corrected delay times:

$$\delta\tau_p = t_p - \tilde{t}_p \tag{2.5}$$

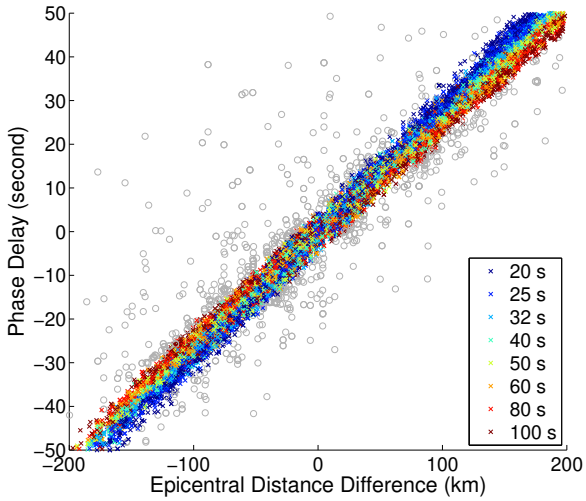

Figure 2.4: Relative phase delays versus epicentral distance difference for all the station pairs with inter-station distance smaller than 200 km, for the Kermadec Islands earthquake. Crosses with different color represent the measurements at different frequencies, and grey circles represent the poor measurements that are discarded as described in Section 2.3.2.

$$\delta\tau_g = t_g - \tilde{t}_g \tag{2.6}$$

As pointed out by *Gee and Jordan* (1992), the windowing function W_c around the peak of the wide-band cross-correlation function may also introduce a bias in the frequency-dependent phase delays. This bias is caused by the center of the window function not coinciding with the actual group delay at each frequency. In this application this bias is generally negligible, since the cross-correlation measurements are only taken between nearby stations, and plus the dispersion in group delay is small.

We perform this phase-delay estimation between a given station and several nearby stations, generally those within 200 km. Fig 2.4 displays the raw phase delays for a representative event recorded across the transportable array. The observed variations are controlled primarily by structural variations beneath the array, and they form the basis for inverting for phase-velocity variations across the array.

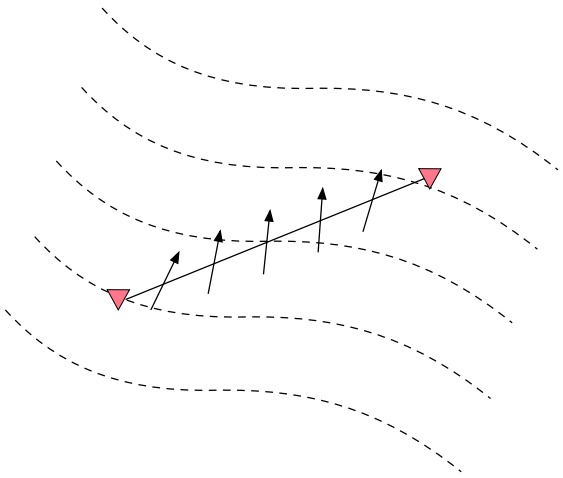

Figure 2.5: Schematic of the slowness-vector inversion. The phase-delay time between any two stations equals to the integral of the slowness vector projected along the link between the stations. Dash lines illustrate wavefronts, red triangles are stations, black line is inter-station link, and black arrows are slowness vectors.

2.2.2 Derivation of apparent phase velocity

For each earthquake and at each frequency, the apparent phase velocity of the wavefield across the array is defined by the Eikonal equation

$$\frac{1}{c'(\vec{r})} = |\nabla\tau(\vec{r})| \tag{2.7}$$

where $\tau(\vec{r})$ is the phase travel time. Also called the dynamic phase velocity, $c'(r)$ is the reciprocal of the travel-time surface gradient, which is close to the structural phase velocity, but will likely be distorted by propagation effects such as multipathing, back-scattering, and focusing of the wavefront (*Lin et al.*, 2009).

The two dimensional network of inter-station phase delays provides a large and well-distributed dataset for estimating the phase gradient via tomographic inversion. Unlike the two-station method, all possible nearby station pairs are measured and used to invert

for propagation velocity across the array, with no assumptions made about direction of propagation. We use a slowness-vector field to describe the propagation of surface waves, with the vector length representing the reciprocal of apparent phase velocity and vector direction representing the wave-propagation direction (Fig. 2.5). The phase-delay time between two nearby stations $\delta\tau_p$ can be described by the integral of the vector field as:

$$\delta\tau_p = \int_{r_i} \vec{S}(\vec{r}) \cdot d\vec{r} \tag{2.8}$$

where $\vec{S}(\vec{r})$ is the slowness vector and $\vec{r_i}$ is the spherical path connecting the two stations. We invert for the two orthogonal components of the slowness distribution (S_R and S_T) as a function of position across the array. S_R follows the great-circle path direction from the epicenter, and is positive in most cases. S_T is orthogonal to S_R with usually a much smaller value, and can be either positive or negative depending on the actual direction of wave propagation. Equation 2.8 can also be written in discrete form as:

$$\delta\tau_p = \sum_i (S_{R_i} dr_{R_i} + S_{T_i} dr_{T_i}) \tag{2.9}$$

where dr_{R_i} and dr_{T_i} denote the projections of the ith segment of the inter-station link on the radial and tangential directions, and S_{R_i} and S_{T_i} are the radial and tangential components of the slowness vector at location i.

The inversion is stabilized by using a smoothness constraint that minimizes the second order derivative of S_R and S_T. The penalty function being minimized can be presented as:

$$\varepsilon_c^2 = \sum \left| \int_{r_i} \vec{S}(\vec{r}) \cdot d\vec{r} - \delta\tau_{p_i} \right|^2 + \lambda \left(\sum |\nabla^2 S_R|^2 + \sum |\nabla^2 S_T|^2 \right) \tag{2.10}$$

where the first term is the misfit between observed and predicted phase delay, and λ is a factor to control the smoothness. The left panels of Fig. 2.7 presents the apparent (Eikonal)

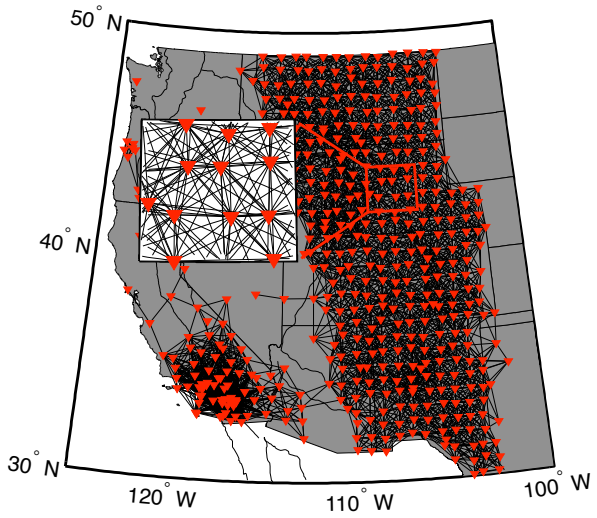

Figure 2.6: Inter-station connections of the slowness-vector inversion for the Kermadec Islands event. Red triangles are station locations and black straight lines are inter-station links, that represent the station pairs with cross-correlation phase delays.

phase velocities determined from the $\delta\tau_p$ data presented in Fig. 2.4, with the station-pair links used in the inversion shown in Fig. 2.6. Here, the phase velocities are inverted on a $0.3°\times0.3°$ grid. We select the weight λ of the smoothing kernel in the slowness inversion based on the estimation of average signal-to-noise ratio and wavelength, which varies at each frequency.

2.2.3 Derivation of structural phase velocity

The bias between apparent phase velocity and structural phase velocity can be corrected by adding amplitude measurements into the inversion, using an approximation to the Helmholtz equation (*Wielandt*, 1993; *Lin and Ritzwoller*, 2011):

$$\frac{1}{c(\vec{r})^2} = \frac{1}{c'(\vec{r})^2} - \frac{\nabla^2 A(\vec{r})}{A(\vec{r})\omega^2} \tag{2.11}$$

Here $c(\vec{r})$ is the structural phase velocity and $A(\vec{r})$ is the amplitude field. The amplitude Laplacian term corrects for the influence of non-plane wave propagation on the apparent

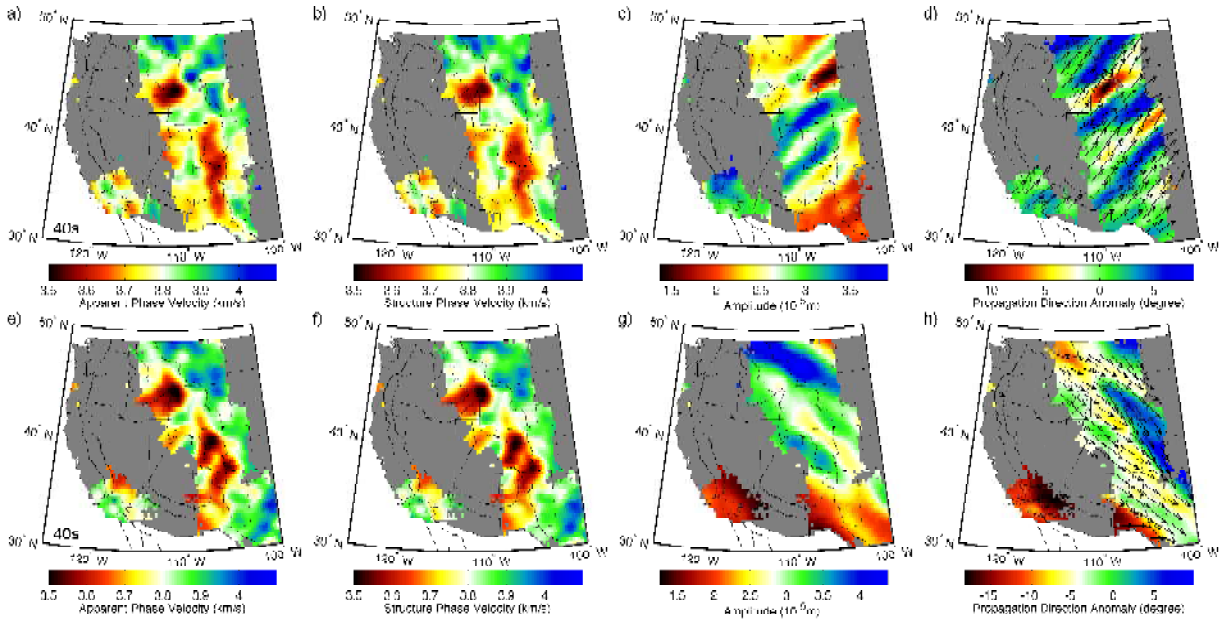

Figure 2.7: The 40-s Rayleigh-wave results of two different events. **a)** The apparent phase-velocity map derived from phase-delay measurements (Fig. 2.4) for the Kermadec Islands event. **b)** The corrected phase-velocity map derived from the apparent phase velocity and amplitude measurements via Helmholtz equation. **c)** The amplitude map. **d)** The map of the propagation direction anomalies. Arrows depict the propagation direction while the colors illustrate the angular difference from the great-circle direction. The rotation of the arrows from great-circle direction is exaggerated for demonstration. **e)-h)** Same as a)-d) but for the April 7, 2009 earthquake near Kuril Islands ($M_s = 6.8$).

phase velocities, allowing for the recovery of the true structural phase velocity (Fig. 2.7). *Lin and Ritzwoller* (2011) applied this formulation to USArray data to explore the seismic structure of the western US.

The associated amplitude of the surface wavefield is estimated using amplitude measurements performed on single-station waveforms. As we have applied the five-parameter wavelet fitting to the windowed and narrow-band filtered auto-correlation function $\tilde{C}(t)$ to remove the windowing effect in Section 2.2.1, the scale factor $\tilde{A}$ of the wavelet is a good approximation of the power spectral density function at the center frequency of the narrow-band filter.

The input apparent phase velocity $c'(\vec{r})$ is derived as in Section 2.2.2 (Fig.2.7a,e). For the amplitude term, we follow *Lin and Ritzwoller* (2011) by fitting a minimum curvature surface to the single-station amplitude estimations (Fig.2.7c,g). The error function for the surface fitting is:

$$\varepsilon_A^2 = \sum_i |A(r_i) - A_i|^2 + \gamma \sum |\nabla^2 A(\vec{r})|^2 \tag{2.12}$$

where A_i is the observed station amplitude at location r_i, $A(r_i)$ is the interpolated amplitude estimated at r_i, and γ controls the smoothness of the surface. In practice, calculating the second gradients of this amplitude field $A(\vec{r})$ is sometimes problematic, as the Laplacian operator magnifies short-wavelength noise, and individual amplitude measurements can be highly variable due to local site conditions and erroneous instrument responses. We utilize a finite-difference calculation to estimate the second derivative numerically, and then one more step of smoothing is performed on the correction term to suppress the short-wavelength noise (see Section 2.5.2 for more details).

The application of the Helmholtz equation implies a consistency between the dynamic phase-velocity and amplitude, which is demonstrated in the right panels of Fig 2.7. In particular, wavefield focusing should produce amplitude variations that are consistent with variations in propagation direction. For the example events shown here, local propagation directions estimated from the apparent phase gradients deviate from the predicted great

circle path by up to ±15 degrees. The regions of wavefield convergence produced high amplitudes as observed in the data, and low amplitudes correspond to regions of wavefield convergence. The spatial correlation of these independent observations provide confidence for application of the Helmholtz correction.

The amplitude correction cannot be simply applied on Love-wave measurements, as the phase and amplitude measurements of Love waves are made on the tangential component based on the great-circle path direction, which is not necessarily the actual particle-motion direction of the propagating Love-wave field. The presence of multipathing wave fields with conflicting polarizations makes the Helmholtz equation invalid. As a result, all the Love wave results discussed in this paper are the results of Eikonal tomography.

In the following section, we present the full application of this analysis to the data from the TA. The analysis up through the calculation of structural phase velocity is done for individual events, at a range of frequencies. For a fixed array geometry, the resulting phase-velocity maps from individual events are averaged (stacked) to produce the final phase-velocity maps that can be used in a structural inversion for shear velocity. In the case of a rolling array such as the TA, stacking and averaging over multiple events produces a single comprehensive phase-velocity map that spans the history of the array deployment.

2.3 Data Processing and Automation

We apply this analysis to the data collected by USArray from January, 2006 to August, 2014. We collect all events with Mw larger than 6.0 and depth shallower than 50 km using the software SOD (*Owens et al.*, 2004). The station locations and event azimuthal distribution are shown in Fig. 2.8. Seismograms are pre-filtered from 0.005 Hz to 0.1 Hz, with instrument response deconvolved to displacement. In total about one-half million seismograms from 850 events are processed, generating about 4 million cross-correlation measurements. This volume of data requires an automated process. Effective automation requires two additional

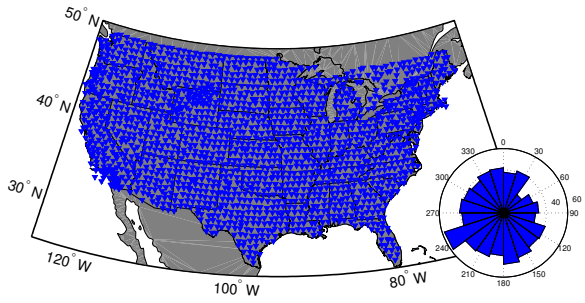

Figure 2.8: Station locations and event azimuthal distribution (insert) from 2006 to 2014.

components to the analysis: the generation of the time window to be analyzed, and a means to evaluate errors and remove outliers.

2.3.1 Auto generation of isolation filter

As the first step of the process, a window function W_S is required to isolate the fundamental-mode energy of the surface waves. The desired window function W_S should be wide enough to include the arrivals of the maximum amplitudes of all frequencies, and narrow enough to eliminate the interference from higher-mode phases and body waves.

To generate this window function, we first estimate the group delays of all the frequency bands at individual stations using the FTAN method (*Levshin et al.*, 1992). The desired time-range to be included for each frequency is two cycles before and five cycles after the group delay. At each station, we select the first beginning and last ending time among these time-ranges of all the frequency bands, and define them as the beginning and ending time of the suggested window function of the station.

We collect the locations of suggested window functions for the entire array, and solve for a linear relation between the time range of the final window function W_S and epicentral distance. The relation is defined as:

$$T_1 = \frac{L}{v_1} + t_1 T_2 = \frac{L}{v_2} + t_2 \tag{2.13}$$

where T_1 and T_2 are the beginning and ending time of W_S, L is the epicentral distance, and v_1, v_2, t_1, t_2 are the parameters estimated by linear regression.

An example of this automated window selection is shown in Fig. 2.1. Alternative window selection algorithms include the use of regional/global group-velocity maps in frequency band of interest, or group-velocity predictions using a regionally appropriate one-dimensional model.

2.3.2 Auto selection of high-quality measurements

We use the coherence between the waveforms of nearby stations as the primary factor to eliminate measurements with low signal-to-noise ratio (SNR) or from dysfunctional stations. The coherence is frequency dependent and can be estimated by comparing the amplitude of cross-correlation function $C(t)$ and two auto-correlation functions $\tilde{C}(t)$. Since we already fit the five-parameter wavelet to those functions, it is convenient to use those fitting results. Coherence at a certain frequency can be written as:

$$\gamma^2 = \frac{A_{12}^2}{\tilde{A}_{11}\tilde{A}_{22}} \tag{2.14}$$

where A_{12} is the amplitude of the narrow-band cross-correlation wavelet estimated in Section 2.2.1, and $\tilde{A}_{11}$ and $\tilde{A}_{22}$ are the amplitudes of the narrow-band auto-correlation wavelet of the two stations estimated in Section 2.2.3. In this study, we exclude all the measurements with the coherence lower than 0.5.

The second round of data selection is performed after the phase-delay measurements from all the station pairs are gathered. We estimate the average phase velocity at each frequency by linearly fitting the phase delays with respect to the difference in epicentral distance, and discard all measurements with misfit more than 10 s relative to the linear prediction. For station pairs less than 200 km apart, this is a weak constraint, removing only those observations with travel-time deviations greater than 20% of the total travel time.

For an example event in Fig. 2.4, this treatment discards 1784 of 41544 total observations for this event, effectively removing most of the extreme measurements and thus stabilizing the Eikonal inversion.

Following the Eikonal inversion described in Section 2.2.2, we reject the measurements with large inversion misfit, which is defined as the difference between the predicted and observed phase delay, and invert for the slowness again. This step removes the inconsistent measurements and enhance the robustness of apparent phase velocity results.

For the amplitude measurements, we discard the stations with amplitude variation larger than 30% of the median amplitude of their nearby stations (<200 km).

2.4 Results

We convert the structural phase velocity maps from individual events into slowness, and then they are weighted and stacked. The weighting of each pixel for each event is based on the ray density in the slowness inversion (Section 2.2.2), and pixels in an individual event map that differ from the stack value by more than two standard deviations are removed. Event maps are utilized only if the number of high-quality, qualified observations exceed a minimum threshold, and we discard events with mean phase velocity that differs by more than 2% of the existing stacked result for the same region. Only the pixels averaging more than 10 events are shown in the maps. After stacking, the phase-velocity maps are further smoothed, with the smoothing length being a quarter of the average wavelength at each frequency. We focus here on the Rayleigh-wave observations; we also calculate maps for Love waves, but they are not shown, pending further analysis of apparent higher-mode contamination.

2.4.1 Phase-Velocity Variations across the Continental US

The Rayleigh-wave phase-velocity maps in eight frequency bands are shown in Fig. 2.9. Surface waves at a particular frequency are sensitive to the shear velocity structure over

a range of depths, thus the phase-velocity anomalies cannot be directly interpreted as the shear-velocity variations at a specific depth. However, higher-frequency Rayleigh waves sample shallower structures, with the depth of maximum sensitivity being roughly one-third of the wavelength.

In the western US, large phase-velocity variations outline the major geological structures. Near the Yellowstone hotspot, high temperatures and the possible presence of partial melt are suggested by a strong slow anomaly in all bands. At the adjacent Snake River Plain, the slow anomalies diminish at high frequencies, perhaps due to the faster crustal velocity associated with basaltic volcanism (e.g., *Sparlin et al.*, 1982; *Peng and Humphreys*, 1998). At low frequencies, slow anomalies suggest the existence of high temperature source and possible partial melt in the upper mantle (e.g., *Saltzer and Humphreys*, 1997). A similar trend of phase velocity variations (fast at high frequency, slow at low frequency) is observed in the northern Basin and Range, where the crust is thinned due to the Cenozoic extension (e.g., *Zandt et al.*, 1995), and the existence of high temperature and partial melt in the upper mantle is suggested by the surface heat flow measurements (e.g., *Lysak*, 1992) and basalt chemistry (e.g., *Gazel et al.*, 2012). The deep crustal roots of central and southern Rocky Mountains produce slow anomalies at high frequencies. At low frequencies, as the effect of the thick crust diminishes, the slow anomalies shift to the south, where they are associated with the lithospheric thinning beneath the Rio Grande Rift (e.g., *Gao et al.*, 2004). The Colorado Plateau is collocated with relative fast phase velocities compared to the surrounding regions at all frequencies. This is consistent with the reported faster shear velocity in the crust (e.g., *Bailey et al.*, 2012), and a thick lithosphere supporting the plateau (e.g., *Lee et al.*, 2001). Even at this continental scale, the impingement of low shear velocities into the plateau interior suggests a progressive thermal erosion or destabilization of the edge of the plateau (e.g., *Roy et al.*, 2009; *Levander et al.*, 2011).

The phase velocities in the eastern US are in general 3-5% higher than those in the western US. However, the magnitudes of the velocity variations are noticeably smaller. At

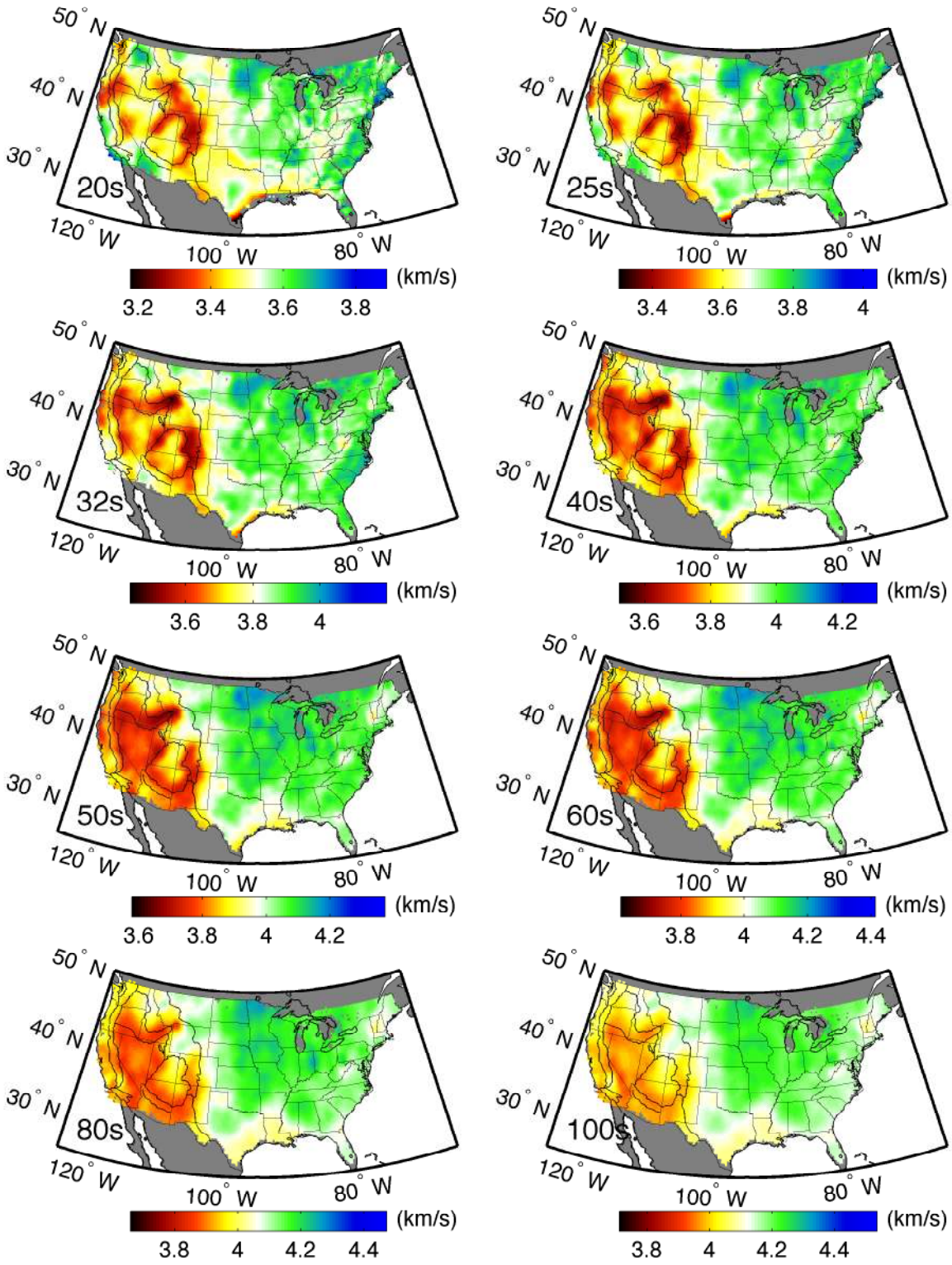

Figure 2.9: Rayleigh-wave phase-velocity maps at different periods, with 850 events stacked.

low frequencies, the slow anomaly beneath the New England region suggests thin lithosphere underlain by warmer mantle (e.g., *Li et al.*, 2002; *Gaherty*, 2004; *Rychert et al.*, 2005). At high frequencies, extremely slow anomalies are observed along the coastline of the Gulf of Mexico, which is attributed to the thick sedimentary layer along the coast (*Laske and Masters*, 1997). The Mid Continent Rift and the Appalachian Highlands are associated with slow anomalies at high frequencies, which probably reflect thickened crust in these two regions (*Crotwell and Owens*, 2005; *Shen et al.*, 2013a; *Parker et al.*, 2013), while the Northern Atlantic Coastal Plain is colocated with fast anomalies, perhaps indicating thin crust (*Crotwell and Owens*, 2005). Most of these anomalies diminish at periods longer than 40 s, indicating that little thermal variations in the mantle remain associated with these long-lived geologic structures.

In order to better quantify the apparent contrast in the amplitude of the phase-velocity variations between the tectonically active western US and the stable eastern interior, we apply a 2D Fourier spectral analysis on the Rayleigh-wave phase-velocity maps. Using an approach similar to *Chevrot et al.* (1998), the Fourier transform is performed on sinusoidal map projections centered at $(40.5°, -113°)$ and $(38°, -90°)$ for the western and eastern US respectively (Fig. 2.10a). We apply a minimum curvature surface interpolation of phase velocity to fill the empty space, and then subtract the average phase velocity of each area to focus on the velocity variations. The 2D amplitude spectra are then plotted for each period in both regions for all spatial scales larger than the nominal surface-wave wavelengths at that period (Fig. 2.10b).

The spectra of both western and eastern areas (Fig.2.10b) indicate a linear increase in the amplitude of heterogeneity with wavelength, which is consistent with global studies at a larger scale (*Chevrot et al.*, 1998; *Dziewoński et al.*, 2010). This result also agrees with predicted spectrum of heterogeneities from numerical models of fluid convection (e.g., *Batchelor*, 1959; *Antonsen and Ott*, 1991; *Ricard et al.*, 2014), which suggest that the 1D power spectrum of the heterogeneities in any direction varies at $1/k$, where k is the wavenumber. This is

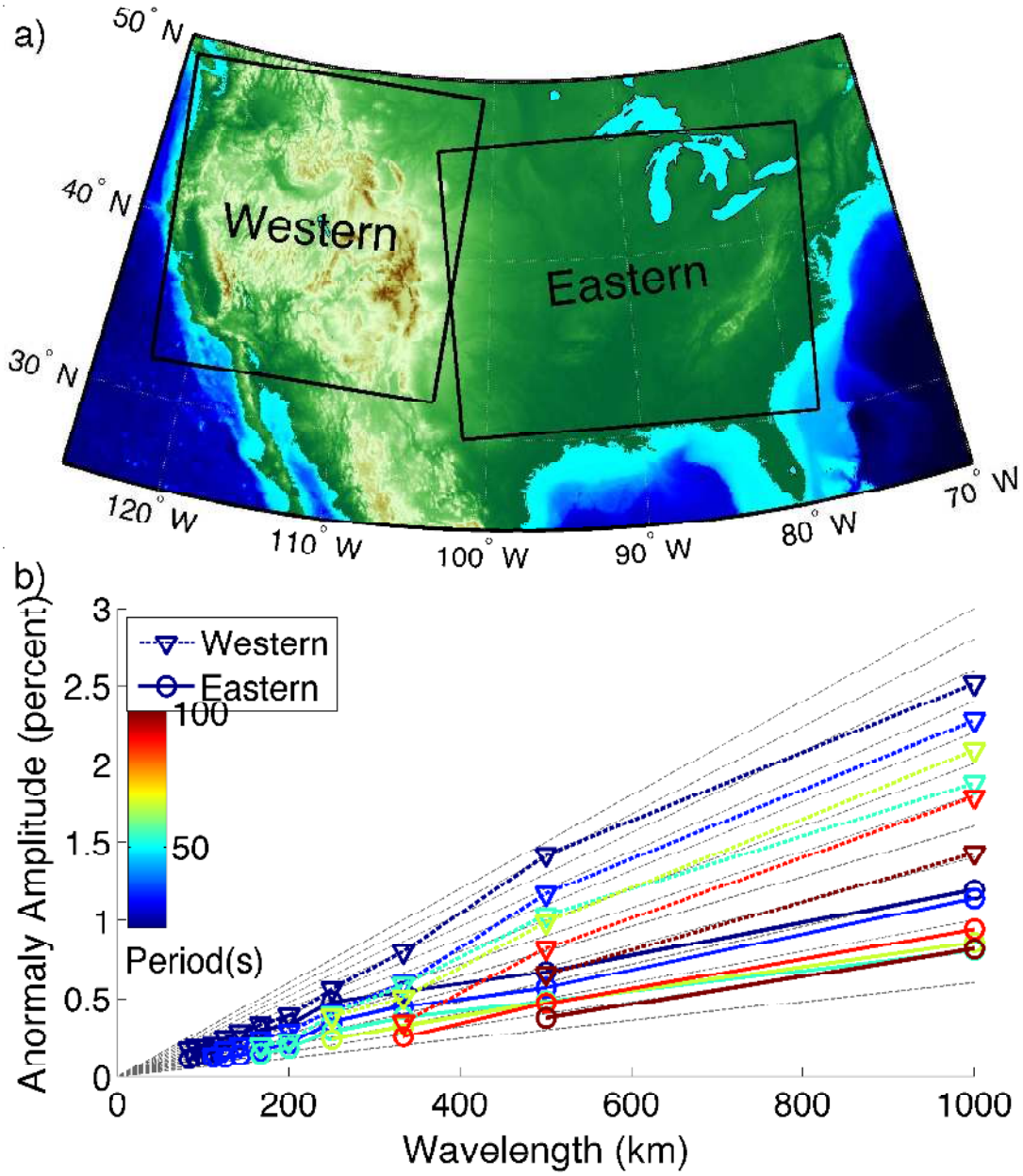

Figure 2.10: 2D spectral analysis of the Rayleigh-wave phase-velocity maps. **a)** The definition of the western and eastern US areas. **b)** The amplitude of phase-velocity variations versus the structural wavelength at different periods. Only the structural wavelengths larger than the Rayleigh-wave wavelengths are plotted at each period. The gray dash lines in the background show the predicted $1/k$ dependence of the heterogeneity strength by thermal convection models (e.g., *Ricard et al.*, 2014).

equivalent to a $1/k^2$ variation for 2D power spectrum (*Chevrot et al.*, 1998), or $1/k$ variation for 2D amplitude spectrum, as what we show in this study.

In the western US, the variation amplitudes measured at the shortest periods (20 s and 25 s) are in general much stronger than the variation amplitudes at longer periods. This trend is visible but less obvious in the eastern US. These two frequency bands are highly sensitive to the structure of continental crust, and we interpret this trend as indicating a greater degree of velocity heterogeneity and thickness variation in the crust. Specifically, the velocity heterogeneity likely arises due to the large variation in velocity of common crustal lithologies (e.g., *Christensen and Mooney*, 1995), and the rough topography of Moho in the western US (*Shen et al.*, 2013b).

In the eastern US, some Moho depth variations larger than 10 km are reported across various tectonic regions (e.g., *Li et al.*, 2002; *Shen et al.*, 2013a; *Parker et al.*, 2013), but in general they are smaller than those observed in the western US (e.g., *Crotwell and Owens*, 2005; *Shen et al.*, 2013b; *Levandowski et al.*, 2014). In addition, the density and shear velocity of old orogen crustal roots may increase with greater age due to cooling and metamorphic reaction (*Fischer*, 2002). This would decrease the velocity contrast between the crustal roots and the underlying mantle, and hence reduces the magnitude of phase-velocity variations.

At that periods most sensitive to mantle structure, the variation amplitudes in the western US are 1-2 times greater than those in the eastern US at most spatial wavelengths. These phase-velocity variations are most likely dominated by variations in temperature (e.g., *Priestley and McKenzie*, 2013; *Dalton et al.*, 2014), which are significant in the western US. Ancient orogenic structures in the east (e.g., mid-continent rift system, Grenville Oregon, Piedmont plateau) likely had large temperature heterogeneity in the past, but thermal diffusion has reduced these variations over time. There is some evidence that at the highest-velocity end of the heterogeneity spectrum, compositional structure contributes significantly to observed shear-velocity variations in stable cratonic lithosphere (*Dalton et al.*, 2009). It is likely that such structure contributes to the phase-velocity variations observed in the eastern portion

of the continent.

2.4.2 Comparison with other studies

Comparison with ambient noise results

Micro-seismic ambient noise has been widely used to retrieve surface-wave phase velocity at high frequencies (e.g., Bensen et al. 2007). We compare the highest frequency earthquake phase-velocity results from this study with the ambient noise phase velocities estimated by *Ekström* (2013). These ambient noise results are also the output of an automated system, which downloads the continuous waveform data, estimates and stacks the normalized coherence, retrieves phase delays between station pairs in the frequency domain (*Ekström et al.*, 2009), and produces phase velocity maps using ray theory. The results are regularly updated and can be downloaded from the author's website (`http://www.ldeo.columbia.edu/~ekstrom/Projects/ANT/USANT12.html`).

Fig. 2.11 depicts the comparison for Rayleigh waves and Love waves at a period of 20 s. The results are highly consistent, despite that they are retrieved from different seismic sources by using different phase measurement techniques and velocity inversions. Strong geological features are clearly highlighted in both results. The largest inconsistencies (Fig 2.11c and f) are localized on the edges of the model space, which are the least-well resolved regions in both models. There are also localized differences near major geological boundaries (e.g. the edge of the Sierra Nevada), which may result from different smoothness constraints in the two approaches.

For Rayleigh waves, the correlation coefficient between the two maps in Fig. 2.11 is 0.95. The mean and the standard deviation of the velocity difference are 0.007 km/s and 0.030 km/s, respectively. The small but systemic difference shows slightly higher velocities (0.2%) from this study (Fig. 2.12), which we interpret as the influence of the ray-bending effects, as the Helmholtz tomography allows for ray bending while conventional ray theory does not. A similar amount of discrepancy is reported by *Lin et al.* (2009) when comparing the

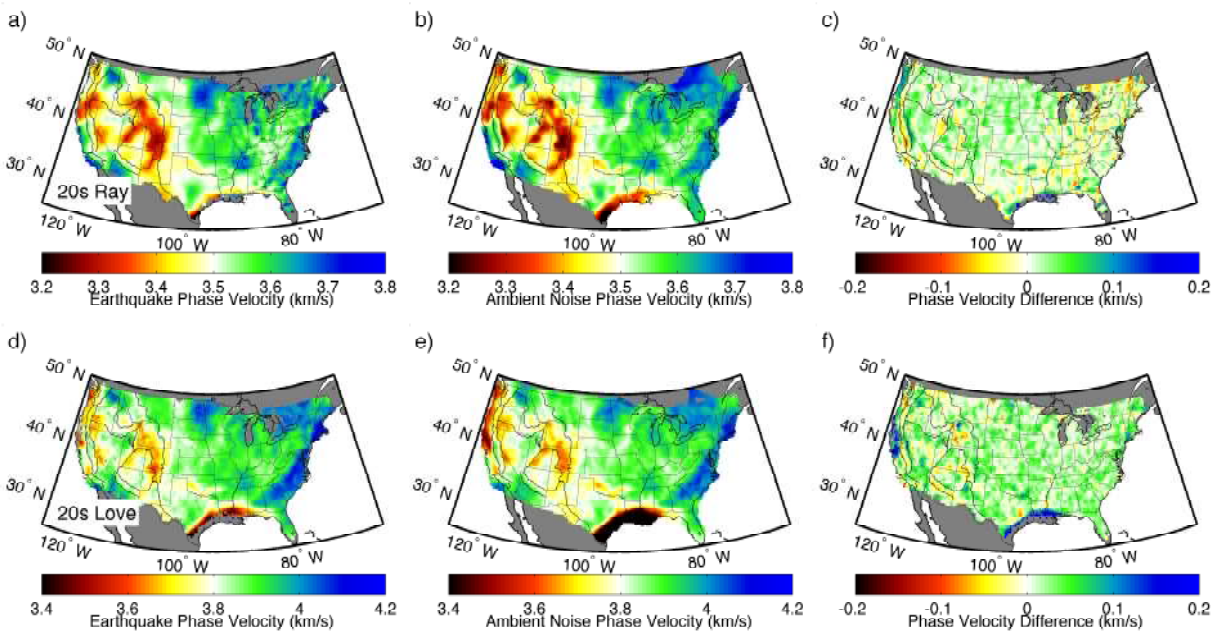

Figure 2.11: Comparison of 20-s Rayleigh and Love wave phase-velocity maps derived from earthquakes (this study) and ambient noise (Ekström 2013). **a)** The earthquake result. **b)** The ambient noise result. **c)** The subtraction of b) from a). **d)-f)**: Same as a)-c), but for Love waves.

straight-ray and Eikonal tomography results using ambient noise measurements.

The Love wave results are usually less robust because of the higher noise level in the horizontal components. Nevertheless, the correlation coefficient between the two studies is 0.93. The mean and the standard deviation of the velocity difference for Love waves is 0.019 km/s and 0.043 km/s, respectively. The mean difference (0.5%) is almost triple the value of the difference in the Rayleigh wave results.

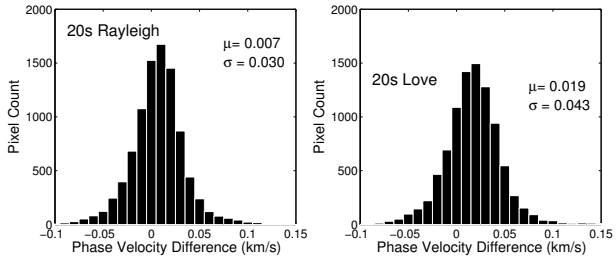

Figure 2.12: Histograms of phase velocity difference between the maps shown in Fig. 2.11.

We also compare the results at two longer periods (25 s and 40 s). The means of the differences are summarized in Fig. 2.14. For Rayleigh waves, we find the difference between the two studies are small. The correlation coefficients range from 0.971 to 0.982 with slightly increase with period. For Love waves, on the other hand, the systemic bias between the earthquake and the ambient noise measurements increases significantly with period, from 0.5% at 20 s period to 2% at 40 s period. The correlation coefficient drops from 0.925 at 20 s period to 0.888 at 40 s period. We suspect that this bias is mainly controlled by overtone interference, which is discussed in more detail in Section 2.4.3.

Comparison with other earthquake results

We further test our results with comparing them to published phase-velocity maps derived from earthquake-generated surface-waves traversing USArray's TA. *Lin and Ritzwoller* (2011) derive phase-velocity maps for the western US from 40-80 s period by applying Helmholtz tomography to single-station phase measurements made using FTAN. *Foster et al.* (2014a) produce phase-velocity maps for the western US spanning 25-100 s period using a modified two-station approach, where the array observations are used to estimated and correct for off-great-circle propagation. In their case the underlying single-station phase measurements are made using *Ekström et al.* (1997).

Fig. 2.14 and 2.13 present several comparisons between our results and these two models. Fig. 2.14 summarizes mean velocity difference between our maps and *Foster et al.* (2014a) at 25, 32, and 40 s, across the similar band spanned by *Ekström* (2013). The Rayleigh-wave results show a high degree of consistency among the studies, with the mean of the difference between them close to zero and correlation coefficient greater than 0.9. The frequency-dependent systematic bias of the Love-wave results indicates the effect of higher-mode interference. This consistency is visually apparent in map form (Fig. 2.13), and extends to long period. At 60-s period (Fig. 2.13a, b), the comparison with *Lin and Ritzwoller* (2011) is excellent, with a correlation coefficient between the two maps of 0.97. At 100-s period

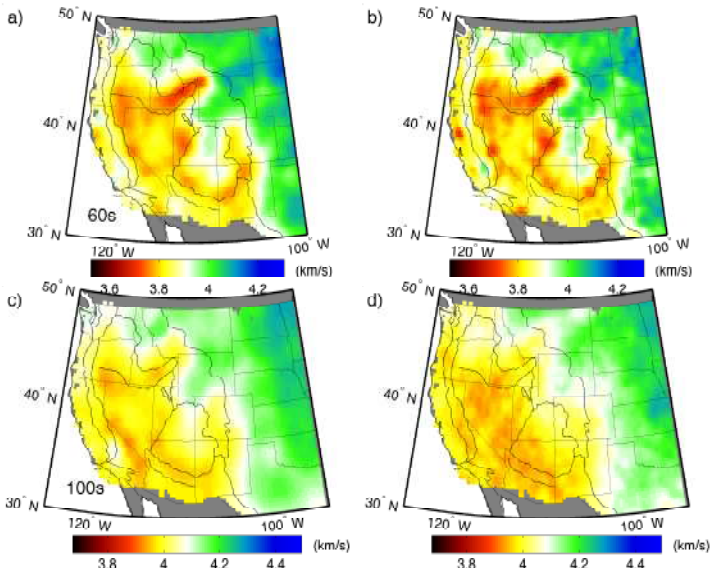

Figure 2.13: Comparison with other earthquake studies at intermediate and long periods. a) 60-s phase-velocity map from this study. b) 60-s phase-velocity map from *Lin and Ritzwoller* (2011). c) 100-s phase-velocity map from this study. d) 100-s phase-velocity map from *Foster et al.* (2014a).

(Fig. 2.13c, d), the correlation with *Foster et al.* (2014a) is 0.96. Subtle differences in the strength and delineation of individual velocity anomalies are visually apparent between the models, which are likely related to different choices of stacking and smoothing in the modeling. These choices are discussed further in Section 2.5.

2.4.3 Possible Source of Error

Station Terms

Although the automated data selection techniques described in Section 2.3 are able to eliminate most of the poor measurements with low SNR, they are not able to distinguish the stations with a time-shift problem or an abnormal amplification term, as the waveforms of those stations may still correlate well with their neighbors.

A station time-shift can be generated either from clock malfunction or from the incorrect instrument response. If the error is large, the observations can be detected and discarded by the misfit check described in Section 2.3.2. The stations with smaller timing errors can be

distinguished in the apparent phase-velocity maps by the appearance of two short-wavelength anomalies with reversed polarization, located before and after the station in the direction of wave propagation. Those stations can be manually identified and excluded. In general, such errors are not significant in the Transportable Array, and we do not perform this manual selection in this study.

The station amplification, on the other hand, is more unavoidable and with less obvious impact compared to the time-shift problem. The amplitude correction we apply in Section 2.2.3 is based on the assumption that all the stations have the same amplification term, which is not perfect due to variation in local geological structure and installation conditions. The ideal way to eliminate this bias is to first estimate the station amplification by averaging multiple events (*Eddy and Ekström*, 2014), or to invert the phase velocity (include focusing/defocusing terms) and amplification term iteratively *Lin et al.* (2012). However, the amplification term of most stations in the USArray is very close to 1 (*Eddy and Ekström*, 2014), and variation in amplification is generally much smaller and more heterogeneous than the smooth amplitude variations associated with focusing and defocusing. As a result, their influence on the final results of this study is minor.

Azimuthal Anisotropy

Lin et al. (2011) report the existence 1-2% of Rayleigh wave azimuthal anisotropy across our frequency range in the western and central US, by using the amplitude correction to further improve the accuracy of the azimuthal-anisotropy estimates. While this anisotropy almost certainly reflects true structural properties in the crust and upper mantle, accurately estimating anisotropic variations adds significant complexity to the 2D inversion. Our goal in this study is determine isotropic phase-velocity maps, and we assume that we can ignore anisotropy due to our well-distributed azimuthal distribution of events (Fig. 2.8). We test this assumption by performing an identical set of phase-velocity inversions, where we include an estimate of azimuthal anisotropy by fitting the structural phase velocity with the wave

propagation direction obtained in the slowness inversion. We compare the isotropic part of the azimuthally anisotropic phase velocity models with original isotropic models presented in Fig 2.9, and find the difference is smaller than 1% for 95% of the grids, with the median value of 0.4%. These small discrepancies are likely caused by the uneven distribution of source back-azimuth in some area, and are negligible in this study.

Overtone Interference

We do not observe any significant effects of higher-mode interference on the Rayleigh-wave phase-velocity maps, as no significant bias is found between the earthquake and the ambient noise results (Fig. 2.14). The source of ambient noise is usually believed to be shallow, and therefore the amplitudes of overtones are relatively smaller in the ambient noise waveforms than in the earthquake waveforms. By assuming the ambient noise results being overtone-free, the consistency between the earthquake and the ambient noise result for Rayleigh waves indicates that the effect of overtone interference is small.

For Love waves, the effect of overtone interference on the phase measurement is more significant than for Rayleigh waves, as the difference in the group velocities between the Love-wave fundamental mode and the first few overtones is smaller. We attempt to minimize overtone interference by limiting the analysis to shallow events (<50 km), but the comparison between the earthquake and the ambient noise results still shows a significant frequency-dependent bias (Fig. 2.14).

In a recent analysis of surface-wave propagation across the TA, *Foster et al.* (2014a) reported a systematically higher phase velocity obtained over short paths from a mini-array velocity analysis (similar to Eikonal tomography) compared to a long-path two-station method (which is shown in Fig. 2.14). The bias they found for the 50-s Love wave has a similar magnitude to what we observed for the 40-s Love waves. A follow-up study (*Foster et al.*, 2014b) suggested that the overtone interference biases phase-velocity estimates derived from local phase-gradient measurements more than those using long ray-path measurements, and the

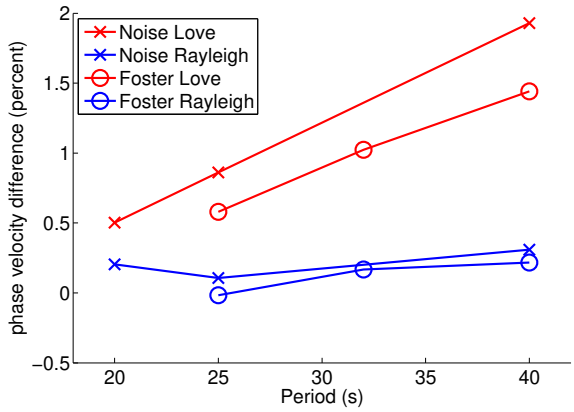

Figure 2.14: The mean phase-velocity difference between this study and the ambient noise results of Ekström (2013) (cross markers) and between this study and the earthquake result of *Foster et al.* (2014a). Rayleigh-wave results show good agreement among the models, while Love-wave results display a systemic bias increasing with period.

bias generated by this influence can be systematic.

The group velocities of the Love wave fundamental mode and the first mode behave differently in the oceanic and continental structure (*Nettles and Dziewoński*, 2011). In oceanic lithosphere, these two modes propagate at a very similar speed, so it is difficult to distinguish them in the time domain (*Gaherty et al.*, 1996) . In continents, the group velocity of the fundamental mode drops dramatically at shorter periods (<50 s), while the group velocity of the first mode remains high. In general, for the continental stations, the time difference between the group delays of the fundamental mode and the overtones is largest at higher frequencies, so interference should be minimal there. This interpretation is consistent with the observations that the bias between the earthquake and ambient-noise results increases with period (Fig. 2.14).

Because the Love wave results are contaminated by overtones interference and hence systematically biased, they are not presented further in this paper. Measuring Love wave phase velocity in the presence of overtone interference will be the subject of a future manuscript.

2.5 Discussion

With the increasing availability of broad-band data from wide-aperture arrays, surface-wave phase-velocity maps are used more than ever for investigating crustal and upper-mantle structure at a variety of scales. Much of the expanded interest has been driven by the development of new analysis techniques that provide robust estimates of structural phase velocity from both ambient noise (e.g., *Ekström*, 2013) and ballistic surface waves, even in the presence of significant multipathing (e.g., *Forsyth and Li*, 2005; *Lin and Ritzwoller*, 2011). These tools have been developed in large part to exploit the capabilities of the latest generation of 2D arrays, but they are likely leading to an expansion of available array data from around the globe, as more scientists recognize the value of surface waves for regional (e.g. PASSCAL) structural experiments, and they design their arrays accordingly.

The analysis presented here has a number of similarities to established methodologies for estimating phase velocity from earthquake data in the presence of multipathing. Our motivation for pursuing this particular approach is to exploit two strengths of waveform cross-correlation: it provides a highly precise means to estimate velocity within an array, and it can be applied with minimal analyst intervention, making it particularly useful for large datasets such as the USArray. In developing this method, we explored a number of options for several of the processing steps, including options that are utilized in other techniques, and we present a brief discussion of these issues here.

2.5.1 Comparison to FTAN phase measurement

The Frequency-Time Analysis (FTAN) method (*Levshin et al.*, 1992) is widely used to make phase- and/or group-velocity measurements from single-station surface-wave seismograms in many global or regional surface-wave studies (e.g., *Levshin et al.*, 1992; *Levshin and Ritzwoller*, 2001; *Yang et al.*, 2011; *Lin and Ritzwoller*, 2011). This method applies a sequences of narrow-band filters to the raw seismograms, and retrieves the group delay at each frequency

by tracking the arrival time of the envelope-function maximum. The phase and amplitude measurements are then made at these amplitude maximums for later tomographic inversion. When made at several individual stations within a seismic array, these measurements can be combined to produce inter-station phase delays that should be directly comparable to those made via cross-correlation, but in practice they differ in two ways.

First, the two methods exploit different techniques to retrieve phase: this study performs cross-correlation on coherent signals between stations to obtain the relative phase variation, and the FTAN method applies a Hilbert transform to single-station waveforms to retrieve absolute phase values. Cross-correlation can suppress the influence of random noise, which is not coherent among the stations, and therefore provides more robust measurements from seismograms with relatively low SNR (e.g., *Landisman et al.*, 1969). This can be demonstrated by a simple synthetic test, in which a narrow-band wavefield is simulated by a cosine function enveloped by a Gaussian function, propagating with a group velocity of 3.7 km/s and a phase velocity of 4.0 km/s. We add normally distributed random noise to each synthetic wavelet, with a standard deviation of 20% of the wavelet's maximum amplitude. We then measure the phase velocity between 500 station pairs with a station spacing of 50 km along the ray path using both methods. The results (Fig. 2.15) show that under the same noise level, the standard deviation of the cross-correlation measurements is significantly smaller (50%) than that of the FTAN measurements. In practice, analysts utilizing FTAN can apply SNR criteria to reduce the sensitivity to high random noise levels, but cross correlation reduces the need for such analyst intervention.

Second, the two methods are sensitive to different portions of data. The FTAN method only samples the waveform near the group delay at each frequency, where the surface waves have their largest SNR. At high frequencies, multiple local maxima with similar amplitude may exist within the envelope due to strong scattering (Fig. 2.16), and selecting inconsistent wavelets across the array may introduce bias into the later phase-velocity inversion. In contrast, the cross-correlation captures the entire surface-wave package, including the coda

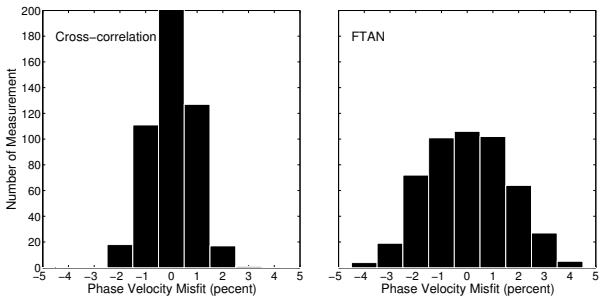

Figure 2.15: Comparison between the cross-correlation measurements and the FTAN measurements in a synthetic test. Left panel: the histogram of the phase-velocity misfit using the cross-correlation method on 500 independent measurements with a 20% noise level. Right panel: the misfit of FTAN measurements of the same dataset.

generated by heterogeneity along the ray path. The phase measurement includes coherent multipathing wavelets, which can be corrected using the amplitude measurements to obtain structural phase velocity. In practice, our method can retrieve robust phase velocities at a period as short as 20 s from teleseismic earthquake data. However, one downside to the cross-correlation algorithm is that the use of a single long broadband window may result in more significant overtone contamination for Love waves, as discussed in Section 2.4.3.

Fig. 2.17 compares the two methods using the data of a real earthquake. Fig. 2.17a is the apparent phase-velocity map for a 60-s Rayleigh wave produced using the algorithm described in *Lin and Ritzwoller* (2011), which corresponds to fig.4a of their paper. In Fig. 2.17b, we replace the FTAN phase measurements with our cross-correlation measurements and keep the velocity inversion the same as Fig. 2.17a. The technique to calculate the travel-time surface from multi-channel phase-variation measurements can be found in Section 2.5.3. The comparison between the two plots indicates that our method reduces short-wavelength heterogeneity in apparent phase velocity, most likely due to more stable measurements at low-amplitude stations compared to the FTAN method.

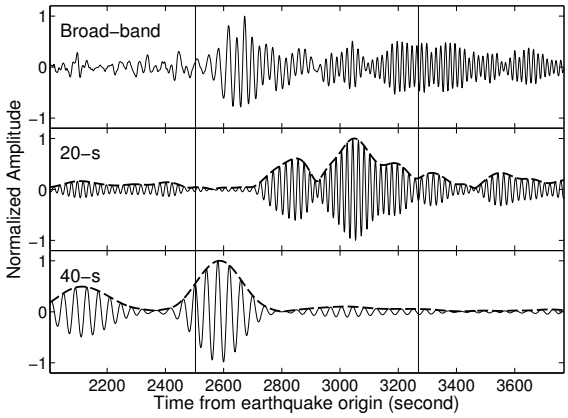

Figure 2.16: Station 327A vertical component record for the same earthquake as in Fig. 2.1. Top panel: the original waveform filtered from 10 s to 200 s. Middle and bottom panels: the narrow-band filtered waveforms with the center periods of 20 s and 40 s respectively. The thick dash lines are the envelope functions, two vertical solid lines show the location of the isolation window function W_S. It is a challenge for the FTAN method to make robust measurements at short periods as the selection of group delay can be uncertain.

2.5.2 Alternative approaches to Eikonal and Helmholtz Tomography

Given a collection of cross-correlation phase delays and station amplitudes, we considered several options in the inversion for both apparent phase velocity (via Eikonal tomography), as well as structural phase velocity (via Helmholtz tomography). Because we measure differential phase between stations instead of absolute phase at individual stations, we directly invert for the orthogonal components S_R and S_T of the slowness vector, rather than reconstructing the travel time surface $\tau(\vec{r})$ and then taking its gradient to obtain apparent phase velocity. This notion provides several advantages. First, we apply the standard slowness-based ray theory as the basis for the inversion, and like conventional ray theory tomography, the ray density serves as a valuable quantification of the data constraints. Directly inverting for the desired variable (slowness and/or phase velocity) provides better control on the smoothness of the inversion, compared to applying smoothing kernels to the integral of slowness (travel time). For example, minimizing the second derivative of the slowness still allows for it to vary

smoothly, while minimizing the second derivative of travel time is comparable to minimizing slowness variation directly. Finally, constraining the smoothness along the radial and tangential directions of the great circle path is more natural for the 2D propagating wave field than along the latitude and longitude direction. Testing suggests that this approach may not produce significant differences in the apparent phase velocity for the far-field measurements as in this study, but may help the near-field surface fitting for ambient noise studies as in *Lin et al.* (2009).

Fig. 2.17b and c compares two applications of Eikonal tomography inversion of the same phase measurements. Directly inverting for slowness suppresses high-wavenumber, low-amplitude variations in phase velocity that are likely due to noise, while maintaining the magnitude of the stronger, well-resolved anomalies (e.g. the edge of the Colorado Plateau). This improvement has the potential to enhance the resolution of the final structural phase-velocity results, though it is secondary compared to the improvement we obtain from the cross-correlation phase measurement (Fig. 2.17a and b).

Obtaining the amplitude correction term for Helmholtz tomography presents several challenges. Amplitude measurements are not as robust as phase measurements, as they are susceptible to variations in local amplification and station terms (*Lin et al.*, 2012; *Eddy and Ekström*, 2014). Moreover, the correction term relies on the estimation of the amplitude Laplacian. Using finite difference to calculate the second-order derivative of a surface at a certain location requires 9 to 16 adjacent data points, which is triple that required to estimate the gradient. For the USArray with ∼70-km station spacing, the amplitude correction term has a maximum resolution of ∼140 km (*Lin and Ritzwoller*, 2011). Finally, fitting an amplitude surface by minimizing its curvature does not guarantee the smoothness of its Laplacian term, as shown in Fig. 2.18b. Adding fourth order derivative minimization into the damping kernel to fit the amplitude surface was attempted, but no significant improvement was observed.

To partially resolve these difficulties, we adopt a slight modification to the approach of *Lin*

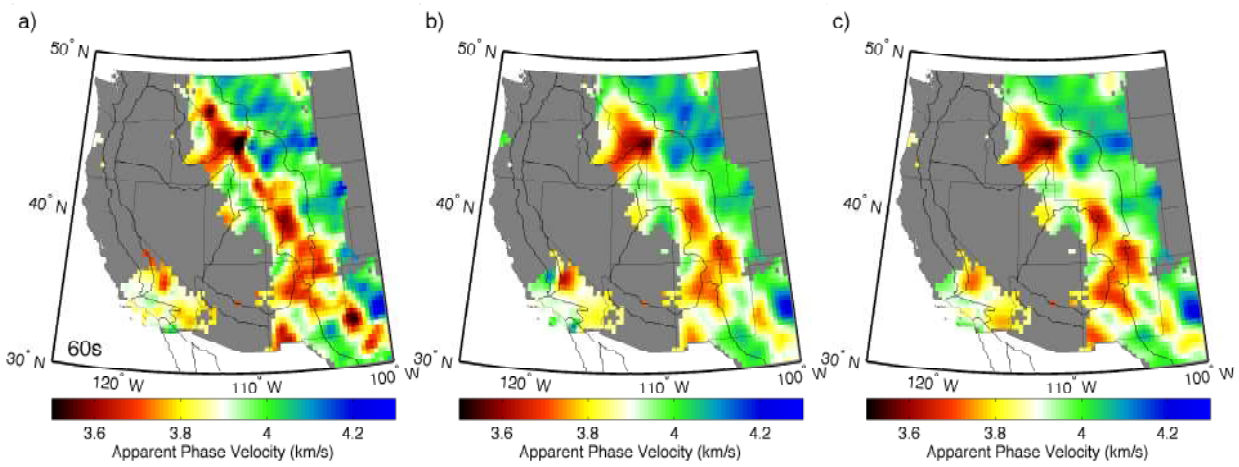

Figure 2.17: 60-s Rayleigh-wave Eikonal tomography results for the April 7, 2009 earthquake near Kuril Islands (M_s=6.8), using different phase-measurement and tomographic-inversions techniques.**a)** Phase measurement: FTAN; Tomography: gradient of the travel-time surface. **b)** Phase measurement: cross-correlation; Tomography: gradient of the travel-time surface. **c)**Phase measurement: cross-correlation; Tomography: slowness vector inversion.

and Ritzwoller (2011). After retrieving the amplitude surface (Fig. 2.18a) and calculating the second derivative, a rough correction term is generated (Fig. 2.18b). We then fit a minimum curvature surface again over this preliminary correction term, with a much larger damping factor to remove any variance with the wavelength shorter than the theoretical resolution (140 km for USArray), as shown in Fig. 2.18c. The smoothed correction term can then be applied to clean up the apparent phase velocity map. By comparing Fig. 2.18d and Fig. 2.17c, we can see that the bias generated by multipathing interference is significantly reduced and the shapes of the anomalies are more consistent with the geological structures.

2.5.3 Compatibility with the two-plane-wave method

The two-plane-wave method (TPWM) (*Forsyth and Li*, 2005) is widely applied in the field of surface wave tomography. The assumption that the surface wavefield can be approximated by two interferencing plane waves can be limiting, in particular for very large arrays such as the USArray, but the approach has some advantages for small arrays and arrays with irregular station spacing. In its traditional formulation, the TWPM requires significant

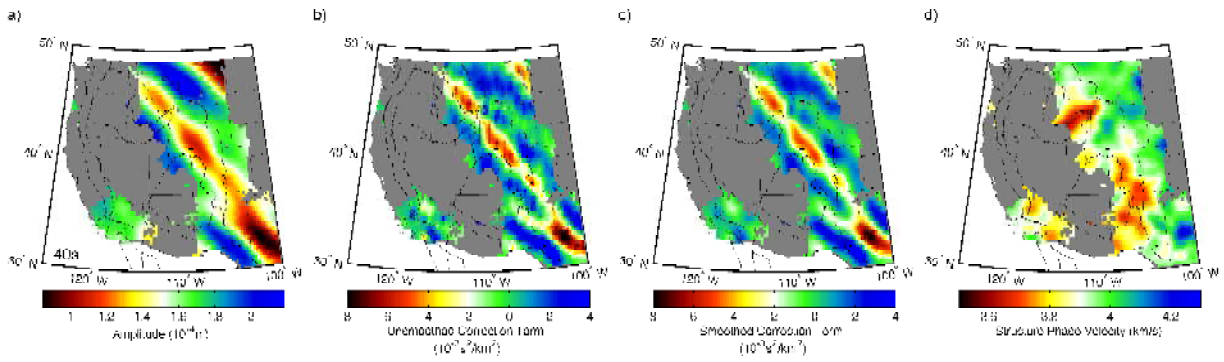

Figure 2.18: Demonstration of the amplitude-correction procedure on the apparent phase-velocity map in Fig. 2.17c. **a)** The amplitude map generated from the minimum-curvature surface interpolation. **b)** The preliminary correction term derived from (a) via Helmholtz equation. **c)** The smoothed correction term. **d)** The corrected phase velocity map, derived from c) and Fig. 2.17c.

manual interaction, with amplitude and phase information being measured at individual stations via Fourier analysis, and requiring low-quality data to be manually discarded prior to inversion for phase velocity. In this section, we provide a simple algorithm to convert the cross-correlation measurements into a format that can be used as the input into the TPWM inversion algorithm.

The TPWM requires the relative phase delays of all stations compared to a reference station. The cross-correlation measurements provide differential phase between station pairs. Each phase difference measurement can be written as

$$\tau_i - \tau_j = \delta\tau_{ij}, \tag{2.15}$$

where τ_i and τ_j represent the absolute phases at station i and station j, and $\delta\tau_{ij}$ is the cross-correlation phase difference measurement derived in this study. To solve for τ_i, a matrix

formula $A\tau = \delta\tau$ is built as:

$$\begin{pmatrix} 1 & -1 & 0 & \cdots \\ 1 & 0 & -1 & \cdots \\ 0 & 1 & -1 & \cdots \\ \vdots & \vdots & \vdots & \vdots \end{pmatrix} \begin{pmatrix} \tau_1 \\ \tau_2 \\ \tau_3 \\ \vdots \end{pmatrix} = \begin{pmatrix} \delta\tau_{12} \\ \delta\tau_{13} \\ \delta\tau_{23} \\ \vdots \end{pmatrix} \tag{2.16}$$

Where the matrix A on the left side is redundant but not full rank, as no absolute phase information of any station is given. At this point we need to add one more equation to the set:

$$\tau_1 = 0, \tag{2.17}$$

by assuming the first station (any station in the array) has zero phase. Then the matrix A is invertible, and the problem can be solved by a simple least-squares inversion:

$$\tau = (A^T A)^{-1} A^T \delta\tau, \tag{2.18}$$

where τ is now the relative phase delay of all the stations compared to the reference station. τ and the array amplitude measurements (Section 2.2.3) can then be used as the input for TPWM inversion.

2.6 Conclusion

We present a new method to measure the surface-wave phase velocity across a seismic array. This method is based on the cross-correlation of waveforms from nearby stations to obtain the phase variations between station pairs. We find that the cross-correlation measurement is more robust than the conventional single-station FTAN measurement under the influence of random noise.

The phase variation and amplitude measurements are inverted for the structural phase

velocity using the Helmholtz equation (*Lin and Ritzwoller*, 2011). With the coherence and other data quality estimations serving as selection criteria, we build an automated system that retrieves phase velocity maps directly from seismic data without manual interaction. We apply this system to the USArray TA and produce robust and up-to-date phase velocity maps for the continental US for Rayleigh waves in the 20-100 s band. The Love-wave phase-velocity results are also calculated, but they display systematic bias compared to ambient noise and other results that we interpret as overtone interference. Further study is underway to investigate this phenomenon.

The Rayleigh wave phase velocity maps clearly outline major geological structures (e.g., Snake River Plain, Basin and Range, Colorado Plateau, Yellowstone hotspot, Rocky Mountains, Mid-Continent Rift, Appalachian Mountains), indicating shear velocity variations in the crust and the upper mantle associated with these structures. A 2D spectral analysis of the phase-velocity maps suggests that the magnitude of velocity variation linearly depends on the structural wavelength. The phase velocity variations in the western US are on average 1-2 times greater than those in the eastern US at most of the structural wavelengths.

The methodology and automated system we develop in this paper has been adopted by IRIS as a data product to provide weekly updated phase velocity maps of continental US at: `http://www.iris.edu/ds/products/aswms/`. The Matlab code of the Automated Surface-Wave Measuring System (ASWMS) is available at `https://github.com/jinwar/matgsdf`.

Acknowledgments

The authors thank Colleen Dalton and four anonymous reviewers for their helpful comments that improved the manuscript. We thank Fan-Chi Lin for providing FTAN measurements for comparison, and Anna Foster, Jiayi Xie and Göran Ekström for informative discussion. Weisen Shen provided geological boundaries of the western US and additional FTAN measurements. We are grateful to everyone involved in the deployment and operation of the

USArray Transportable Array. Seismic data were collected from the IRIS Data Management Center (www.iris.edu). This research was supported by grants from the National Science Foundation's EarthScope program (EAR-0545777 and EAR-1252039).

Chapter 3

Crust and Upper Mantle Structure Associated with Extension in the Woodlark Rift, Papua New Guinea from Rayleigh-wave Tomography

[1]

Abstract

The Woodlark seafloor spreading center is propagating westwards into the Australian plate near the D'Entrecasteaux Islands (DI), Papua New Guinea, generating an active transition zone from continental rifting to seafloor spreading. From March 2010 to July 2011, we deployed 31 inland and 8 off-shore broadband seismic stations around the DI region, to explore the dynamic processes of the lithosphere extension and the exhumation of the high-pressure terranes exposed on those islands. We measure the multi-band (10-60 s) Rayleigh-wave phase velocities from both ambient-noise and earthquake signals. These measurements are then inverted for a three-dimensional shear-velocity model for the crust and upper mantle. The results indicate that the lithosphere extension is localized near the rift axis beneath the

[1]AUTHORS: Ge Jin[a]*, James Gaherty[a], Geoff Abers[b], Younghee Kim[c], Zachary Eilon[a], Roger Buck[a]
[a] Lamont-Doherty Earth Observatory, Columbia University, 61 Route 9W, Palisades, NY 10964, USA
[b] Department of Earth and Atmospheric Science, Cornell University
[c] School of Earth and Environmental Sciences, Seoul National University.
* corresponding author: ge.jin@ldeo.columbia.edu

DI, with a shear-velocity structure in the upper mantle that is similar to mid-ocean ridges. Beneath the Kiribisi Basin west of DI, a ultra-slow shear-velocity anomaly (∼4.0 km/s) is observed at shallow mantle depth (30-60 km), which can be interpreted either by the presence of excess partial melt due to slow melt extraction, or by the existence of felsic crustal material mixing with the surrounding mantle.

3.1 Introduction

The D'Entrecasteaux Islands (DI) of Papua New Guinea locate on the axis of the Woodlark rifting system, which is an active transition zone from continental rifting to seafloor spreading (Figure 3.1) (e.g. *Taylor et al.*, 1999; *Ferris et al.*, 2006). These islands expose the high-pressure (HP) metamorphic terranes bearing the youngest-known ultrahigh-pressure (UHP) coesite eclogite (*Monteleone et al.*, 2007; *Zirakparvar et al.*, 2011). The burial of these HP/UHP rocks is thought to have occured during the Cenozoic arc-continent collision between the Australian Plate and the Papua New Guinea mainland (e.g., *Lus et al.*, 2004), and they remained at mantle depth until being rapidly exhumed to the surface over the last 5-8 Ma at plate-tectonic rates (e.g. *Baldwin et al.*, 2004, 2008; *Gordon et al.*, 2012). The exhumation of the UHP rocks is coeval with the local extensional tectonic environment (*Taylor et al.*, 1999).

The exhumation process occurs on the axis of the Woodlark Rift, synchronous with its westward propagation (*Baldwin et al.*, 1993; *Monteleone et al.*, 2007). The slab pull from the Solomon Sea plate subduction at the New Britain Trench creates a strong extensional environment that favors the exhumation of UHP rocks. There are two competing models to explain the exhumation process in this area: subduction reversal that extracts UHP rocks along the paleo-subduction channel as a low-angle unroofing process (*Hill et al.*, 1992; *Webb et al.*, 2008), or thinning of overlying crust that allows penetration of buoyant continental rocks to the surface as diapirs (*Ellis et al.*, 2011; *Little et al.*, 2011).

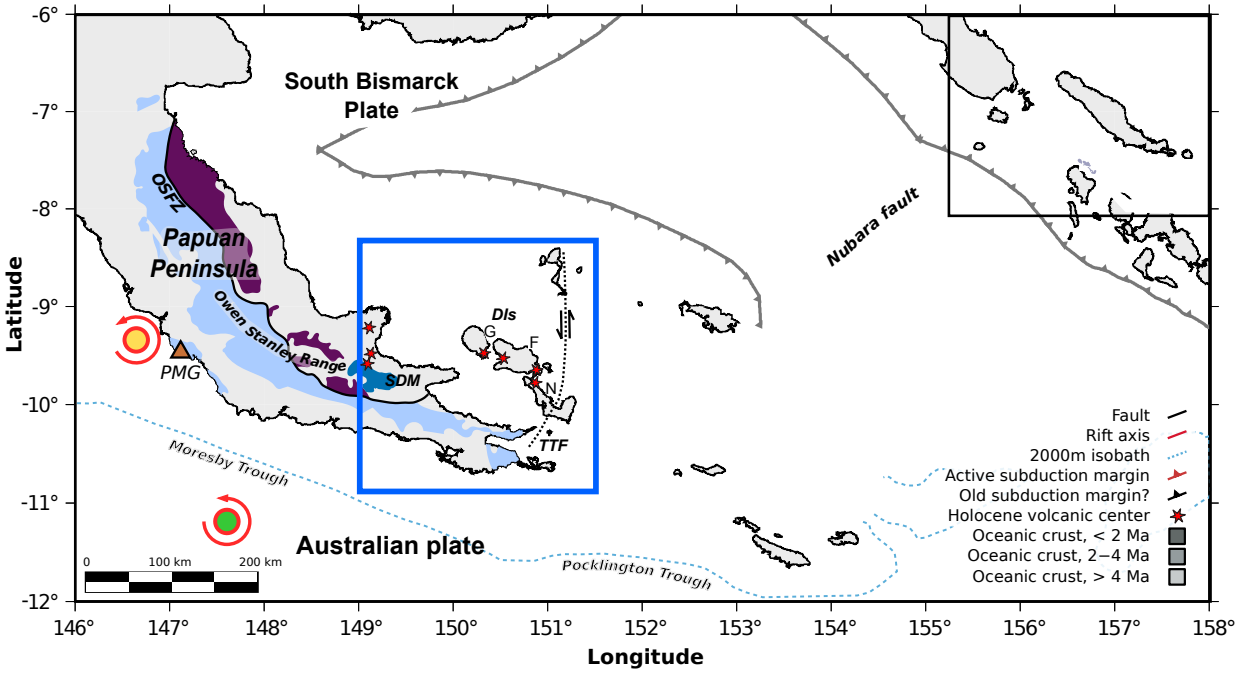

Figure 3.1: Tectonic map of Papua Peninsula and Woodlark Basin (from *Eilon et al.* (2014), modified after *Baldwin et al.* (2008)). Yellow and green circles are Euler poles for the Woodlark plate (WLK) relative to the Australia plate (AUS) between 6.0-0.5 Ma (*Taylor et al.*, 1999) and present-day rotation (*Wallace*, 2004), respectively. Red arrows show the current motions of WLK with respect to AUS given by the GPS measurements (*Wallace*, 2004). Oceanic crust shown by gray shading, Brunes chron indicated by white dashed line, and the recent shift in tectonics is evident from the obliquity of present spreading ridges to magnetic isochrons. Purple shaded: PUB(Papuan Ultramafic Belt); light blue shaded: Owen-Stanley Metamorphics. DIs: D'Entrecasteaux Islands (G: Goodenough, F: Fergusson, N: Normanby); KB: Kiribisi Basin; OSFZ: Owen Stanley Fault Zone; SDM: Suckling-Dayman Massif (Dayman Dome); TP: Trobriand Platform; TTF: Trobriand Transfer Fault. Blue box shows area of field deployment in later figures, active volcanic centers in this region only are depicted. Inset: simplified regional tectonics showing role of WLK and South Bismarck Plate (SBP) in mobile belt between obliquely converging Australian and Pacific (PAC) plates.

A numerical modeling study of the diapiric unroofing process requires extremely buoyant crustal bodies and extensive partial melt in the crust and upper mantle (*Ellis et al.*, 2011). The sporadic volcanism observed across the region may imply the existence of partial melting in upper mantle, with the magmatic composition indicative of subduction enrichment (e.g., *Smith and Davies*, 1976; *Martinez and Taylor*, 1996; *Taylor and Huchon*, 2002). The presence of the high-density Papuan Ultramafic Belt (PUB) within the Papuan Peninsula (Figure 3.1) (*Davies and Warren*, 1988), potentially overlying lower-density continental crust, provides a possible source of gravity instability to fuel diapir extrusion (*Martinez et al.*, 2001).

The youngest high-grade metamorphic rocks locate at Goodenough Island, the westernmost of the DI (*Monteleone et al.*, 2007). At the Kiribisi Basin west of Goodenough Island, where potential UHP exhumation may occur in the future, little localized surface extension can be observed in the geology and stratigraphy offshore (*Fitz and Mann*, 2013), while up to 100-140 km extension is required by the far-field plate motion in the last 6 Ma (*Taylor et al.*, 1999; *Goodliffe and Taylor*, 2007; *Eilon et al.*, 2014). A recent GPS study reveals that most of the current extension is compensated at the normal faults around the DI and at the Mai'iu fault on the Peninsula (*Wallace et al.*, 2014). Although the mantle deformation estimated from seismic anisotropy suggests a broad mantle flow field (*Eilon et al.*, 2014), localized lithospheric extension is observed in the eastern DI (*Abers et al.*, 2002; *Eilon et al.*, 2015). The mantle seismic velocity (and inferred lithospheric geometry) and crustal thickness beneath the Kiribisi Basin are important observations to evaluate the lithospheric extension.

From March 2010 to August 2011, 31 land-based broadband stations (Guralp CMG-3T with 120s-corner sensors) and 8 ocean bottom seismometers (OBS, Trillium 240 with 240s-corner seismometers) were deployed with a station spacing $\sim$25 km, to cover a $2.5^\circ \times 2.5^\circ$ area centered at Goodenough Island (Figure 3.2). We perform surface-wave tomography on the collected data and provide a seismic shear-velocity model to reveal the possible distribution of temperature, melt, and compositional anomalies in the crust and the upper mantle, and

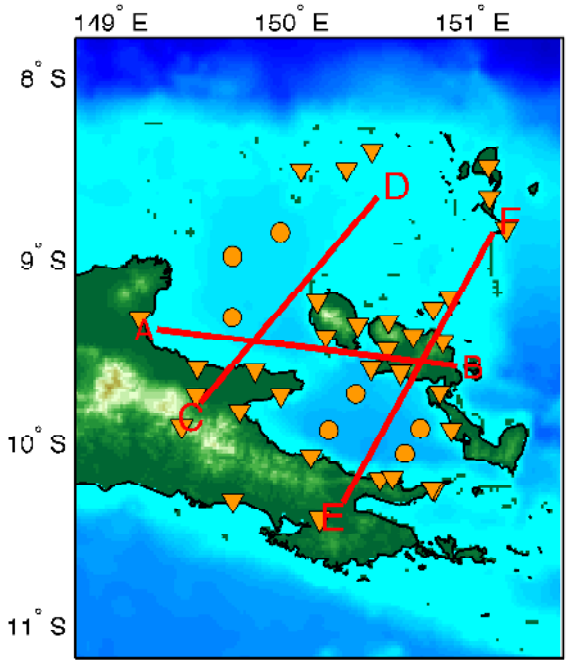

Figure 3.2: Topography map with station and profile locations. Triangles are land stations while circles are OBSs. Red lines are the profile locations shown in Figure 3.9. The map labels are the same as in Figure 3.1.

their possible roles in the UHP unroofing. We find that the mantle extension is localized along the rift axis, and ultra-slow shear velocity in the upper mantle beneath the Kiribisi Basin implies the potential existence of partial melt and/or felsic crustal material.

3.2 Methodology and Data

We image the crust and mantle to approximately 90 km depth in the region using Rayleigh waves derived from a combination of ambient noise and teleseismic earthquakes. Ambient-noise and earthquake-based Rayleigh-wave tomography are highly complementary, in that ambient noise is ideally suited to relatively short periods, while teleseismic Rayleigh waves generally constrain longer periods. In detail, the two sources must be processed separately, but the resulting maps of phase velocity are generally compatible [e.g. Jin and Gaherty,

2015]. In this study, they can be combined to provide phase-velocity dispersion curves from 10-60 sec. Here we summarize the analyses utilized to extract phase velocity from each type of data.

3.2.1 Ambient noise tomography

We use ambient-noise signals to obtain Rayleigh-wave phase velocities at high frequencies (T<20 s). To estimate phase velocity, we apply the measurement in the frequency domain to minimize the limitation of short inter-station distance at long periods (*Aki*, 1957; *Ekström et al.*, 2009; *Calkins et al.*, 2011). The stacked cross-spectrum ρ between two vertical records separated by distance r can be represented as:

$$\rho(r,\omega) = \sum_{m=0}^{\infty} i^m a_m(\omega) \mathcal{J}_m \left(\frac{\omega r}{c(\omega)} \right), \tag{3.1}$$

where $a_m(\omega)$ are the cylindrical the harmonic coefficients of the source azimuthal density function, $\mathcal{J}_m$ are the Bessel functions of the first kind, and $c(\omega)$ is the frequency-dependent phase velocity (*Cox*, 1973). If the source distribution is homogeneous, the only non-zero term of a_m is $a_0 = 1$. The cross-spectrum ρ can be rewritten as (*Aki*, 1957):

$$\rho(r,\omega) = \mathcal{J}_0 \left(\frac{\omega r}{c(\omega)} \right), \tag{3.2}$$

In reality, the source distribution may not be azimuthally isotropic, which causes the imaginary part of the cross-spectrum to be non-zero (*Cox*, 1973). However, this problem can be minimized by properly normalizing the data (*Bensen et al.*, 2007). We can therefore approximate the real part of the cross-spectrum as:

$$Re\left(\rho(r,\omega)\right) = \mathcal{J}_0 \left(\frac{\omega r}{c(\omega)} \right), \tag{3.3}$$

by ignoring the higher order terms of harmonic expansion (*Ekström et al.*, 2009).

We apply this analysis to the continuous broadband vertical-component records, which are down-sampled to 1 Hz and then divided into hour-long segments. After removing the instrument responses, we normalize the traces by applying the running-absolute-mean technique in the time domain to eliminate the effects of large earthquakes (*Bensen et al.*, 2007). Then the normalized cross-spectrum is calculated by stacking the hourly coherency spectrum (*Ekström*, 2013):

$$\rho(\omega) = \frac{1}{N}\sum_{i}^{N} \frac{U_i(\omega)V_i^*(\omega)}{|U_i(\omega)||V_i(\omega)|}, \tag{3.4}$$

where U_i and V_i are the Fourier transform of the i^{th} time-segment records of two stations.

The cross-spectra $\rho(\omega)$ can be transformed back to the time domain to examine the data quality. Figure 3.3 shows the stacked cross-spectra in the time domain after two different band-pass filters. Clean Rayleigh-wave Green's functions can be observed in the period band 10-20 s. The data quality is low at higher frequency band (6-9 s), with asymmetric waveforms and high noise level. This is probably caused by uneven distribution of the secondary microseismic sources (*Tian and Ritzwoller*, 2015).

Ekström et al. (2009) developed a method to estimate dispersion curves in frequency domain by tracking the zero-crossing locations of Bessel functions. With ω_n denoting the frequency of the nth zero-crossing and z_n representing the nth zero of $\mathcal{J}_0$, the phase velocity c at ω_n can be represented as:

$$c(\omega_n) = \frac{\omega_n r}{z_n}. \tag{3.5}$$

This technique is robust but can still have problems with short-path station pairs, since phase velocities only at zero-crossing frequencies can be measured, and other parts of the dispersion curve have to be interpolated. This issue is particularly important in this study, in which the array's aperture is small. By assuming an average phase velocity of 3.2 km/s, the zero-crossing intervals of $\mathcal{J}_0$ being close to π, and a frequency band ranging from 0.04

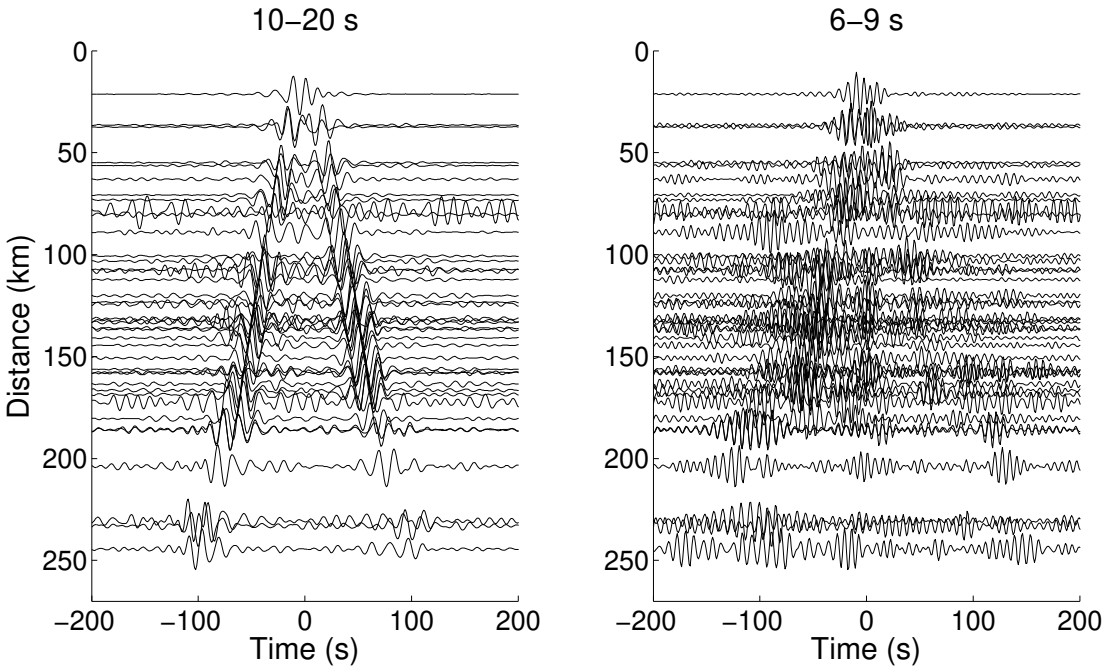

Figure 3.3: Time-domain ambient noise cross-correlation waveforms of station AGAN to all the other stations. Left panel: cross-correlation waveforms filtered between 10-20 s. Right panel: cross-correlation waveforms filtered between 6-9 s.

Hz to 0.15 Hz (6-20 s), the expected number of zero crossings is:

$$N = \frac{\omega_{max} - \omega_{min}}{c\pi} r \approx 0.07r, \tag{3.6}$$

where r is in km. For the station pairs with inter-station path shorter than 70 km, which comprise 30% of all the possible station pairs in this study, only 4-5 data points can be retrieved to constrain the entire dispersion curve.

In order to better estimate phase velocities from the short-path station pairs, we instead fit the entire cross-spectrum waveforms in the frequency band of interest via a non-linear least-square inversion. Equation 3.3 can be rewritten as:

$$Re\left(\rho(r,\omega)\right) = \mathcal{J}_0\left(\frac{\omega r}{c(\omega)}\right) = \mathcal{J}_0\left(\omega t(\omega)\right), \tag{3.7}$$

where $t(\omega) = r/c(\omega)$ is the phase-delay time (or travel time) between the two stations, and

is the unknown variable to be determined. We invert for $t(\omega)$ by minimizing the penalty function ε^2 defined by:

$$\varepsilon^2 = \sum ||\alpha \mathcal{J}_0(\omega t) - Re(\rho)||^2 + a \sum ||\nabla^2 t||^2 + b \sum ||\frac{dt}{d\omega} X\left(\frac{dt}{d\omega}\right)||^2. \tag{3.8}$$

X is a step function, with $X(x \geq 0) = 1$ and $X(x < 0) = 0$, and α is a scaling factor to match the amplitude of $\mathcal{J}_0$ with the observation, which is re-calculated in each iteration.

The penalty function ε^2 has three components. The first term on the RHS is the misfit of the predicted Bessel function to the observation, the second term quantifies the smoothness of dispersion curve, and the third term forces the dispersion to be "normal" within the frequency band, i.e. requires the phase velocity to be slower at higher frequency. The constants a and b are the coefficients that control the weighting of the damping terms. During the inversion, the dispersion curve is down-sampled to 5.5 mHz to decrease the number of unknowns. Examples of the Bessel function fitting can be seen in Figure 3.4. The intra-station paths between the station MAYA and the OBS D to the station AGAN are very similar, and so is their average dispersion (right panel). The discrepancies at long periods are caused by the large Bessel function misfit of the land-OBS pair at low frequencies, probably due to the lower SNR. The OBS-OBS pairs in general have very low SNR for this dataset, especially for the frequencies higher than 0.08 Hz (12.5 s). They only comprise 7% of the measurements, and are omitted from subsequent inversions.

The phase travel times between 496 station pairs with more than 2000 hours of cross-correlation time and high SNR are selected to invert for the 2D phase velocity maps at different frequencies. We adopt the ray-theory tomography, and weight each measurement based on the misfit of the Bessel-function fitting and the number of time segments being stacked. Only the station pairs with intra-station distances between one and six wavelengths of the Rayleigh waves are included in the tomographic inversion. We apply a smoothness damping by minimizing the second-order gradient of the phase velocities. The phase-velocity maps are generated at 8 periods from 10.2 to 17.4 s. A checkerboard test shows that anomalies

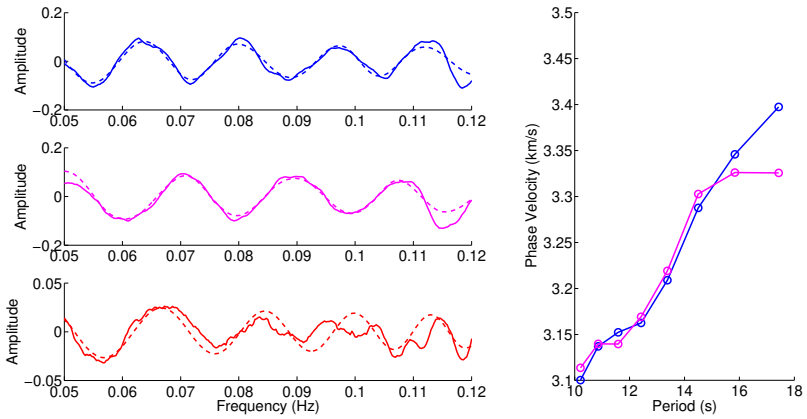

Figure 3.4: Examples of cross-spectrum waveform fitting. Left: Solid lines are observations and dashed lines are fitting results. Blue lines are from a land-land station pair (AGAN and MAYA), magenta lines are from a land-OBS pair (AGAN and D), while red lines are from an OBS-OBS pair (E and H). Measurements from OBS-OBS pairs are discarded due to the low SNR. Right: dispersion curves from the Bessel function fittings in the left panel.

larger than ∼40 km can be well retrieved. Examples of the phase-velocity maps from the ambient-noise analysis are shown in the first row of Figure 3.5.

3.2.2 Earthquake Helmholtz Tomography

We use teleseismic surface waves to estimate Rayleigh-wave phase velocities at low frequencies. In this study, we adopt the automated surface wave measuring system (ASWMS) developed by *Jin and Gaherty* (2015) to retrieve the 2D phase-velocity maps.

The ASWMS measures the phase variations between nearby stations by calculating the multi-channel cross-correlation functions $C_i(t)$ between vertical component records, which can be summarized as:

$$C_i(t) = F_i * W_c(S_1 \star W_s S_2), \tag{3.9}$$

where S_1 and S_2 are the seismic records from two nearby stations, W_S is the window function applied only on the station 2 waveform to isolate the phase of interest (Rayleigh wave in

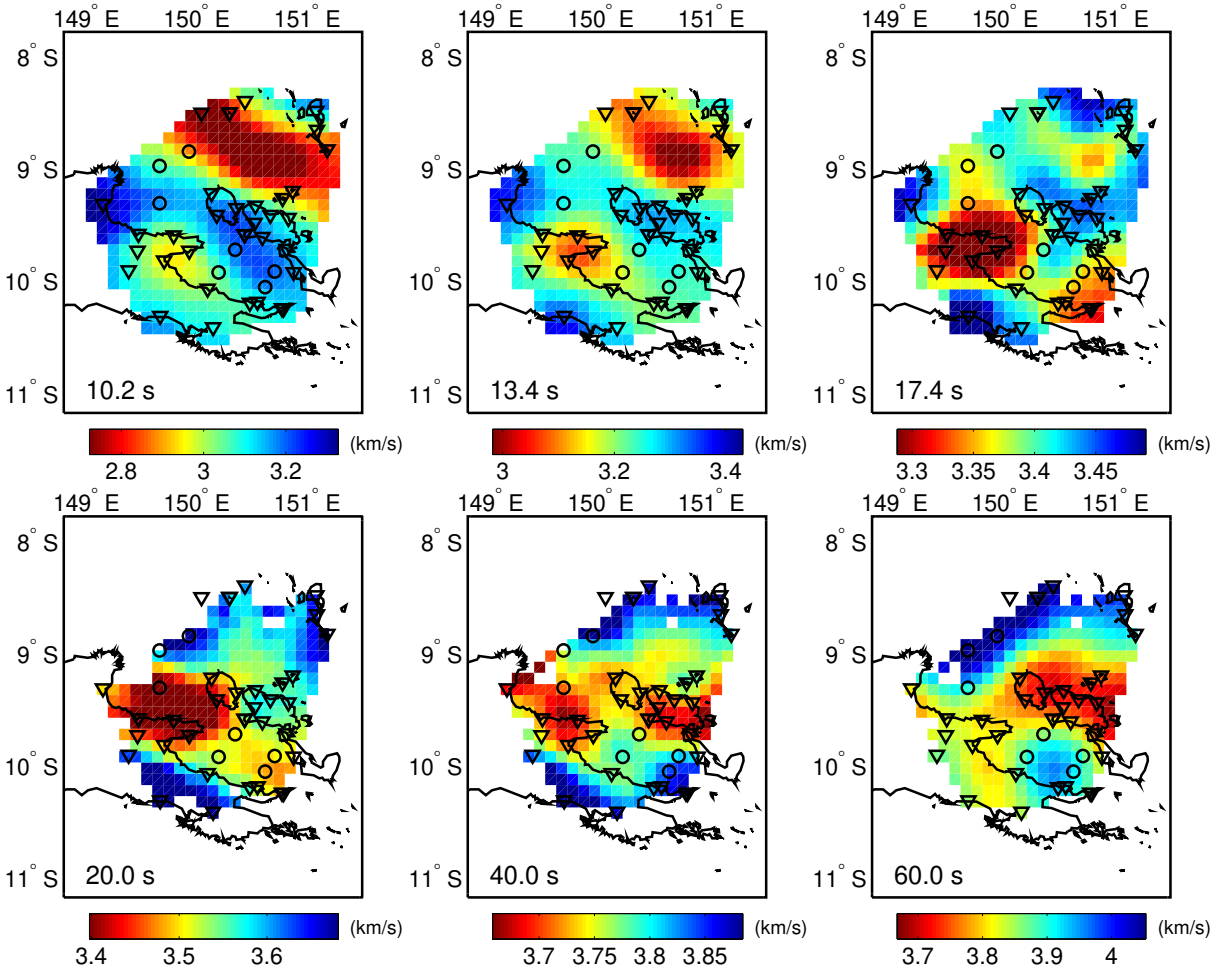

Figure 3.5: Phase velocity maps at different periods. The upper panels show the results from ambient noise, while the lower panels show the earthquake results. Land stations and OBSs are indicated by triangles and circles respectively.

this study), "$*$" is the convolution operator, "$\star$" is the cross-correlation operator, W_c is the window function applied on the cross-correlation waveform to further isolate the coherent signal generated by fundamental Rayleigh waves, and F_i is the i^{th} narrow band filter with the central frequency ω_i.

$C_i(t)$ is then fit by a five-parameter wavelet defined as:

$$C_i(t) \approx AGa\left[\sigma(t-t_g)\right]\cos\left[\omega(t-t_p)\right], \tag{3.10}$$

where the two important variables are the group delay t_g and the phase delay t_p between the two stations, while Ga is the Gaussian function, A is a positive scale factor, σ is the half-bandwidth, and ω is the center frequency of the narrow-band waveform.

The phase delay t_p is then corrected for cycle-skipping and bias generated by the window functions. We define the corrected phase delay as $\delta\tau_p$. In most cases, there is only subtle difference between t_p and $\delta\tau_p$.

We retrieve the corrected phase delays $\delta\tau_p$ from all nearby station pairs within 200 km, and use these measurements to invert for the phase-velocity maps. The Eikonal tomography method (*Lin et al.*, 2009) is modified to adapt to the irregularly spaced arrays (*Jin and Gaherty*, 2015). The phase delay $\delta\tau_p$ between two stations is written as:

$$\delta\tau_p = \int_{\vec{r}_1}^{\vec{r}_2} \vec{S}(\vec{r})d\vec{r}, \tag{3.11}$$

where $\vec{r}_1$ and $\vec{r}_2$ are the location vectors of the two stations, and $\vec{S}(\vec{r})$ is the slowness vector field to be solved. The slowness vector field is inverted independently for each event, and the apparent phase velocity can be obtained from the length of the slowness vector: $c' = 1/|\vec{S}(\vec{r})|$.

We then use the amplitude measurements to further correct the phase-velocity maps obtained from the Eikonal tomography. The amplitudes are measured using the auto-correlation functions that are similar to the definition of Equation 3.9, except S_1 is substituted for S_2. The auto-correlation function is then fitted via Equation 3.10, and the scale

factor A is a good approximation of the power spectrum amplitude at the center frequency ω_i.

The amplitude measurements are used to correct the Eikonal phase velocity c' for the effect of multi-pathing via the Helmholtz equation (*Lin and Ritzwoller*, 2011):

$$\frac{1}{c^2(\vec{r})} = \frac{1}{c'^2(\vec{r})} - \frac{\nabla^2 A(\vec{r})}{A(\vec{r})\omega^2}, \tag{3.12}$$

where $c(\vec{r})$ is the corrected (structural) phase velocity and $A(\vec{r})$ is the amplitude field. We retrieve individual structural phase-velocity maps for each event, which are then averaged to obtain the final phase velocity maps at each frequency.

From March 2010 to June 2011, a total of 93 earthquakes with magnitudes larger than 6.0, source depths shallower than 50 km, and epicentral distances from 20° to 140° are selected. The azimuthal distribution of the events is shown in Figure 3.6. The azimuthal distribution of events is not even, since a large number of eligible earthquakes are from the NNW direction. *Eilon et al.* (2014) report strong azimuthal anisotropy existing in this area. This uneven-distribution of back azimuths may induce some bias in the phase-velocity measurements, which is further discussed in Section 3.3.2. The phase velocities obtained using the Helmholtz tomography method is shown in the lower row of Figure 3.5.

3.2.3 Shear-Velocity Inversion

We utilize the phase-velocity maps to construct a three-dimensional (3D) shear-velocity model for the region. At each pixel, dispersion curves are retrieved from the phase-velocity maps, and then inverted for 1-D shear-velocity model. This inversion is known to be strongly dependent on choice of a starting model. In order to minimize and evaluate the effect of the dependence, we develop a strategy that can be divided into three steps: a grid-search for the best initial model, a random perturbation on the best model to generate a large initial model set, and iterative nonlinear least-squares inversions to get the final model distribution.

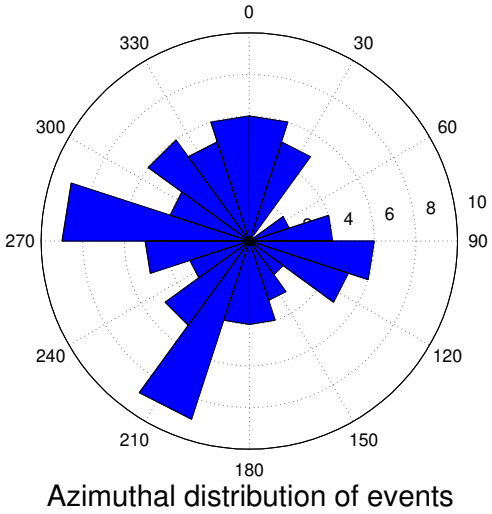

Figure 3.6: Azimuthal distribution of events for the earthquake-based phase-velocity measurements.

The final models from the random initial models are statistically summarized to get the final result.

First, we search through a range of parameters to find a good starting model at each pixel. In this step, the model space is simply divided into three layers: a shallow layer representing sediment or shallowmost crustal rocks, a crustal layer with the thickness constrained by the preliminary receiver-function results (*Abers et al.*, 2012; *Obrebski et al.*, 2014), and a half-space layer underneath representing the mantle. The receiver function analysis is based on the H-κ stacking approach *Zhu and Kanamori* (2000) to estimate the Moho depth at each station location. These Moho depths are preliminary, but provide a good estimation of first-order crustal thickness variation in the area. We use a minimum-curvature surface fitting to produce a continuous Moho-depth variation across the array. For each pixel, we search through various shallow-layer thicknesses, crustal velocities, and mantle velocities to find the best 3-layer model, which provides the minimum misfit to the observed dispersion curve. The parameter space being searched through is listed in Table 3.1.

In order to evaluate the effect of initial model dependency on the resulting model, we randomly perturb the best initial models found in the previous step. At each pixel, all the

Table 3.1: Initial Model Grid-search Parameters

Parameter	Search values	Unit
Shallow layer thickness	2, 4	km
Shallow layer velocity	2.5 7	km/s
Crustal velocity	3.4, 3.5, 3.6	km/s
Mantle velocity	4.1, 4.3, 4.5, 4.7	km/s

model parameters are perturbed within a certain range to generate a large set of initial models. The maximum perturbations for the model parameters are: 30% for shallow-layer velocity, 10% for crust and mantle velocities, 5 km for crustal thickness, and 1 km for shallow-layer thickness. For each pixel, we generate 100 random initial models to feed into the later inversion.

We utilize the program *surf96* (*Herrmann and Ammon*, 2004; *Herrmann*, 2013) to invert for detailed 1D structures of the crust and upper mantle. This program iteratively perturbs the shear velocity of each model layer to fit the observed dispersion curve at a given pixel using an iterative least-squares approach. We divide the crust (without the shallow layer) of initial models into 4 layers with even thickness, and the mantle into 10 layers with a thickness of 10 km. At each iteration, a smoothness damping is applied to the shear-velocity perturbations in the crust and in the mantle separately (no smoothing is applied across the Moho). This procedure ensures the smoothness of final model, while maintaining the velocity discontinuity across Moho if it is required by data.

The non-linear least-squares inversion is performed on the 100 initial models generated in the previous steps at each pixel. Final models with large misfits are discarded (20 % larger than the average misfits), with the rest being selected to estimate the mean and standard deviation of the shear velocities at a certain depth.

Examples of the inversion results are shown in Figure 3.7. The averaged 1-D shear velocity profiles of each the pixel are gathered to form the 3-D shear velocity model shown in Figures 3.8 and 3.9.

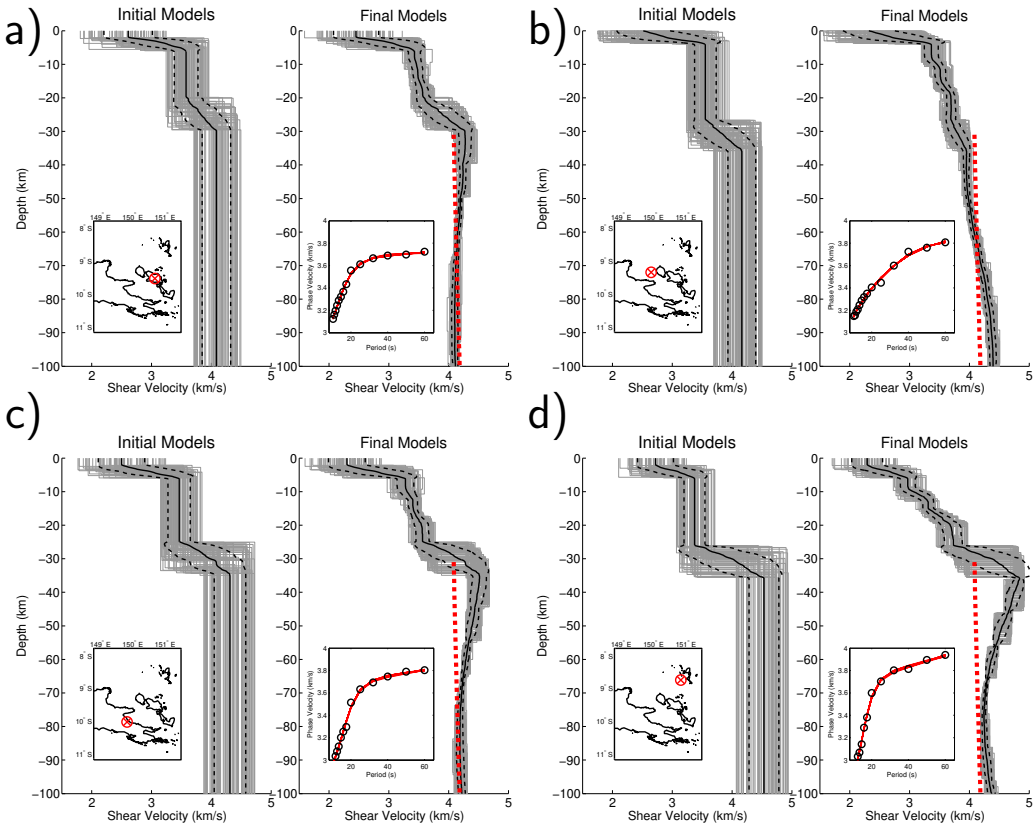

Figure 3.7: One-dimensional shear velocity inversions at several example locations. For each subplot, left panel shows the random generated initial models (grey lines), while right panel shows inverted final models. Mean model is represented by solid black line, with dashed black lines indicating one standard deviation. The red line from 30-100 km in the right panel shows the Vs calculation from mantle adiabatic upwelling model, using the parameters from *Jackson and Faul* (2010), while the green line shows the EPR model from *Gu et al.* (2005). The embedded map in the left shows the grid location, while the embedded panel in the right shows the inverted phase velocities (red lines) compared to the observations (black circles). a) Fergusson Island. b) Kiribisi Basin. c) Papua Peninsula. d) Trobriand Platform.

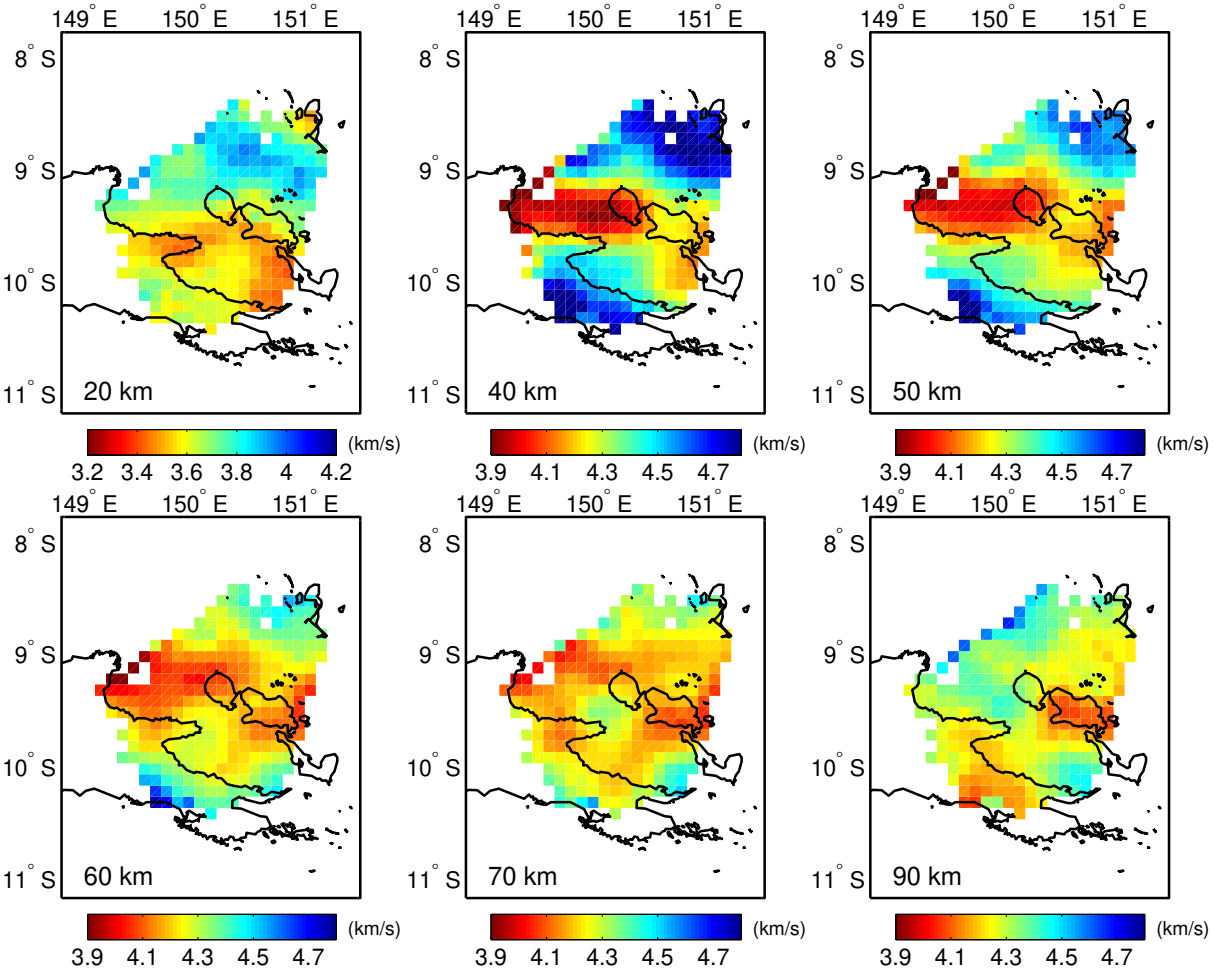

Figure 3.8: Mean shear velocity at different depths. Depth of 20 km corresponds to mid-to-lower crust, while the panels 40 km and deeper represent variation in the mantle.

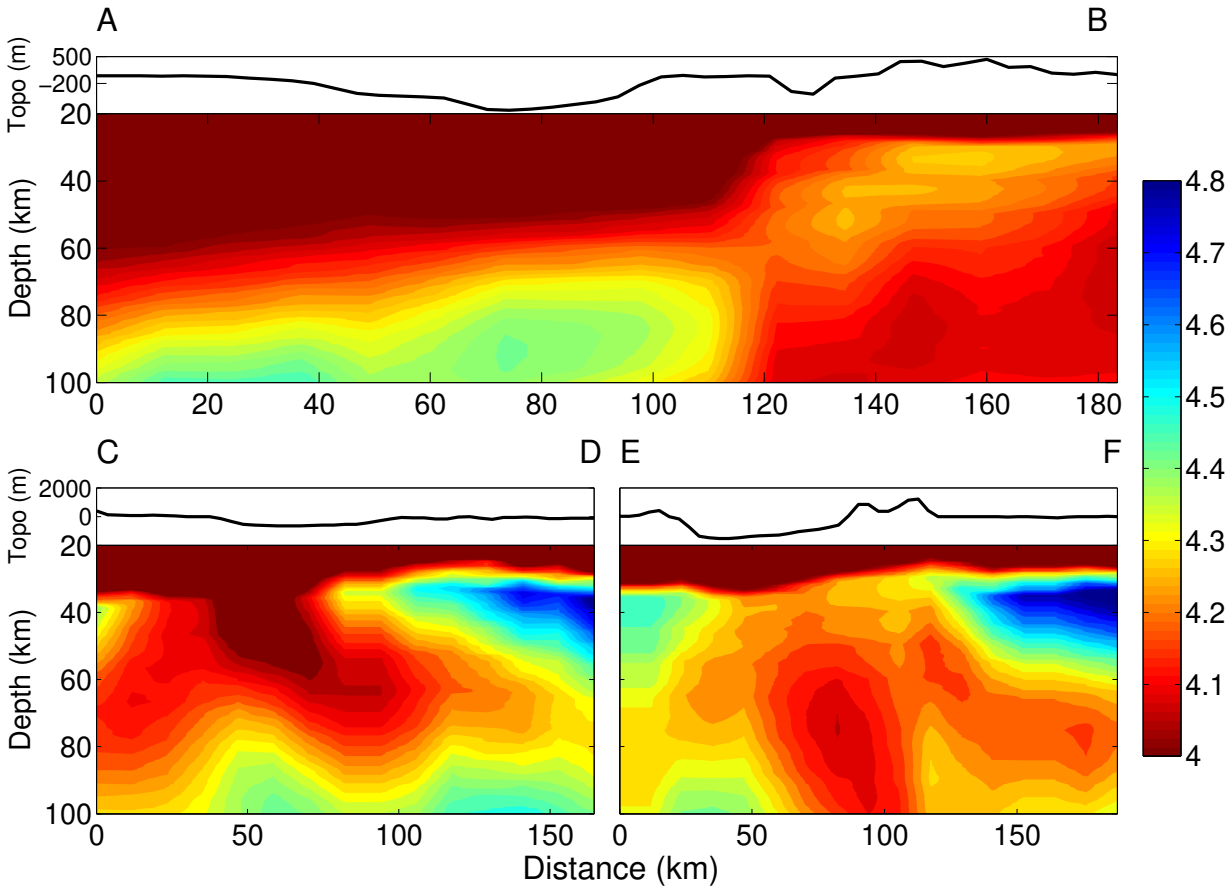

Figure 3.9: Mean shear velocity along vertical 2-D profiles. The location of profiles can be found on Figure 3.2.

3.3 Results

3.3.1 Phase Velocity

Phase-velocity maps of selected periods are shown in Figure 3.5. In general, phase velocities at higher frequencies are more sensitive to shallower structures. In detail, the sensitivity is highly dependent on the velocity structure. For general earth structure, the peak sensitivity depth is approximately one-third of the surface-wave wavelength.

The highest frequencies (10-15 s) are primarily associated with variation in crustal velocities, including the possible effect of thick sediments in the Trobriand Platform (*Fitz and Mann*, 2013). The 17-s and 20-s phase-velocity maps correlate well with the Moho topography from the preliminary receiver-function results (Figure 3.10), as the Moho depth variation in the region (20-40 km) (*Abers et al.*, 2002, 2012; *Obrebski et al.*, 2014) corresponds to the peak Rayleigh-wave sensitivity at these periods (Figure 3.11). For regions with thinner crust (for example, Fergusson and Goodenough Islands), more mantle rocks are sampled and therefore the phase velocity is higher. The consistency between the two observations shows good reliability of both results. At low frequencies (T>20 s), the slow anomalies mainly locate along the projection of the Woodlark Rift axis, with the slowest region moving from west to east as period increases. At low frequencies, the slow anomalies mainly locate along the projection of the Woodlark rift axis, with slowest region moving from west to east as frequency decreases.

As presented in Section 3.2, the phase velocities at short periods (10-17 s) and at long periods (20-60 s) are retrieved using different methods. The short-period phase velocities are inverted based on the straight-ray assumption, as the array aperture is not large enough to perform Eikonal tomography. Theoretically, the straight-ray tomography can be biased by the ray-bending effect. However, *Lin et al.* (2009) show that this bias is fairly small ($< 0.3\%$) for short intra-station distance, such as used here. The smoothness of the dispersion curves across the transition also implies that this bias is small for our data.

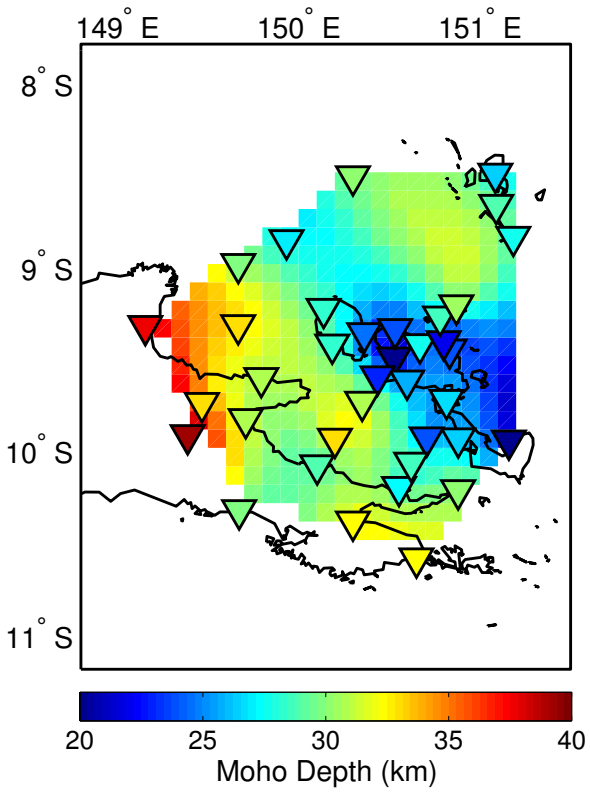

Figure 3.10: Crustal thickness from the receiver function analysis (*Abers et al.*, 2012). Values between the stations are interpolated using a minimum-curvature surface.

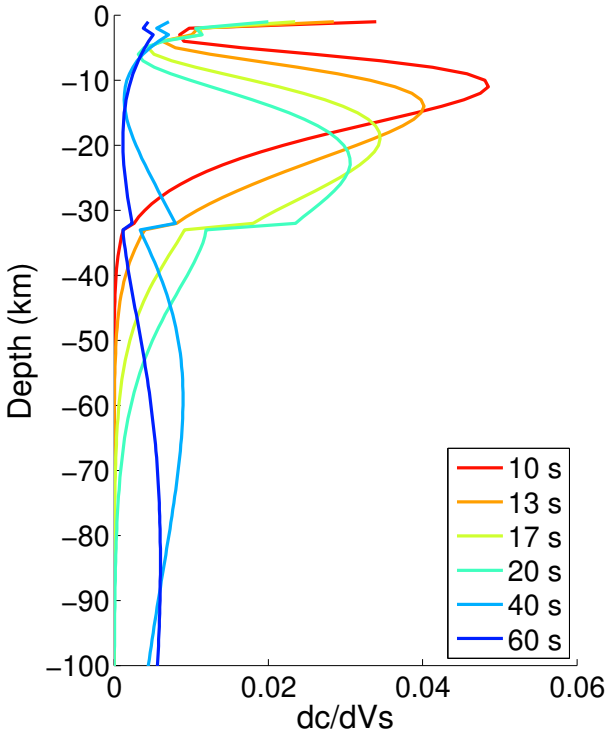

Figure 3.11: Shear-velocity sensitivity kernels of Rayleigh-wave phase velocities at different frequencies. The kernels are calculated based on a 1D model with a 32-km crust.

3.3.2 Shear Velocity

A large part of the shear-velocity uncertainties come from the initial model dependence of the inversion. At each pixel, 100 initial models are randomly generated to invert for shear-velocity profiles. These profiles are then averaged to provide the final result (Section 3.2.3). In general, the standard deviations of the shear velocities from different initial models are smaller than 0.05 km/s at mantle depth (>40 km). The standard deviations are higher around Moho depth (0.1-0.15 km/s), as dispersion curves cannot precisely constrain sharp velocity transitions. The inversion results of several typical locations, together with their uncertainties, are shown in Figure 3.7. The depth slices and cross sections of the 3D shear velocity model are shown in Figure 3.8 and 3.9.

These results outline several main features:

1. The axis of the Woodlark rift beneath the DI is identified by slow anomalies with a width about 60 km, extending in depth to the model base.

2. The shallow mantle beneath the Kiribisi Basin west of Goodenough Island (30-60 km, centered around 9.4°S, 149.9°E) is slower than that beneath the eastern DI.

3. Mantle velocity beneath the Trobriand Platform and the Papuan Peninsula are notably higher, consistent with stable lithosphere mantle.

Since the period range we use for the inversion is from 10-60 s, the structures shallower than 10 km and deeper than 90 km are not well constrained. In addition, the Moho depths of the initial models are constrained by the preliminary receiver-function results. A more formal inversion of receiver function waveforms using dispersion constraint is underway (*Obrebski et al.*, 2014). Our approach allows us to retrieve a continuous velocity volume, that incorporates the first-order Moho variability, but we do not interpret Moho depth explicitly (Figure 3.7).

Eastern D'Entrecasteaux Islands

The average shear velocity at 20 km depth is around 3.5 km/s beneath Fergusson Island and west of Normanby Island (Figure 3.8). This result agrees well with the body wave tomography result (3.6 km/s) at 23.5 km depth derived from travel times of local events (*Ferris et al.*, 2006). Such slow velocities suggest a felsic to intermediate lower-crustal composition, which matches well with the granitic intrusion associated with the metamorphic core complex unroofing observed on the DI (*Ferris et al.*, 2006).

The crust beneath the eastern DI is significantly thinned to ∼20 km, compared to the likely original thickness of 35-40 km seen at off-axis stations (*Abers et al.*, 2002, 2012). Mantle velocities at this location are low relative to the off-axis regions, implying that the lithosphere has been thinned. This localized crustal and lithospheric extension is likely associated with mantle upwelling, which generates temperature variation and possible partial melt in the upper mantle. The deeper mantle (>60 km) beneath this region has a shear velocity around 4.1 km/s (Figure 3.7a), which is close to asthenosphere velocities beneath the youngest oceanic lithosphere (*Nishimura and Forsyth*, 1989; *Gu et al.*, 2005), where the mantle geotherm is likely controlled by adiabatic upwelling (Figure 3.7a).

The upper-most mantle (25-40 km) is slightly faster, with a value ranging from 4.2 to 4.3 km/s. This fast-velocity structure is very similar to the Ethiopian Rift in the east Africa at the similar depth, where the continental lithosphere is thinned due to lateral extension, with the remaining represented by a thin fast seismic lid at the most shallow part of the mantle (*Dugda et al.*, 2007; *Keranen et al.*, 2009).

Kiribisi Basin

Figure 3.7b displays a typical shear velocity structure beneath the Kiribisi Basin between Goodenough Island and the stratovolcano Mt. Victory. The preliminary receiver-function results suggest a Moho depth around 30-35 km in this region. However, these results are mainly constrained by the OBS measurements, which are not reliable due to the complexity of

signals recorded, possibly due to basin reverberations. The shear velocity inversion shows no significant velocity discontinuity deeper than 20 km, but displays a gradual velocity increase at shallow depths: from 3.3 km/s in the upper crust (<10 km), to 3.5 km/s at mid-crustal depth (10-15 km), to 3.8 km/s in the lower crust depth (>18 km). This crustal structure is similar with the structure along the coastal area of Papua Peninsula northwest of Mt. Victory from previous seismic refraction studies (*Finlayson et al.*, 1976, 1977).

Very slow shear velocities (∼4.0 km/s) are observed at shallow mantle depth from 30 to 60 km beneath this region, which is slower than the mantle beneath the DI at the same depth. Deeper than 60 km, the shear velocity increases rapidly with depth, reaching a value of 4.4 km/s at 90 km.

Papua Peninsula and Trobriand Platform

Figure 3.7 c and d depict the typical shear velocity profiles of the Papuan Peninsula and the Trobriand Platform, respectively. These two regions show a similar structure and we interpret them as representing the unrifted continental lithosphere. The receiver function results suggest Moho depth in these regions of ∼30-35 km, and the shear velocity inversion requires a sharp velocity discontinuity at a similar depth.

In the upper mantle, a fast seismic layer exists from the Moho to about 60 km depth. The lithosphere beneath the Trobriand Platform appears much faster than that beneath the Papuan Peninsula. This fast anomaly is at the edge of our array and thus poorly resolved by surface waves, but teleseismic body-wave tomography (*Eilon et al.*, 2015) also shows a significant velocity contrast (∼10%) between the Trobriand Platform and the DI at upper-mantle depths (60-120 km). The consistency between these two studies indicates that the fast velocity zone in the upper mantle beneath the Trobriand Platform may be real. *Eilon et al.* (2015) also note the presence of intermediate-depth earthquakes in this region (*Dieck et al.*, 2013), and discuss the interpretation of the anomaly as continental lithosphere or a remnant slab fragment.

3.4 Discussion

3.4.1 Localization of lithospheric extension

There are significant variations of the extension rate along the Woodlark Rift due to the plate motion geometry. A maximum of ∼140 km extension is required west of Goodenough Island and ∼200 km east of Normanby Island (*Taylor et al.*, 1999; *Eilon et al.*, 2014). This ∼30% difference in extension may lead to variations in the localization of lithospheric extension along the rift.

In the eastern DI, the seismic observations are consistent with substantial crustal thinning and lithospheric removal (*Abers et al.*, 2002, 2012; *Eilon et al.*, 2015). The exhumed domes, containing rocks that reached maximum pressures of ∼3 GPa (100 km) (e.g. *Baldwin et al.*, 2008), currently occupy the space of the original upper crust. Such exhumation may be associated with a strong diapiric mantle upwelling, as modelled by *Ellis et al.* (2011). However, the shear-velocity profile in this region resembles a mantle structure controlled by adiabatic upwelling. Figure 3.7a shows the comparisons of our result to the East Pacific Rise (*Gu et al.*, 2005), as well as the calculated shear velocities of dry olivine using the parameterization of *Jackson and Faul* (2010), with the assumptions of 1-cm grain size, $1350^{\circ}C$ potential temperature, and adiabatic geotherm extending up to the base of the crust. The slightly slower observed velocity in this study at >60 km depth compared to the predicted shear velocity of dry olivine may be caused by slightly higher potential temperature (*Dalton et al.*, 2014), presence of water and partial melt (*Braun*, 2000), and/or smaller grain size (*Jackson and Faul*, 2010).

The faster upper-most mantle lid (25-40 km) may represent the thinned remnant of the pre-rift continental lithosphere, perhaps thermally or compositionally modified by the rifting process (e.g. *Schmeling and Wallner*, 2012). While highly extended continental crust is well documented in mature rifts (e.g. *Keranen et al.*, 2009) and rifted margins (*Shillington et al.*, 2006), observations of thinned mantle lithosphere are relatively few. *Dugda et al.* (2007) find

evidence for a thin seismic lid beneath the main Ethiopian rift, with velocities very similar to those observed here. They interpreted the lid as continental lithosphere that was thermally modified by plume impingement associated with rifting, producing velocities that are lower than in the surrounding, unextended lithosphere. There is no evidence for significant thermal perturbation prior to extension in our region, but the velocities in the lid beneath the DEI are lower than in the surrounding peninsula and Trobriand plateau (Figure 3.7). The pre-rift lithosphere was likely a complex mélange built up by a recent history of subduction and arc-continent collision (e.g. *Webb et al.*, 2014; *Malusà et al.*, 2015), and this perhaps explains the velocity heterogeneity within the lithosphere. However, it is also plausible that the processes of lower-crustal exhumation and associated volcanism resulted in localized thermal and/or compositional modification of the extended lithosphere, similar to in the case in Ethiopia.

Beneath the Kiribisi Basin, west of Goodenough Island, no clear velocity discontinuities can be observed from 10 to 60 km depth (Figure 3.7b). The Kiribisi Basin is a shallow-water area with presumably thick crust extending north from the Papuan Peninsula, where a seismic refraction study estimates a crustal thickness of ∼25 km (*Finlayson et al.*, 1977). *Fitz and Mann* (2013) use sedimentary records to demonstrate very little (∼2-10 km) upper crust extension within the Kiribisi basin since late Miocene, although faults identified on reflection seismic records sometimes underestimate crustal extension by a significant amount (*Reston*, 2007).

We interpret this region as having a crust about 30 km thick (Figure 3.10), with relatively fast lower crust and very slow upper mantle, so the velocity contrast between crustal and mantle rocks is small. *Finlayson et al.* (1977) reports the P velocity of the lower crust beneath the west Kiribisi Basin is around 6.5-7.0 km/s, which agrees well with the 3.8 km/s S velocity that we observe, assuming an approximate V_p/V_s ratio of 1.80 (*Ferris et al.*, 2006). Combined with the very low mantle shear velocities (3.9-4.1 km/s) observed in this region, the seismic expression of the Moho is minimal. The interpretation of the slow mantle velocities is discussed in the next section; in terms of lithospheric breakup, they suggest that

such extension is embryonic, and has not yet significantly impacted the crustal structure.

While there is little expression of crustal thinning over thinned mantle lithosphere west of the DI, there is evidence of the extensional processes stepping southwards from Goodenough Island onto the Papuan Peninsula. The basin structure southwest of Goodenough Island shows signs of recent extensional faults (*Fitz and Mann*, 2013) and is delineated by a band of active seismicity (*Dieck et al.*, 2013). The Dayman Dome massif has been interpreted to be an extensional core complex (e.g. *Daczko et al.*, 2011). The zone of low velocities in the mantle beneath the Kiribisi Basin clearly do not correlate with the trend or locations of these structures. The crustal thickness within the transfer basin southwest of Goodenough Island cannot be well resolved, but stations near Dayman Dome show no evidence of thinned crust in either receiver functions (*Abers et al.*, 2012; *Obrebski et al.*, 2014) or surface-wave velocities.

3.4.2 Upper mantle structure of the Kiribisi Basin

One of the most interesting observations of this study is the extremely slow anomaly ($\sim$4.0 km/s) at upper mantle depth beneath the Kiribisi Basin, near 9.4°S, 149.9°E, west of Goodenough Island (e.g., 30-60 km depth, Figure 3.9). Several mechanisms can affect shear velocity in the upper mantle, including temperature variation, composition, and existence of partial melt. Here we present two possible interpretations of this observation.

The first interpretation is based on the notion that the slow anomaly is generated by temperature variation and partial melt. *Abers et al.* (2002) suggest a 300-700°C temperature difference in the uppermost mantle beneath the eastern DI compared to the surrounding continental lithosphere, if the P-velocity slow anomaly is interpreted only as a result of temperature variation. *Eilon et al.* (2015) demonstrate that at $\sim$90 km depth large (700°C) thermal gradients exist in the mantle between the rift axis and a fast, seismogenic structure to the north. At 30-60 km depth, the shear velocity in the western Kiribisi Basin is 0.2-0.3 km/s slower than the upper mantle beneath the eastern DI. This is surprising because of the

smaller amount of extension in the west. If we try to explain this velocity contrast by purely thermal variation of melt-free dry olivine, it would imply temperatures around $100 - 200°C$ higher than the adiabatic geotherm at 30-60 km depth, based on the approach of *Jackson and Faul* (2010), and assuming a constant grain size of 1 cm.

For a peridotitic mantle, velocities this low at this depth imply the presence of melt. The presence of water (perhaps emplaced during the long history of subduction in the region) could combine with temperature to lower velocities, but the degree of water necessary would lower the melting temperature such that melting would be induced in this regime as well. It is difficult to determine the abundance of partial melt just by isotropic shear velocity alone, because the melt distribution have great effect on shear velocity and anisotropy (*Bastow et al.*, 2010). Most studies suggest 2-10 % of shear velocity reduction for each percent of partial melt (e.g. *Takei*, 2002; *Hammond and Humphreys*, 2000; *Takei and Holtzman*, 2009), which is more than enough to explain our observation without much temperature variation.

Why the mantle beneath the less-extended Kiribisi Basin is slower relative to the extended region beneath the DI is unclear. One possible interpretation is that, in the west, the slower and less localized extension near the surface, together with the un-thinned continental crust, inhibits melt extraction, and facilitates partial-melt accumulation in the upper mantle. This phenomenon has been proposed in mid-ocean ridge environments where melt production outpaces melt extraction (e.g. *Lizarralde et al.*, 2004; *Gaherty and Dunn*, 2007; *Wei et al.*, 2015). Teleseismic body-wave tomography (*Eilon et al.*, 2015) observes low velocities and thus high temperatures at larger depth (>90 km) beneath this region, and thus mantle upwelling may be inducing melting that shallow extension has yet to tap.

In the east, on the other hand, the crustal thinning (*Abers et al.*, 2002), dike intrusion (e.g. *Little et al.*, 2011), and local volcanism (e.g. *Smith*, 1976; *Baldwin et al.*, 2012) on the DI facilitate melt extraction and cooling of the upper mantle. Furthermore, the eastern DI are within 100 km of the Woodlark spreading center tip. Melt extraction associated with building modern oceanic crust may induce an eastward melt propagation, which also helps

to generate a E-W gradient of melt abundance in the upper mantle between the eastern DI and the Kiribisi Basin.

The alternative interpretation of the slow anomaly is based on a possible compositional difference. The gneiss domes that form the DI contain a significant amount of felsic material, some of which was subducted to the depth of ∼100 km prior to exhumation (e.g. *Baldwin et al.*, 2008; *Little et al.*, 2011). The U-Pb zircon geochronologic analysis from the Fergusson Island samples yields an exhumation history that suggests the UHP metamorphic eclogites stalled beneath the crust for ∼1 Ma, before they were finally exhumed to the surface (*Gordon et al.*, 2012). Meanwhile, the exhumation propagates to the west, as shown by a westward younging of the $^{40}Ar/^{39}Ar$ cooling ages of the HP samples within the DI (*Baldwin et al.*, 1993). These observations suggest the possible presence of felsic, crustal materials in the mantle west of Goodenough Island. This material would have been emplaced through the same (likely subduction-related) process that produced the DI UHP facies, but it has not yet been exhumed.

We evaluate whether a mix of crustal and mantle rocks can explain the slower upper mantle (30-60 km) shear velocity beneath the Kiribisi Basin compared to the eastern DI, where the UHP rocks have been exhumed. *Brownlee et al.* (2011) investigate the samples collected from the DI, and estimate their seismic velocities at depth. Based on their calculation, the quartzofeldspathic gneiss, which is the dominant composition of the gneiss domes, has a shear velocity of ∼3.7 km/s at the depth of 30-60 km, assuming a temperature of $700°C$. The shear velocity of melt-free olivine at the same P-T condition is 4.6 km/s if 1 cm grain size is assumed (*Jackson and Faul*, 2010). The average shear velocity we observed in the upper-most mantle beneath the Kiribisi Basin is around 4.0 km/s. In order to achieve this value, about 62 % of the mantle volume should be occupied by quartzofeldspathic gneiss (using a Voigt-Reuss-Hill average).

This tectonic setup is similar to the numerical diapir model of *Ellis et al.* (2011). However, the model requires a 22-km-radius subducted crustal body that is mostly made of gneiss,

and consists of roughly 10-20% partial melt during exhumation. These conditions would lead to a shear velocity value much slower than our observation. While the limited resolution of surface wave tomography (*Bodin and Maupin*, 2008) allows for small partial-melt crustal bodies at upper mantle depth, the size must be much smaller than that modeled by *Ellis et al.* (2011). Further modeling studies are needed to determine the conditions under which a mixed felsic-mafic body at depth would provide sufficient buoyancy to drive exhumation, while still meeting the constraints of seismic observations.

3.5 Conclusion

We retrieve a 3D shear-velocity model in the area near the D'Entrecasteaux Islands, Papua New Guinea using both ambient noise and earthquake Rayleigh-wave phase-velocity measurements.

The results indicate a localized upper-mantle extension along the Woodlark Rift axis, which favors the exhumation of the UHP rocks exposed on the DI. In the eastern DI, the deeper velocity structure (>50km) is close to the prediction of an adiabatic upwelling mantle, with a slightly faster shallow mantle that may be associated with the extended continental lithosphere. There is no evidence of an ultra slow diapir-like structure (*Ellis et al.*, 2011) presently beneath the DI.

We discover the shallow mantle beneath the Kiribisi Basin west of the DI is slower than the mantle beneath the more extended eastern DI at the same depth. We provide two possible interpretations of this observation: more partial melt accumulates in the west because of the less melt extraction; and/or there are un-exhumed felsic crustal material at mantle depth, mixed with peridotitic mantle west of the DI. In either scenario, the degree of partial melt is modest. This low-velocity anomaly is spatially decoupled from the surface expression of extension west of the DI, which occurs 10s of km south on the Papuan Peninsula.

Acknowledgments

We thank the IRIS-PASSCAL Instrument Center for providing instruments and field support, as well as Hugh Davies for facilitating the fieldwork. For the field deployment, we are grateful to J. Calkins, P. Ruprecht, T. Koczynski, P. Irarue, and R. Verave (UPNG/MRA), J. Oa and E. Nidkambu (National Mapping) for their efforts. The OBS were provided by the OBS lab at Scripps Institute of Oceanography, through the OBS Instrumentation Program funded by the Division of Ocean Science at NSF. This research was supported by NSF grants EAR-0814236 (Abers) and EAR-0708445 (Gaherty). The seismic data used in this study can be acquired through the IRIS Data Management Center (http://ds.iris.edu/ds/nodes/dmc).

Chapter 4

Love-Wave Phase-velocity Estimation in the Presence of Multi-mode Interference

[1]

abstract

The propagation of Love waves contains important information to constrain mantle radial anisotropy. The measurements of Love-wave fundamental-mode phase velocities are usually contaminated by the first overtone interference, due to their similar group velocities. We simulate the interference effect on phase-velocity measurements using two plane waves traveling at different phase velocities. The simulation results indicate an asymmetric interference pattern in phase measurements that may lead to systemic bias. We propose a correction scheme that utilizes amplitude measurements to correct for the interference. The synthetic tests suggest the correction can significantly reduce the phase-velocity variance and bias generated by the interference.

[1]AUTHORS: Ge Jin[a]*, James Gaherty[a], Anna Foster[b], Pei-ying Lin[a]
[a] Lamont-Doherty Earth Observatory, Columbia University, 61 Route 9W, Palisades, NY 10964, USA
[b] Earth Observatory of Singapore
* corresponding author: ge.jin@ldeo.columbia.edu

4.1 Interference Pattern

Global and regional observations suggest that Love-wave phase-velocity measurements show a systematic variation with epicentral distance that can be explained by the interference between 0T and 1T (*Nettles and Dziewoński*, 2011; *Foster et al.*, 2014b). The interference produces a systematic variation in amplitude and phase that, for array recordings of an earthquake at teleseismic distance ($> 30°$), can be well reproduced by the interference between two plane waves with different phase velocities corresponding to 0T and 1T. In this study, we ignore multi-pathing and ray-bending effects (discussed in Section 4.4), and assume the structure is homogeneous within the array.

Assuming a wavefield dominated by 0T and 1T, the observed Love wave from an earthquake can be represented as:

$$u(X,t) = A(\omega)e^{-i(\omega t+\varphi)} = A_0(\omega)e^{-i(\omega t-k_0X+\Phi_0)} + A_1(\omega)e^{-i(\omega t-k_1X+\Phi_1)}. \tag{4.1}$$

A and φ are the amplitude and phase of the entire waveform. A_0 and A_1 are the amplitudes of 0T and 1T, respectively. k_0 and k_1 are the corresponding average wavenumbers along the path, Φ_0 and Φ_1 are the initial phases of 0T and 1T at the source, X is the epicentral distance, and ω is the angular frequency. The wavenumber k can also be presented as $k = \omega/c$, where c is the phase velocity. This wavefield summation at a certain location can be simplified as the summation of two vectors, as demonstrated in Figure 4.1, where $\varphi_0 = -k_0X + \Phi_0$ and $\varphi_1 = -k_1X + \Phi_1$. The amplitude A and phase φ of the entire wavefield is controlled by the amplitudes A_0 and A_1, and the phase difference $\varphi_1 - \varphi_0$.

Most array-based methods evaluate phase velocity from the local phase gradient, which is associated with the estimation of relative phase variation between stations. If the measurements are free of overtone interference, where $A_1 = 0$, then the phase variation $\delta\varphi$ between the two stations at the same time can be simply presented as:

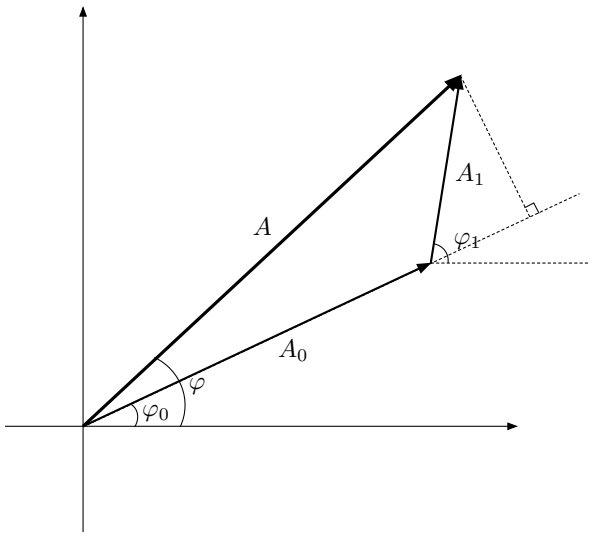

Figure 4.1: Demonstration of the wave field summation for equation 4.1.

$$\delta\varphi = k_0 \delta X \tag{4.2}$$

where δX is the difference of their epicentral distance.

If the amplitude of 1T is small ($A_1 \ll A_0$), the phase variation, which is defined as the phase difference from the single-mode situation, can be approximated as:

$$\delta\varphi = k_0 \delta X + \frac{A_1}{A_0} \sin[(k_1 - k_0)\delta X + \delta\Phi] \tag{4.3}$$

where $\delta\Phi$ is the phase difference between 0T and 1T at a certain station. The amplitude variation can be presented as:

$$A = A_0 + A_1 \cos[(k_1 - k_0)\delta X + \delta\Phi] \tag{4.4}$$

In this case, the apparent wavenumber k', which is defined as a local phase gradient, can be presented as:

$$k' = k_0 \left\{ 1 + \frac{A_1}{A_0} \frac{k_1 - k_0}{k_0} \cos[(k_1 - k_0)\delta X + \delta\Phi] \right\} \tag{4.5}$$

The apparent wavenumber oscillates around the wavenumber of 0T, with the magnitude of the oscillation proportional to the amplitude ratio and the wavenumber discrepancy between the two modes. The interference wavelength L can be obtained by:

$$L = \left| \frac{2\pi}{k_1 - k_0} \right| = T \left| \frac{c_0 c_1}{c_0 - c_1} \right| \tag{4.6}$$

In order to verify our approximation, we designed a synthetic experiment. The single-frequency waveforms of 0T and 1T are approximated as Gaussian-enveloped cosine functions, providing a total wavefield defined as:

$$u(X,t) = A_0 \exp(-\frac{(t-t_g)^2}{2\sigma^2}) e^{-i(\omega t - k_0 X)} + A_1 \exp(-\frac{(t-t_g)^2}{2\sigma^2}) e^{-i(\omega t - k_1 X)} \tag{4.7}$$

where t_g is the group delay, which is assumed to be the same for both modes, and σ controls the width of the wavelet. The phase and amplitude are measured at the peak of the envelope function of $u(X,t)$ using the FTAN method (*Levshin et al.*, 1992). The apparent phase velocity between two locations is defined as:

$$c' = \frac{X_2 - X_1}{t_{g2} - t_{g1} - (\varphi_2 - \varphi_1 + 2\pi N)/\omega} \tag{4.8}$$

where φ_1 and φ_2 are the phase measurements at these two locations. N is an integer to correct cycle skipping.

Figure 4.2a shows an example of this simulation at a period of 40 s. In this case, we assume the amplitude of 1T is 10% of the amplitude of 0T, with the two modes traveling at the same group velocity and phase velocities calculated from PREM (*Dziewonski and Anderson*, 1981) (4.3838 and 4.8773 km/s for 0T and 1T, respectively). The phase and amplitude at each epicentral distance are calculated via Equation 4.1. The upper and middle panels of

Figure 4.2a depict the amplitude and phase relative to the fundamental mode (A/A_0 and $\varphi - \varphi_0$, respectively), while the red-dashed lines show the approximations of Equations 4.3 and 4.4. In the bottom panel, the apparent phase velocities are estimated by using station pairs centered at every 0.1° along the great-circle path. We vary inter-station distance from 0.2° to 5° to evaluate its effect on the phase-velocity estimation. Using Equations 4.5 and 4.6, we calculate that the interference should produce 1% phase velocity variations, with an interference wavelength of around 1733 km, which is consistent with the simulation in Figure 4.2a.

If the two waves have more comparable amplitudes, Equation 4.3 becomes less accurate, while Equation 4.6 is still correct. Figure 4.2b depicts the same simulation, but with an amplitude ratio between the two modes of 0.5. The interference wavelength is unchanged, while the phase and amplitude variation as a function of distance becomes asymmetric. The phase variation goes up to 0.55 rad, which is equivalent to 3.5 s of travel time for 40-s period. The result shows that the interference generates about 50% variation in amplitude and 10% in phase velocity.

The asymmetry of the interference pattern is more obvious when the amplitudes of the two modes are close, as shown in Figure 4.2c. In this case, the amplitude ratio between 1T and 0T is set to be 0.9, and up to 50% phase-velocity variation can be observed. It is worth noting that for the majority of the interference cycle, the apparent phase velocity is stable and biased to be faster than the fundamental-mode phase velocity. This may contribute to the systematic bias in Love-wave phase-velocity measurements observed in *Foster et al.* (2014a,b) and *Jin and Gaherty* (2015).

The apparent phase velocity is fastest where the two modes are in phase. The apparent wavenumber at this location can be presented as:

$$k'_{peak} = k_0 + \frac{A_1}{A_0 + A_1}(k_1 - k_0) \tag{4.9}$$

which corresponds to apparent phase velocity of:

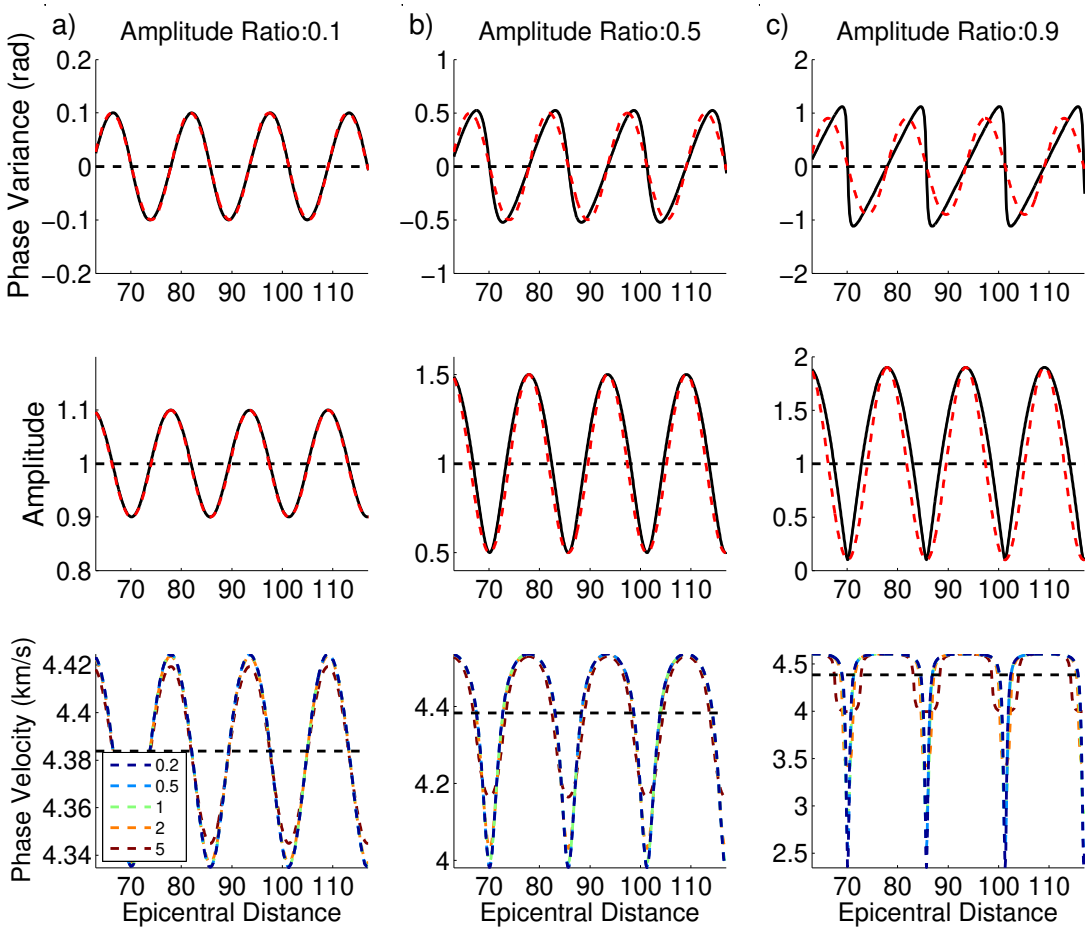

Figure 4.2: Interference pattern for different amplitude ratio between 1T and 0T. a) Interference pattern for an amplitude ratio equals to 10%. Upper: phase variations from the 0T phase velocity prediction. Red dashed line shows the prediction of Equation 4.3. Mid: Amplitude variations. Red dashed line shows the prediction of Equation 4.4. Lower: phase velocity estimations at different epicentral distances using the two-station method (Equation 4.8). Colored dashed lines show the measurements with different station spacing, from 0.2° to 5°. b) same as a, but for an amplitude ratio equal to 50%. c) same as a, but for an amplitude ratio equal to 90%. Note that the range in y axes for all three observables increase substantially from a) to c).

$$c'_{peak} = \frac{(A_0 + A_1)c_0c_1}{A_0c_1 + A_1c_0} \tag{4.10}$$

The slowest apparent phase velocity is observed where the two modes are out of phase by π:

$$k'_{trough} = k_0 - \frac{A_1}{A_0 - A_1}(k_1 - k_0) \tag{4.11}$$

$$c'_{trough} = \frac{(A_0 - A_1)c_0c_1}{A_0c_1 - A_1c_0} \tag{4.12}$$

When A_1 is close to A_0, the value of c'_{trough} is much farther from c_0 than the value of c'_{peak} is from c_0, producing the asymmetric pattern in Figure 4.2c.

The measured phase velocity also depends on the distance between the stations used to estimate the phase gradient. The lower panels of Figure 4.2 show phase-velocity estimations using the two-station method with various inter-station distances. Larger station spacing tends to have smaller bias, because the phase variation is averaged out along the longer inter-station path. This is consistent with the observations of *Foster et al.* (2014a) and *Jin and Gaherty* (2015), that the phase-velocity estimates across USArray using only distant station pairs have smaller bias than the results of local-array gradient methods that utilize observations from closely spaced stations.

Depending on the earthquake focal mechanism and the propagation path, it is possible that the amplitudes of overtones are larger than that of 0T. In that case, the apparent phase velocity oscillates around the overtone's phase velocity, and the interference pattern is similar to Figure 4.2.

4.2 Quasi-Helmholtz Correction

The Helmholtz equation was first used in the field of surface-wave measurement by *Lin and Ritzwoller* (2011), to reduce the effect of multi-pathing interference. The Helmholtz equation can be presented in terms of the wavenumber as:

$$k^2 = k'^2 - \frac{\nabla^2 A}{A} \tag{4.13}$$

where k is structural wavenumber, k' is apparent wavenumber, and $\nabla^2 A$ is the Laplacian term of the wave amplitude. Equation 4.13 is only valid for the single-mode situation and does not work if another wave co-exists with a different phase velocity.

However, the phase and amplitude variations due to the dual-mode interference are highly correlated (Figure 4.2). This implies the possibility of using the amplitude field to correct the bias in apparent phase velocity, even under the existence of multiple modes. Equation 4.13 can be modified to conditionally correct for dual-mode interference as:

$$k^2 = k'^2 - \alpha \frac{\nabla^2 A}{A} \tag{4.14}$$

where α is a constant to compensate for the discrepancy of the two velocities.

We start with the simple case of $A_1 \ll A_0$. In this case, the apparent wavenumber is approximated by Equation 4.5, and the amplitude is presented by Equation 4.4. By substituting Equations 4.4 and 4.5 into Equation 4.14, and ignoring second-order terms, we have:

$$k^2 = k_0^2 + [2k_0(k_1 - k_0) + \alpha(k_1 - k_0)^2]\frac{A_1}{A_0}\cos(k_1 - k_0)\delta X \tag{4.15}$$

The interference effect can be removed by forcing $k = k_0$. The constant α can then be obtained as:

$$\alpha = \frac{2k_0}{k_0 - k_1} = \frac{2c_1}{c_1 - c_0} \tag{4.16}$$

Equation 4.16 is only accurate if $A_1 \ll A_0$. However, it can significantly reduce the interference bias even if A_0 and A_1 are more comparable.

The corrected phase-velocity measurements using α calculated from Equation 4.16 are

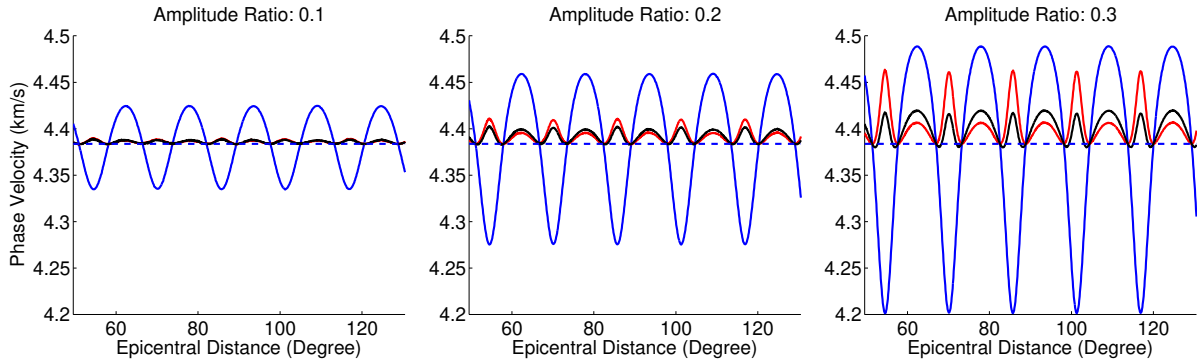

Figure 4.3: Effect of quasi-Helmholtz correction on the phase velocity for different amplitude ratios. Blue line: uncorrected phase-velocity measurements. Red line: corrected phase-velocity measurements using α estimated from Equation 4.16. Black line: corrected phase velocity using α inverted from data. Blue line: true 0T phase velocity.

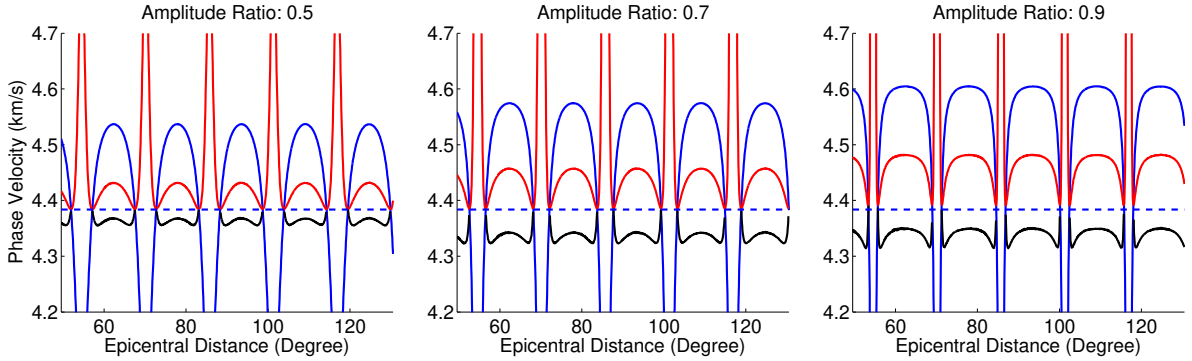

Figure 4.4: Same as Figure 4.3, but for larger amplitude ratios, only the portion with $\nabla^2 A > 0$ is used to estimate α and apply the correction.

shown as the red lines in Figures 4.3 and 4.4, for simulated data with various A_1/A_0 ratios ranging from 0.1 to 0.9. The results suggest that the correction significantly reduces the phase-velocity variations due to the interference. As the amplitude ratio increases, the correction becomes less accurate: it undercorrects the constructively interfering portion while overcorrecting the destructively interfering portion, due to the asymmetric pattern described by Equation 4.9-4.12.

For real observations, c_0 and c_1 are unknown, but α can be directly inverted from the measurements, by minimizing the standard deviation of the phase velocities measured from different events. The phase-velocity measurements corrected using the inverted α are shown

as black lines in Figures 4.3 and 4.4.

The correction with inverted α can reduce phase velocity variation to <1% for the cases with amplitude ratio between the two modes smaller than 0.3. It does, however, introduce a small but systematic bias into the averaged phase velocity. This bias is less than 0.5% even when the interfering wave has an amplitude of 30% of the main wave.

If the amplitudes of the two modes are more comparable, as in Figure 4.4, the overcorrection of the destructively interfering portion becomes significant. Further improvements of the correction can be achieved by discarding the measurements associated with the most destructively interfering portion, where $\nabla^2 A$ is positive. This is reasonable in observed data, as destructive interference produces small amplitudes that leads to low signal to noise ratio (SNR) measurements.

The black lines in Figure 4.4 depict the correction with α inverted using only the measurements with negative $\nabla^2 A$. The improvement after the correction is significant, with the systematic bias even smaller than the bias from the theoretical α obtained from Equation 4.16. The bias, in the extreme case with the amplitude ratio being 0.9, is less than 1.5%, as compared to 4.5% in the original uncorrected measurements.

For real earthquakes, the amplitude ratio between 1T and 0T is variable for each event, depending on the source mechanism, the structure along the path, and possibly how the waveforms are windowed for analysis. We perform another synthetic test to simulate this situation. Fifty events are generated with random A_1/A_0 ratios ranging from 0.3 to 0.7. Phase and amplitude are measured at a random epicentral distance between 20 and 160 degrees using 5 stations with 10 km spacing to calculate the phase gradient k and amplitude Laplacian term $\nabla^2 A$. Measurements with positive $\nabla^2 A$ are discarded. The correction term α is inverted by minimizing the standard deviation of the corrected phase velocities from all 50 events. The results of this test are shown in the left panel of Figure 4.5. The correction significantly stabilizes the phase velocity measurements.

We then repeat the test 100 times, and calculate the median values of the phase velocities

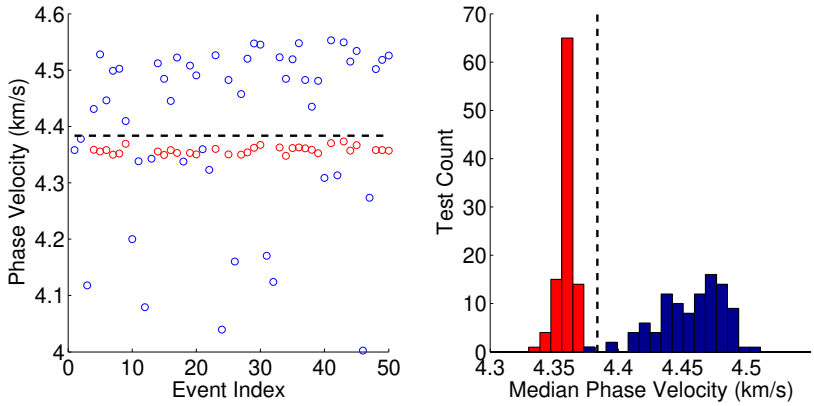

Figure 4.5: Synthetic test with random amplitude ratio and epicentral distance. Left panel: result from a single test with 50 randomly parameterized events. Blue circles show uncorrected phase-velocity measurements, red circles are corrected phase-velocity measurements. Right panel: histogram of the median phase velocities of corrected (red) and uncorrected (blue) phase velocities of 100 tests. In both panels, black dashed line show the true phase velocity.

before and after the correction. The comparison is shown in the right panel of Figure 4.5. Although still slightly biased (∼0.5%), now to slower velocity, the phase velocity estimation becomes much more robust and reliable after the correction.

4.3 Application to Synthetic Seismic Data

In order to further verify the robustness of this correction, we apply it to synthetic seismic datasets generated from two earth models using MINEOS. The receiver locations are shown in Figure 4.6. This array geometry can provide good estimates of local phase and amplitude gradients regardless of the incoming wave direction.

The CMT solutions (*Dziewonski et al.*, 1981; *Ekström et al.*, 2012) from 29 events with magnitude larger than 6.5 and depth shallower than 50 km in 2012 are selected to generate synthetic waveforms. Examples of the synthetic waveforms are shown in Figure 4.7. The phase and amplitude measurements at the periods of 25-200 s are obtained using the Automated Surface-Wave Measuring System (*Jin and Gaherty*, 2015). We use a linear regression between the phase and the epicentral distance to estimate the phase gradient (apparent phase

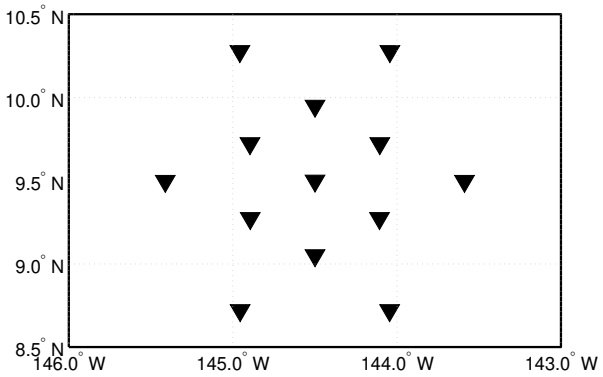

Figure 4.6: Array geometry for the seismic synthetic test in Section 4.3.

velocity), and the amplitude Laplacian term is obtained by fitting a second-order polynomial to the amplitude as a function of epicentral distance.

The first model we adopt is a continental mantle model appropriate for western North America (TNA), with a 40-km thick crust (*Walck*, 1984; *Grand and Helmberger*, 1984). The group and phase velocities calculated from the model, along with the amplitude ratios between the first two overtones and 0T are shown in Figure 4.8. At the 100-s period, the amplitude ratio between 1T and 0T is around 0.3, which is consistent with the observations of *Foster et al.* (2014b) on USArray data.

We first generate a set of waveforms that include only 0T and 1T, which are the main phases affecting fundamental-mode Love-wave measurements (*Nettles and Dziewoński*, 2011; *Foster et al.*, 2014b). The uncorrected and corrected measured phase velocities are shown in Figure 4.9a, with the median and stardard variation of the phase velocities at each period shown in the right panel. The variations in phase velocity decreases significantly after the correction, with the bias in the median phase velocity almost eliminated.

There are some slight discrepancies between these results and the results from the purely two-plane-wave interference test in Figure 4.5. For example, the velocity variations in the corrected measurements are larger in the mode-summation synthetic seismic test. This might be due to ignoring the source radiation pattern for individual events. The radiation pattern

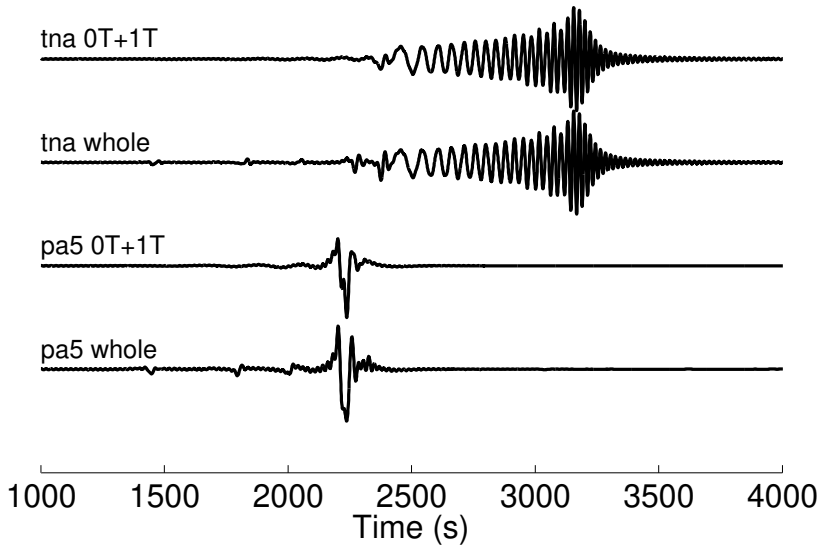

Figure 4.7: Examples of the synthetic seismograms for different models and mode summations. The centroid moment tensor of the 6.7Mw earthquake near the Negros, Philippines on Feb. 6th, 2012 is used to generate the waveforms.

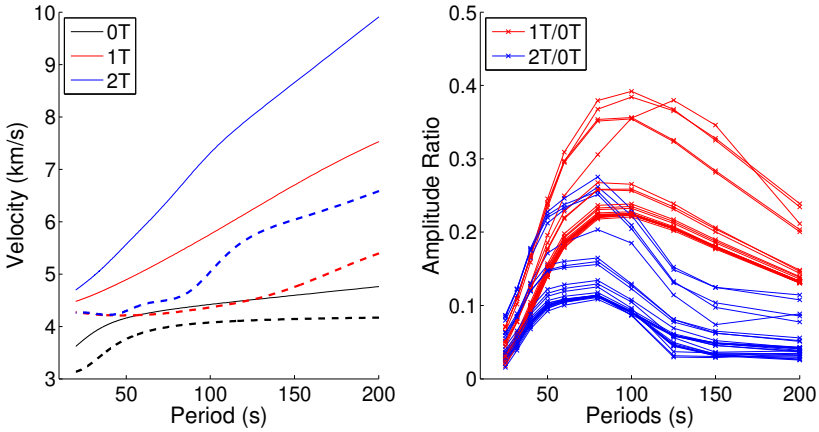

Figure 4.8: Dispersion curves and amplitude ratios for the continental model and focal mechanisms used. Left: phase (solid lines) and group (dashed thick lines) velocities of the fundamental mode and the first two overtones. Right: amplitude ratio of the overtones to 0T, for all events.

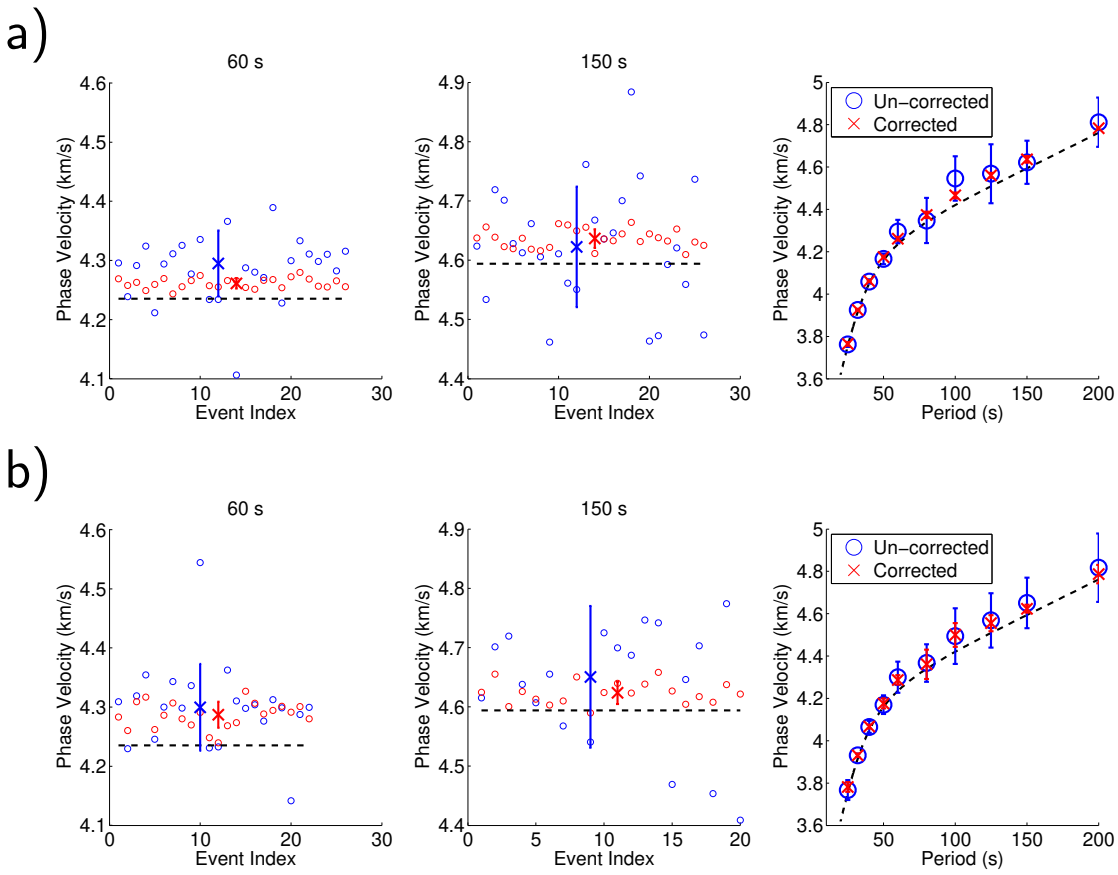

Figure 4.9: Phase-velocity measurements from seismograms calculated using the continental model, for all qualified events. a) Results for seismograms using only the summation of 0T and 1T. Left: phase-velocity measurements of individual events at 60-s period. Blue circles are un-corrected phase velocities, with the median and standard deviation displayed by the blue errorbar. Red circles and errorbar are for the corrected velocities. Middle: same as the left panel but for 150-s period. Right: medians and standard deviations of all qualified phase-velocity measurements at different periods. b) same as a), but for the full synthetic waveforms (up to 20T). Dashed lines show the true phase velocity of 0T in all panels.

for Love waves has a 4-θ variation in azimuth for most focal mechanisms. If the azimuth to the array is close to a nodal plane direction, a significant amplitude variation will exist in the tangential direction, and the amplitude ratio between 0T and 1T may vary as well. This variation may still produce some errors in both phase and amplitude gradient estimation, though it can be partly compensated for by only fitting the phase and amplitude gradients in the radial direction. Some events have to be excluded in this test if they produce abnormal phase and amplitude measurements. We exclude those events automatically by requiring a linear dependence between $1/c^2$ and $\nabla^2 A$.

Nevertheless, the improvement from the correction is remarkable. For the periods affected by overtone interference (60-200 s), the standard deviations of the phase velocities are decreased by up to 90%, and the median-velocity biases are less than 1%.

We then perform the same test on full synthetic waveforms (including up to the 20th overtones), and the results are very similar, except for the slightly larger variations in both uncorrected and corrected phase velocities (Figure 4.9b), probably due to the interference from the second overtone (Figure 4.8).

Compared to continental structure, oceanic mantle models with a high-velocity lid overlying a distinct low-velocity zone can generate larger overtone interference both due to greater overtone excitation (especially at shorter periods) and less discrepancy between the group velocities for different modes. We adopt an oceanic velocity model (PA5) from *Gaherty et al.* (1996) to perform the same tests, using the same event set. Dispersion curves and amplitude ratios between the modes calculated using this model are shown in Figure 4.10. In this case, the group velocities of the fundamental mode and first two overtones (1T and 2T) are similar at most frequencies, and the amplitudes of 1T and 2T are both comparable to or larger than 0T at periods of less than 100 s.

We first consider synthetic waveforms containing 0T and 1T only. The estimated phase velocities before and after the correction are shown in Figure 4.11a. The results are more complicated than for the continental case, as the dominant mode changes with frequency.

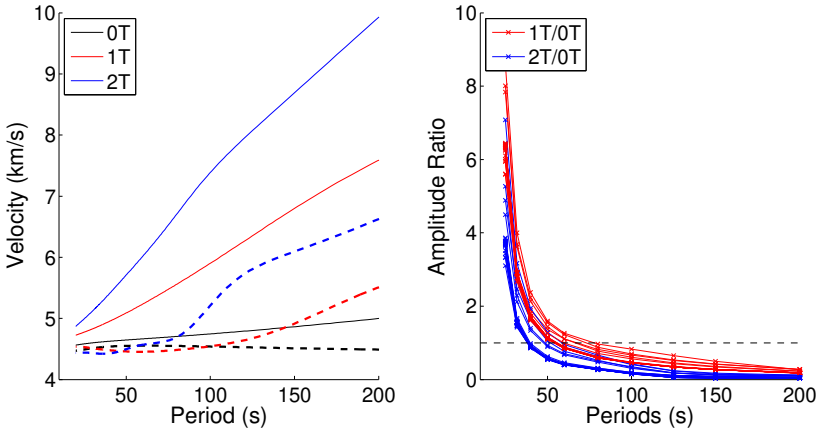

Figure 4.10: Same as Figure 4.8, but for the oceanic model. The horizontal dashed line in the right panel depict the location where the amplitude ratio equals 1.

At short periods (<50 s), the amplitude of 1T is larger than that of 0T, so the corrected phase velocity corresponds to 1T; at long periods (>60 s), 0T becomes the dominant mode, and the corrected phase velocities are for 0T. In the middle bands (∼60 s), the dominant mode is ambiguous, and the correction does not work in this case.

At 50-s period, although 1T is always larger than 0T for all events, the amplitude ratios are close to 1. The measured uncorrected phase velocities have small standard deviations but are obviously biased. This demonstrates the case that when the amplitudes of two interfering waves are similar, and the majority of the interference cycle is biased to a nearly constant phase velocity (Figure 4.2c). If the measurements from all the events have epicentral distance in this portion of the interference cycle, the correction scheme does not work since there is too little amplitude and/or phase variation observed to improve the consistency between events.

For both the short-period and the long-period cases, the correction successfully reduces variance and generally reduces the bias of the phase velocities. At longer periods (80-125 s), the amplitudes of the two modes are sufficiently close that measurements with positive $\nabla^2 A$ are discarded, and the corrected phase velocities show an over-correction as in Figure 4.5.

Applying the correction scheme to full synthetic waveforms for the oceanic model pro-

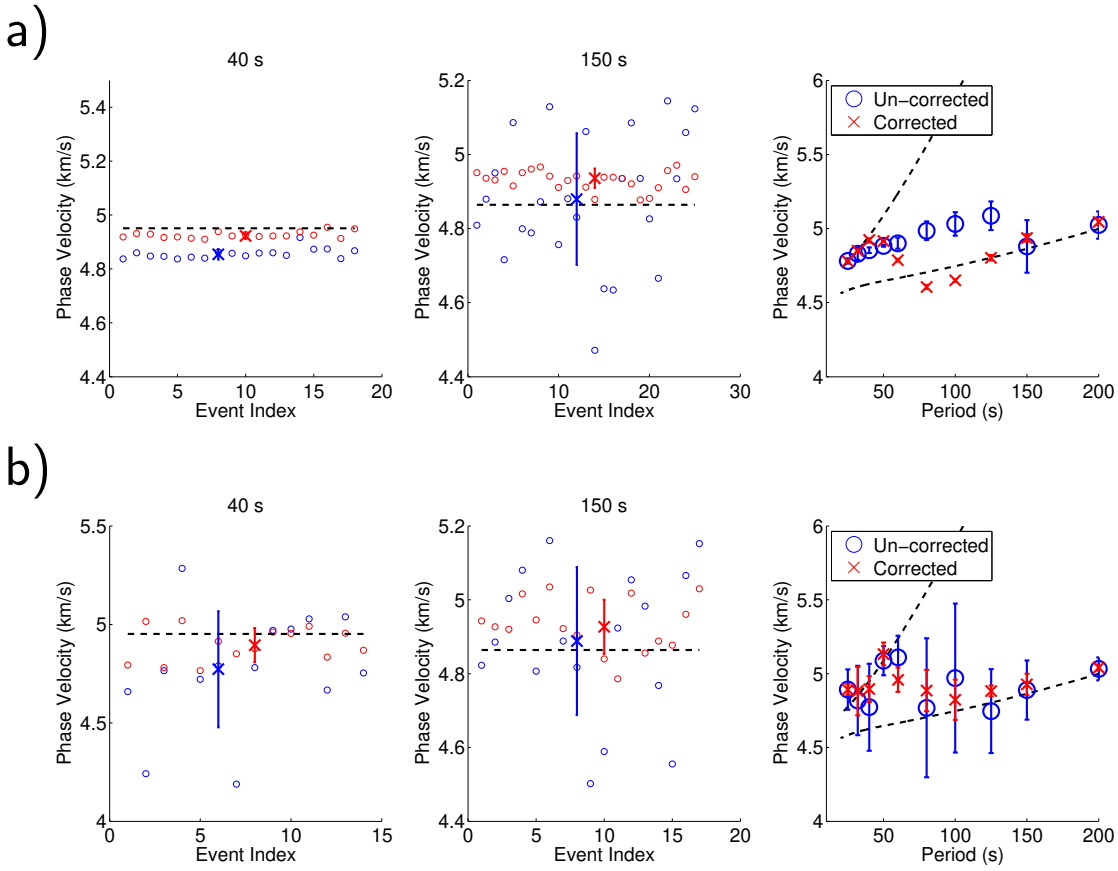

Figure 4.11: Same as Figure 4.9, but for the oceanic model. The dashed lines in the left panels depict the true phase velocity of 1T, while the dashed lines in the middle panels show that of 0T.

duces similar results (Figure 4.11b), but with larger scatter and uncertainty due to the complexity of the interference. For Love-wave propagation in such structures, both 1T and 2T provide strong interference for 0T, with 1T generally about 2 times larger than 2T, but both significantly larger that 0T at periods < 50 s. Although the quasi-Helmholtz correction is designed to work with only two interfering waves, it is able to stabilize the phase-velocity estimates considerably even in this multi-mode case, converging to robust estimates for 1T at short periods (25-50 s), and for 0T at long periods (>100 s). In both period bands, the standard deviation after correction is larger than the two-mode case, and the bias at long period remains as high as 2%.

4.4 Discussion

We have developed a quasi-Helmholtz data-processing scheme for reducing or removing bias and uncertainty in Love-wave phase-velocity measurement that arises due to multi-mode interference. The synthetic tests presented in Sections 4.2 and 4.3 suggest that the efficacy of the correction is dependent on the relative amplitudes of the dominant mode branches, with the algorithm becoming increasingly ineffective as the mode amplitudes converge to a common value. The amplitude ratio between 0T and its overtones are determined by the source excitation, propagation path, structure near the receiver, and the details of the window function applied to isolate surface-wave energy during the measurement. For realistic 1D Earth models, the relative amplitudes vary substantially between models and as a function of frequency. While it is commonly the case (and generally assumed) that the fundamental mode is the dominant branch, there can be cases where this is not true, and the algorithm allows for this circumstance, as demonstrated in Section 4.3. In these cases, the c_0 and c_1 terms are swapped in the quasi-Helmholtz correction equations, with the inversion for alpha resulting in a negative value. This works under the assumption that 1T $>$ 0T for all events at a given frequency; synthetic calculation of the mode amplitudes for assumed source depth

and excitation and propagation models can guide the event selection and inversion in these cases.

Application of this analysis to real data is the subject of a future paper, but the synthetic tests presented here suggest a number of considerations that will be important for successful application. First, strong lateral heterogeneity distorts the surface wavefield, causing interference between the waves traveling along adjacent paths (multi-pathing effect). This interference produces a much larger Laplacian term for the amplitude field than the overtone interference does, as the multi-pathing interference wavelength is much smaller than that of the dual-mode interference. α for the intra-branch interference is 1 (*Lin and Ritzwoller*, 2011), but is usually larger than 10 for the same-path dual-mode interference (Equation 4.16), which implies the amplitude variation from the multi-pathing effect may significant affect the dual-mode correction. Multi-pathing between mode branches would further add to the complexity. Despite this, observations of interference patterns within the heterogeneous North American continent (*Foster et al.*, 2014b) that are clearly consistent with the multimode interference modeled here imply that these effects can still be discerned through the presence of multipathing.

A second difficulty that real-data application may encounter is the low resolution and high noise level in the amplitude Laplacian term estimation. In order to obtain the second-order gradient of the amplitude field, 3-5 times more stations are required compared to the first-order gradient calculation (*Lin and Ritzwoller*, 2011; *Jin and Gaherty*, 2015). The finite difference calculation also introduces short-wavelength noise that has to be suppressed by aggressive smoothing (*Jin and Gaherty*, 2015). As a result, the correction should be applied to data from relatively homogeneous areas over which amplitude variations are smooth, and/or it should be used only over large spatial areas where the smoothed amplitude Laplacian accurately characterizes the large-scale average variations in amplitude behavior. A dense distribution of stations is important to robustly estimate this term as well.

Finally, the synthetic tests demonstrate that while the quasi-Helmholtz correction clearly

improves single-branch phase velocity estimates, notable bias in the final measurements still remain, even for relatively clean and simple synthetic examples. In some cases, the remaining bias is larger than the standard deviation in the corrected phase velocity estimates (Figures 4.10, 4.11a). For this reason, applications of this approach to real data should utilize highly conservative estimates for the error in the phase velocity estimates when they are utilized in subsequent analysis, inversion, or interpretation. This reflects the fact that, regardless of the efficacy of any particular analysis scheme, the estimates of phase velocity from a waveform with strong mode interference are significantly less certain than those made in the presence of little or no interference. Based on our synthetic tests, we expect that standard errors of at least 1% of the phase velocity should be assumed prior to subsequent interpretation.

4.5 Conclusion

Array-based Love-wave phase-velocity measurements can be significantly biased by the interference of the fundamental mode and overtones. We develop a strategy to correct this bias, by taking advantage of the coherence between the apparent phase velocity and the amplitude Laplacian term. The correction has a similar form to the Helmholtz equation, except that the amplitude correction term is multiplied by a constant α. The value of α can be either estimated from a reference velocity model or inverted from the data. Synthetic tests show that the correction significantly reduces the variation of phase velocity measurements due to overtone interference, and moves the average value closer to the true phase velocity. However, careful data selection and array design are needed to apply it to real data.

Acknowledgments

The software MINEOS published and maintained by CIG is used to generate synthetic seismic waveforms in this study.

Chapter 5

Concluding Remarks

In this dissertation, we develop several new surface-wave measuring methods and apply them on different datasets to understand local tectonic structures.

In Chapter 2, we develop the Automated Surface-Wave Measuring System (ASWMS), which can retrieve surface-wave phase velocities from dense-array data without human intervention. We produce robust Rayleigh-wave phase-velocity maps of the US continent at the periods of 20-100s using the USArray data, and work with IRIS to provide weekly-updated results for the scientific community and the general public. The phase-velocity maps clearly outline the major geological structures in the US continent. The spectral analysis of these maps implies that in the upper mantle, thermal variation affects shear velocity more than compositional variations.

In Chapter 3, we apply surface-wave analysis in the region near the D'Entrecasteaux Islands, Papua New Guinea. We retrieve phase-velocity variations using both ambient-noise and earthquake signals. The phase velocities in a broad period range (10-60 s) are inverted for the shear-velocity structure in the crust and the upper mantle. The results imply the existence of un-exhumed crustal material and/or partial melt in the shallow mantle west of the most recently exhumed UHP rocks on Goodenough Island.

In Chapter 4, we focus on the effect of Love-wave overtone interference on the array-based phase-velocity measurements. We simulate the interference pattern by two plane waves travelling together at different phase velocities. We also develop a correction scheme

that can significantly reduce the phase-velocity bias and variance due to the interference.

References

Abers, G. A., A. Ferris, M. Craig, H. Davies, A. L. Lerner-Lam, J. C. Mutter, and B. Taylor (2002), Mantle compensation of active metamorphic core complexes at Woodlark rift in Papua New Guinea, *Nature*, *418*(6900), 862–865.

Abers, G. A., Y. Kim, J. B. Gaherty, Z. Eilon, G. Jin, and R. Verave (2012), Imaging to understand exhumation of UHP rocks during rifting: the 2010-2011 CDPapua seismic experiment, in *AGU Fall Meeting Abstracts*.

Aki, K. (1957), Space and time spectra of stationary stochastic waves, with special reference to microtremors, *Bull. Earthquake Res. Inst. Univ. Tokyo*, (35), 415–456.

Antonsen, T., and E. Ott (1991), Multifractal power spectra of passive scalars convected by chaotic fluid flows, *Physical Review A*, *44*(2), 851–857, doi:10.1103/PhysRevA.44.851.

Bailey, I. W., M. S. Miller, K. Liu, and A. Levander (2012), VS and density structure beneath the Colorado Plateau constrained by gravity anomalies and joint inversions of receiver function and phase velocity data, *J. Geophys. Res.: Solid Earth*, *117*(B2), B02,313, doi: 10.1029/2011JB008522.

Baldwin, S. L., G. S. Lister, E. J. Hill, D. A. Foster, and I. McDougall (1993), Thermochronologic constraints on the tectonic evolution of active metamorphic core complexes, D'entrecasteaux Islands, Papua New Guinea, *Tectonics*, *12*(3), 611–628, doi: 10.1029/93TC00235.

Baldwin, S. L., B. D. Monteleone, L. E. Webb, P. G. Fitzgerald, M. Grove, and E. J. Hill (2004), Pliocene eclogite exhumation at plate tectonic rates in eastern Papua New Guinea, *Nature*, *431*(7006), 263–267.

Baldwin, S. L., L. E. Webb, and B. D. Monteleone (2008), Late Miocene coesite-eclogite exhumed in the Woodlark Rift, *Geology*, *36*(9), 735–738, doi:10.1130/G25144A.1.

Baldwin, S. L., P. G. Fitzgerald, and L. E. Webb (2012), Tectonics of the New Guinea Region, *Annu. Rev. Earth Planet. Sci.*, *40*(1), 495–520, doi:10.1146/annurev-earth-040809-152540.

Bastow, I. D., S. Pilidou, J. M. Kendall, and G. W. Stuart (2010), Melt-induced seismic anisotropy and magma assisted rifting in Ethiopia: Evidence from surface waves, *Geochem. Geophys. Geosyst.*, *11*(6), doi:10.1029/2010GC003036.

Batchelor, G. K. (1959), Small-scale variation of convected quantities like temperature in turbulent fluid Part 1. General discussion and the case of small conductivity, *Journal of Fluid Mechanics*, *5*(01), 113–133, doi:10.1017/S002211205900009X.

Bensen, G. D., M. H. Ritzwoller, M. P. Barmin, A. L. Levshin, F. Lin, M. P. Moschetti, N. M. Shapiro, and Y. Yang (2007), Processing seismic ambient noise data to obtain reliable broad-band surface wave dispersion measurements, *Geophys. J. Int*, *169*(3), 1239–1260, doi:10.1111/j.1365-246X.2007.03374.x.

Bodin, T., and V. Maupin (2008), Resolution potential of surface wave phase velocity measurements at small arrays, *Geophys. J. Int*, *172*(2), 698–706, doi:10.1111/j.1365-246X.2007.03668.x.

Braun, M. (2000), The effects of deep damp melting on mantle flow and melt generation beneath mid-ocean ridges, *Earth Planet. Sci. Lett.*, *176*(3-4), 339–356, doi:10.1016/S0012-821X(00)00015-7.

Brisbourne, A. M., and G. W. Stuart (1998), Shear-wave velocity structure beneath North Island, New Zealand, from Rayleigh-wave interstation phase velocities, *Geophys. J. Int*, *133*(1), 175–184, doi:10.1046/j.1365-246X.1998.1331485.x.

Brownlee, S. J., B. R. Hacker, M. Salisbury, G. Seward, T. A. Little, S. L. Baldwin, and G. A. Abers (2011), Predicted velocity and density structure of the exhuming Papua New Guinea ultrahigh-pressure terrane, *J. Geophys. Res.*, *116*(B8), B08,206, doi:10.1029/2011JB008195.

Calkins, J. A., G. A. Abers, G. Ekström, K. C. Creager, and S. Rondenay (2011), Shallow structure of the Cascadia subduction zone beneath western Washington from spectral ambient noise correlation, *J. Geophys. Res.: Solid Earth*, *116*(B7), B07,302, doi:10.1029/2010JB007657.

Chen, P., L. Zhao, and T. H. Jordan (2007), Full 3D Tomography for the Crustal Structure of the Los Angeles Region, *Bull. Seismol. Soc. Am.*, *97*(4), 1094–1120, doi:10.1785/0120060222.

Chevrot, S., J. P. Montagner, and R. Snieder (1998), The spectrum of tomographic earth models, *Geophys. J. Int*, *133*(3), 783–788, doi:10.1046/j.1365-246X.1998.00542.x.

Christensen, N. I., and W. D. Mooney (1995), Seismic velocity structure and composition of the continental crust: A global view, *J. Geophys. Res.: Solid Earth*, *100*(B6), 9761–9788, doi:10.1029/95JB00259.

Cox, H. (1973), Spatial correlation in arbitrary noise fields with application to ambient sea noise, *J. Acoust. Soc. Am.*, *54*(5), 1289, doi:10.1121/1.1914426.

Crotwell, H. P., and T. J. Owens (2005), Automated Receiver Function Processing, *Seismol.*

Res. Lett., *76*(6), 702–709, doi:10.1785/gssrl.76.6.702.

Daczko, N. R., P. Caffi, and P. Mann (2011), Structural evolution of the Dayman dome metamorphic core complex, eastern Papua New Guinea, *Geol. Soc. Am. Bull.*, *123*(11-12), 2335–2351, doi:10.1130/B30326.1.

Dalton, C. A., G. Ekström, and A. M. Dziewoński (2009), Global seismological shear velocity and attenuation: A comparison with experimental observations, *Earth Planet. Sci. Lett.*, *284*(1-2), 65–75, doi:10.1016/j.epsl.2009.04.009.

Dalton, C. A., C. H. Langmuir, and A. Gale (2014), Geophysical and Geochemical Evidence for Deep Temperature Variations Beneath Mid-Ocean Ridges, *Science*, *344*(6179), 80–83, doi:10.1126/science.1249466.

Davies, H. L., and R. G. Warren (1988), Origin of eclogite-bearing, domed, layered metamorphic complexes ("core complexes") in the D'entrecasteaux Islands, Papua New Guinea, *J. geophys. Res*, *7*(1), 1, doi:10.1029/TC007i001p00001.

Dieck, C. C., G. A. Abers, Z. Eilon, J. B. Gaherty, and R. Verave (2013), Seismicity in an active rift exposing ultra-high pressure metamorphic rocks: D'Entrecasteaux Islands, Papua New Guinea, *AGU Fall Meeting Abstracts*, *-1*, 2524–2524.

Dugda, M. T., A. A. Nyblade, and J. Julia (2007), Thin Lithosphere Beneath the Ethiopian Plateau Revealed by a Joint Inversion of Rayleigh Wave Group Velocities and Receiver Functions, *J. Geophys. Res.*, *112*(B8), B08,305, doi:10.1029/2006JB004918.

Dziewonski, A. M., and D. L. Anderson (1981), Preliminary reference Earth model, *Phys. Earth Planet. Inter.*, *25*(4), 297–356, doi:10.1016/0031-9201(81)90046-7.

Dziewonski, A. M., T. A. Chou, and J. H. Woodhouse (1981), Determination of earthquake source parameters from waveform data for studies of global and regional seismicity, *J. Geophys. Res.*, *86*(B4), 2825–2852, doi:10.1029/JB086iB04p02825.

Dziewoński, A. M., V. Lekic, and B. A. Romanowicz (2010), Mantle Anchor Structure: An argument for bottom up tectonics, *Earth Planet. Sci. Lett.*, *299*(1-2), 69–79, doi:10.1016/j.epsl.2010.08.013.

Eddy, C. L., and G. Ekström (2014), Local amplification of Rayleigh waves in the continental United States observed on the USArray, *Earth Planet. Sci. Lett.*, *402*, 50–57, doi:10.1016/j.epsl.2014.01.013.

Eilon, Z., G. A. Abers, and G. Jin (2014), Anisotropy beneath a highly extended continental rift, *Geochem. Geophys. Geosyst.*, *15*(3), 545–564, doi:10.1002/2013GC005092.

Eilon, Z., G. A. Abers, J. B. Gaherty, and G. Jin (2015), A Joint Inversion for Velocity and Anisotropy Structure Beneath a Highly Extended Continental Rift, *Geochem. Geophys. Geosyst.*, *submitted*.

Ekström, G. (2013), Love and Rayleigh phase-velocity maps, 5–40 s, of the western and central USA from USArray data, *Earth Planet. Sci. Lett.*, *402*, 42–49, doi:10.1016/j.epsl.2013.11.022.

Ekström, G., J. Tromp, and E. W. F. Larson (1997), Measurements and global models of surface wave propagation, *J. Geophys. Res.: Solid Earth*, *102*(B4), 8137–8157, doi:10.1029/96JB03729.

Ekström, G., G. A. Abers, and S. C. Webb (2009), Determination of surface-wave phase velocities across USArray from noise and Aki's spectral formulation, *Geophys. Res. Lett.*, *36*(18), L18,301, doi:10.1029/2009GL039131.

Ekström, G., M. Nettles, and A. M. Dziewonski (2012), The global CMT project 2004–2010: Centroid-moment tensors for 13,017 earthquakes, *Phys. Earth Planet. Inter.*, *200-201*, 1–9, doi:10.1016/j.pepi.2012.04.002.

Ellis, S. M., T. A. Little, L. M. Wallace, B. R. Hacker, and S. J. H. Buiter (2011), Feedback between rifting and diapirism can exhume ultrahigh-pressure rocks, *Earth Planet. Sci. Lett.*, *311*(3-4), 427–438, doi:10.1016/j.epsl.2011.09.031.

Evernden, J. F. (1954), Direction of approach of rayleigh waves and related problems (Part II), *Bull. Seismol. Soc. Am.*, *44*(2A), 159–184.

Ferris, A., G. A. Abers, B. Zelt, B. Taylor, and S. Roecker (2006), Crustal structure across the transition from rifting to spreading: the Woodlark rift system of Papua New Guinea, *Geophys. J. Int*, *166*(2), 622–634.

Finlayson, D. M., K. J. Muirhead, J. P. Webb, G. Gibson, A. S. Furumoto, R. J. S. Cooke, and A. J. Russell (1976), Seismic Investigation of the Papuan Ultramafic Belt, *Geophys. J. Int*, *44*(1), 45–59, doi:10.1111/j.1365-246X.1976.tb00274.x.

Finlayson, D. M., B. J. Drummond, C. Collins, and J. B. Connelly (1977), Crustal structures in the region of the Papuan Ultramafic Belt, *Phys. Earth Planet. Inter.*, *14*(1), 13–29.

Fischer, K. M. (2002), Waning buoyancy in the crustal roots of old mountains, *Nature*, *417*, 933–936.

Fitz, G., and P. Mann (2013), Tectonic uplift mechanism of the goodenough and Fergusson Island gneiss domes, eastern Papua New Guinea: Constraints from seismic reflection and well data, *Geochem. Geophys. Geosyst.*, *14*(10), 3969–3995, doi:10.1002/ggge.20208.

Forsyth, D. W. (1975), A new method for the analysis of multi-mode surface-wave dispersion: Application to Love-wave propagation in the east Pacific, *Bull. Seismol. Soc. Am.*, *65*(2), 323–342.

Forsyth, D. W., and A. Li (2005), Array analysis of two-dimensional variations in surface wave phase velocity and azimuthal anisotropy in the presence of multipathing interference,

in *Seismic Earth Array Analysis of Broadband Seismograms. AGU Geophysical Monograph Series.*, edited by L. A and N. G, pp. 81–98, doi:10.1029/156GM06.

Foster, A., G. Ekström, and M. Nettles (2014a), Surface wave phase velocities of the Western United States from a two-station method, *Geophys. J. Int*, *196*(2), 1189–1206, doi:10.1093/gji/ggt454.

Foster, A., M. Nettles, and G. Ekström (2014b), Overtone Interference in Array-Based Love-Wave Phase Measurements, *Bull. Seismol. Soc. Am.*, *104*(5), 2266–2277, doi:10.1785/0120140100.

Foti, S., C. Comina, D. Boiero, and L. V. Socco (2009), Non-uniqueness in surface-wave inversion and consequences on seismic site response analyses, *Soil Dynamics and Earthquake ...*.

Friederich, W., and E. Wielandt (1995), Interpretation of seismic surface waves in regional networks: joint estimation of wavefield geometry and local phase velocity. Method and numerical tests, *Geophys. J. Int*, *120*(3), 731–744, doi:10.1111/j.1365-246X.1995.tb01849.x.

Gaherty, J. B. (2001), Seismic Evidence for Hotspot-Induced Buoyant Flow Beneath the Reykjanes Ridge, *Science*, *293*(5535), 1645–1647, doi:10.1126/science.1061565.

Gaherty, J. B. (2004), A surface wave analysis of seismic anisotropy beneath eastern North America, *Geophys. J. Int*, *158*(3), 1053–1066, doi:10.1111/j.1365-246X.2004.02371.x.

Gaherty, J. B., and R. A. Dunn (2007), Evaluating hot spot-ridge interaction in the Atlantic from regional-scale seismic observations, *Geochem. Geophys. Geosyst.*, *8*(5), doi:10.1029/2006GC001533.

Gaherty, J. B., and T. H. Jordan (1995), Lehmann Discontinuity as the Base of an Anisotropic Layer Beneath Continents, *Science*, *268*(5216), 1468–1471, doi:10.1126/science.268.5216.1468.

Gaherty, J. B., T. H. Jordan, and L. S. Gee (1996), Seismic structure of the upper mantle in a central Pacific corridor, *J. Geophys. Res.*, *101*(B10), 22,291–22,309.

Gao, W., S. P. Grand, W. S. Baldridge, D. Wilson, M. West, J. F. Ni, and R. Aster (2004), Upper mantle convection beneath the central Rio Grande rift imaged by P and S wave tomography, *J. Geophys. Res.: Solid Earth*, *109*(B3), B03,305, doi:10.1029/2003JB002743.

Gazel, E., T. Plank, D. W. Forsyth, C. Bendersky, C. T. A. Lee, and E. H. Hauri (2012), Lithosphere versus asthenosphere mantle sources at the Big Pine Volcanic Field, California, *Geochem. Geophys. Geosyst.*, *13*(6), Q0AK06, doi:10.1029/2012GC004060.

Gee, L. S., and T. H. Jordan (1992), Generalized seismological data functionals, *Geophys. J. Int*, *111*(2), 363–390.

Goodliffe, A. M., and B. Taylor (2007), The boundary between continental rifting and seafloor spreading in the Woodlark Basin, Papua New Guinea, *Geological Society, London, Special Publications*, *282*(1), 217–238, doi:10.1144/SP282.11.

Gordon, S. M., T. A. Little, B. R. Hacker, S. A. Bowring, M. Korchinski, S. L. Baldwin, and A. R. C. Kylander-Clark (2012), Multi-stage exhumation of young UHP–HP rocks: Timescales of melt crystallization in the D'Entrecasteaux Islands, southeastern Papua New Guinea, *Earth Planet. Sci. Lett.*, *351-352*, 237–246, doi:10.1016/j.epsl.2012.07.014.

Grand, S. P., and D. V. Helmberger (1984), Upper mantle shear structure of North America, *Geophysical Journal International*, *76*(2), 399–438, doi:10.1111/j.1365-246X.1984.tb05053.x.

Gu, Y. J., S. C. Webb, A. L. Lam, and J. B. Gaherty (2005), Upper mantle structure beneath the eastern Pacific Ocean ridges, *J. Geophys. Res.*, *110*(B06305), doi:10.1029/2004JB003381.

Hammond, W. C., and E. D. Humphreys (2000), Upper mantle seismic wave velocity: Effects of realistic partial melt geometries, *J. Geophys. Res.: Solid Earth*, *105*(B5), 10,975–10,986.

Herrmann, R. B. (2013), Computer Programs in Seismology: An Evolving Tool for Instruction and Research, *Seismol. Res. Lett.*, *84*(6), 1081–1088, doi:10.1785/0220110096.

Herrmann, R. B., and C. J. Ammon (2004), Computer Programs in Seismology: Surface Waves, Receiver Functions, and Crustal Structure.

Hill, E. J., S. L. Baldwin, and G. S. Lister (1992), Unroofing of active metamorphic core complexes in the D'Entrecasteaux Islands, Papua New Guinea, *Geology*, *20*(10), 907–910, doi:10.1130/0091-7613(1992).

Holtzman, B. K., and J. Kendall (2010), Organized melt, seismic anisotropy, and plate boundary lubrication, *Geochemistry*, doi:10.1029/2010GC003296.

Jackson, I., and U. H. Faul (2010), Grainsize-sensitive viscoelastic relaxation in olivine: Towards a robust laboratory-based model for seismological application, *Phys. Earth Planet. Inter.*, *183*(1-2), 151–163, doi:10.1016/j.pepi.2010.09.005.

Jin, G., and J. B. Gaherty (2015), Surface wave phase-velocity tomography based on multichannel cross-correlation, *Geophys. J. Int*, *201*(3), 1383–1398, doi:10.1093/gji/ggv079.

Keranen, K. M., S. L. KLEMPERER, J. Julia, J. F. Lawrence, and A. A. Nyblade (2009), Low lower crustal velocity across Ethiopia: Is the Main Ethiopian Rift a narrow rift in a hot craton?, *Geochem. Geophys. Geosyst.*, *10*(5), doi:10.1029/2008GC002293.

Knopoff, L., S. Mueller, and W. L. Pilant (1966), Structure of the crust and upper mantle in the Alps from the phase velocity of Rayleigh waves, *Bull. Seismol. Soc. Am.*, *56*(5), 1009–1044.

Landisman, M., A. Dziewonski, and Y. Satô (1969), Recent Improvements in the Analysis of Surface Wave Observations, *Geophys. J. Int*, *17*(4), 369–403, doi:10.1111/j.1365-246X.1969.tb00246.x.

Laske, G., and G. Masters (1997), A Global Digital Map of Sediment Thickness, *Eos Trans. AGU*, *78*, F483, doi:10.1029/97JB02622/full.

Lee, C. T., Q. Yin, R. L. Rudnick, and S. B. Jacobsen (2001), Preservation of ancient and fertile lithospheric mantle beneath the southwestern United States, *Nature*, *411*(6833), 69–73, doi:10.1038/35075048.

Levander, A., B. Schmandt, M. S. Miller, K. Liu, K. E. Karlstrom, R. S. Crow, C. T. Lee, and E. D. Humphreys (2011), Continuing Colorado plateau uplift by delamination-style convective lithospheric downwelling, *Nature*, *472*(7344), 461–465, doi:10.1038/nature10001.

Levandowski, W., C. H. Jones, W. Shen, M. H. Ritzwoller, and V. Schulte Pelkum (2014), Origins of topography in the western U.S.: Mapping crustal and upper mantle density variations using a uniform seismic velocity model, *J. Geophys. Res.: Solid Earth*, *119*(3), 2375–2396, doi:10.1002/2013JB010607.

Levshin, A., L. Ratnikova, and J. Berger (1992), Peculiarities of surface-wave propagation across central Eurasia, *Bull. Seismol. Soc. Am.*, *82*(6), 2464–2493.

Levshin, A. L., and M. H. Ritzwoller (2001), Automated Detection, Extraction, and Measurement of Regional Surface Waves, in *Monitoring the Comprehensive Nuclear-Test-Ban Treaty Surface Waves*, edited by A. L. Levshin and M. H. Ritzwoller, pp. 1531–1545, Birkhäuser Basel, Basel, doi:10.1007/978-3-0348-8264-4_11.

Li, A., K. M. Fischer, S. van der Lee, and W. M. E (2002), Crust and upper mantle discontinuity structure beneath eastern North America, *J. Geophys. Res.*, *107*(B5), doi:10.1029/2001JB000190.

Li, X. D., and B. Romanowicz (1996), Global mantle shear velocity model developed using nonlinear asymptotic coupling theory, *J. Geophys. Res.: Solid Earth*, *101*(B10), 22,245–22,272, doi:10.1029/96JB01306.

Lin, F.-C., and M. H. Ritzwoller (2011), Helmholtz surface wave tomography for isotropic and azimuthally anisotropic structure, *Geophys. J. Int*, *186*(3), 1104–1120, doi:10.1111/j.1365-246X.2011.05070.x.

Lin, F.-C., M. H. Ritzwoller, and R. Snieder (2009), Eikonal tomography: surface wave tomography by phase front tracking across a regional broad-band seismic array, *Geophys. J. Int*, *177*(3), 1091–1110, doi:10.1111/j.1365-246X.2009.04105.x.

Lin, F.-C., V. C. Tsai, and M. H. Ritzwoller (2012), The local amplification of surface waves: A new observable to constrain elastic velocities, density, and anelastic attenuation,

J. geophys. Res, *117*(B6), B06,302, doi:10.1029/2012JB009208.

Little, T. A., B. R. Hacker, S. M. Gordon, S. L. Baldwin, P. G. Fitzgerald, S. Ellis, and M. Korchinski (2011), Diapiric exhumation of Earth's youngest (UHP) eclogites in the gneiss domes of the D'Entrecasteaux Islands, Papua New Guinea, *Tectonophysics*, *510*(1-2), 39–68, doi:10.1016/j.tecto.2011.06.006.

Lizarralde, D., J. B. Gaherty, J. A. Collins, G. Hirth, and S. D. Kim (2004), Spreading-rate dependence of melt extraction at mid-ocean ridges from mantle seismic refraction data, *Nature*, *432*(7018), 744–747, doi:10.1038/nature03140.

Lus, W. Y., I. McDougall, and H. L. Davies (2004), Age of the metamorphic sole of the Papuan Ultramafic Belt ophiolite, Papua New Guinea, *Tectonophysics*, *392*(1-4), 85–101, doi:10.1016/j.tecto.2004.04.009.

Lysak, S. V. (1992), Heat flow variations in continental rifts, *Tectonophysics*, *208*(1-3), 309–323, doi:10.1016/0040-1951(92)90352-7.

Malusà, M. G., C. Faccenna, S. L. Baldwin, P. G. Fitzgerald, F. Rossetti, M. Laura Balestrieri, M. Danišík, A. Ellero, G. Ottria, and C. Piromallo (2015), Contrasting styles of (U)HP rock exhumation along the Cenozoic Adria-Europe plate boundary (Western Alps, Calabria, Corsica), *Geochem. Geophys. Geosyst.*, doi:10.1002/2015GC005767.

Martinez, F., and B. Taylor (1996), Backarc spreading, rifting, and microplate rotation, between transform faults in the Manus Basin, *Mar. Geophys. Res.*, *18*(2-4), 203–224, doi:10.1007/BF00286078.

Martinez, F., A. M. Goodliffe, and B. Taylor (2001), Metamorphic core complex formation by density inversion and lower-crust extrusion, *Nature*, doi:10.1038/35082042.

Menke, W., and G. Jin (2015), Waveform Fitting of Cross Spectra to Determine Phase Velocity Using Aki's Formula, *Bull. Seismol. Soc. Am.*

Monteleone, B. D., S. L. Baldwin, and L. E. Webb (2007), Late Miocene–Pliocene eclogite facies metamorphism, D'Entrecasteaux Islands, SE Papua New Guinea, *J. Metamorph. Geol.*, doi:10.1111/j.1525-1314.2006.00685.x.

Nettles, M., and A. M. Dziewoński (2008), Radially anisotropic shear velocity structure of the upper mantle globally and beneath North America, *J. Geophys. Res.*, *113*(B2), B02,303, doi:10.1029/2006JB004819.

Nettles, M., and A. M. Dziewoński (2011), Effect of Higher-Mode Interference on Measurements and Models of Fundamental-Mode Surface-Wave Dispersion, *Bull. Seismol. Soc. Am.*, *101*(5), 2270–2280, doi:10.1785/0120110019.

Nishimura, C. E., and D. W. Forsyth (1989), The anisotropic structure of the upper mantle in the Pacific, *Geophys. J. Int*, *96*(2), 203–229, doi:10.1111/j.1365-246X.1989.tb04446.x.

Obrebski, M., G. A. Abers, G. Jin, and Z. Eilon (2014), Rift Structure in Eastern Papua New Guinea From the Joint Inversion of Receiver Functions and Seismic Noise, in *AGU Fall Meeting Abstracts*.

Owens, T. J., H. P. Crotwell, C. Groves, and P. Oliver-Paul (2004), SOD: standing order for data, *Seismol. Res. Lett.*, *75*(4), 515–520, doi:10.1785/gssrl.75.4.515-a.

Parker, E. H., R. B. Hawman, K. M. Fischer, and L. S. Wagner (2013), Crustal evolution across the southern Appalachians: Initial results from the SESAME broadband array, *Geophys. Res. Lett.*, *40*(15), 3853–3857, doi:10.1002/grl.50761.

Peng, X., and E. D. Humphreys (1998), Crustal velocity structure across the eastern Snake River Plain and the Yellowstone swell, *J. Geophys. Res.: Solid Earth*, *103*(B4), 7171–7186, doi:10.1029/97JB03615.

Pollitz, F. F., and J. A. Snoke (2010), Rayleigh-wave phase-velocity maps and three-dimensional shear velocity structure of the western US from local non-plane surface wave tomography, *Geophys. J. Int*, *180*(3), 1153–1169, doi:10.1111/j.1365-246X.2009.04441.x.

Priestley, K., and D. McKenzie (2013), Earth and Planetary Science Letters, *Earth Planet. Sci. Lett.*, *381*(C), 78–91, doi:10.1016/j.epsl.2013.08.022.

Rau, C. J., and D. W. Forsyth (2011), Melt in the mantle beneath the amagmatic zone, southern Nevada, *Geology*, *39*(10), 975–978, doi:10.1130/G32179.1.

Reston, T. (2007), Extension discrepancy at North Atlantic nonvolcanic rifted margins: Depth-dependent stretching or unrecognized faulting?, *Geology*, *35*(4), 367–370, doi:10.1130/G23213A.1.

Ricard, Y., S. Durand, J. P. Montagner, and F. Chambat (2014), Is there seismic attenuation in the mantle?, *Earth Planet. Sci. Lett.*, *388*(C), 257–264, doi:10.1016/j.epsl.2013.12.008.

Roy, M., T. H. Jordan, and J. Pederson (2009), Colorado Plateau magmatism and uplift by warming of heterogeneous lithosphere, *Nature*, *459*(7249), 978–982, doi:10.1038/nature08052.

Rychert, C. A., K. M. Fischer, and S. Rondenay (2005), A sharp lithosphere–asthenosphere boundary imaged beneath eastern North America, *Nature*, *436*(7050), 542–545, doi:10.1038/nature03904.

Saltzer, R. L., and E. D. Humphreys (1997), Upper mantle P wave velocity structure of the eastern Snake River Plain and its relationship to geodynamic models of the region, *J. Geophys. Res.: Solid Earth*, *102*(B6), 11,829–11,841, doi:10.1029/97JB00211.

Schaff, D. P., and G. C. Beroza (2004), Coseismic and postseismic velocity changes measured by repeating earthquakes, *J. Geophys. Res.: Solid Earth*, *109*(B10), B10,302, doi:10.1029/2004JB003011.

Schmeling, H., and H. Wallner (2012), Magmatic lithospheric heating and weakening during continental rifting: A simple scaling law, a 2-D thermomechanical rifting model and the East African Rift System, *Geochem. Geophys. Geosyst.*, *13*(8), doi:10.1029/2012GC004178.

Shapiro, N. M., M. Campillo, L. Stehly, and M. H. Ritzwoller (2005), High-Resolution Surface-Wave Tomography from Ambient Seismic Noise, *Science*, *307*(5715), 1615–1618, doi:10.1126/science.1108339.

Shen, W., M. H. Ritzwoller, and V. Schulte Pelkum (2013a), Crustal and uppermost mantle structure in the central U.S. encompassing the Midcontinent Rift, *J. Geophys. Res.: Solid Earth*, *118*(8), 4325–4344, doi:10.1002/jgrb.50321.

Shen, W., M. H. Ritzwoller, and V. Schulte Pelkum (2013b), A 3-D model of the crust and uppermost mantle beneath the Central and Western US by joint inversion of receiver functions and surface wave dispersion, *J. Geophys. Res.: Solid Earth*, *118*(1), 262–276, doi:10.1029/2012JB009602.

Shillington, D. J., W. S. Holbrook, H. J. A. Van Avendonk, B. E. Tucholke, J. R. Hopper, K. E. Louden, H. C. Larsen, and G. T. Nunes (2006), Evidence for asymmetric nonvolcanic rifting and slow incipient oceanic accretion from seismic reflection data on the Newfoundland margin, *J. Geophys. Res.*, *111*(B9), B09,402–23, doi:10.1029/2005JB003981.

Smith, I. E. (1976), Volcanism in Australasia, pp. 275–286.

Smith, I. E., and H. L. Davies (1976), *Geology of the southeast Papuan mainland*, Australian Government Publishing Service for the Bureau of Mineral Resources, Geology and Geophysics.

Sparlin, M. A., L. W. Braile, and R. B. Smith (1982), Crustal structure of the Eastern Snake River Plain determined from ray trace modeling of seismic refraction data, *J. Geophys. Res.: Solid Earth*, *87*(B4), 2619–2633, doi:10.1029/JB087iB04p02619.

Takei, Y. (2002), Effect of pore geometry on VP/VS: From equilibrium geometry to crack, *J. Geophys. Res.*, *107*(B2), ECV 6–1–ECV 6–12, doi:10.1029/2001JB000522.

Takei, Y., and B. K. Holtzman (2009), Viscous constitutive relations of solid-liquid composites in terms of grain boundary contiguity: 1. Grain boundary diffusion control model, *J. Geophys. Res.*, *114*(B6), B06,205, doi:10.1029/2008JB005850.

Tape, C., Q. Liu, A. Maggi, and J. Tromp (2010), Seismic tomography of the southern California crust based on spectral-element and adjoint methods, *Geophys. J. Int*, *180*(1), 433–462, doi:10.1111/j.1365-246X.2009.04429.x.

Taylor, B., and P. Huchon (2002), Active continental extension in the western Woodlark Basin: a synthesis of Leg 180 results, in *Proceedings of the Ocean Drilling Program, Sci-*

entific Results, pp. 1–36, US Gov. Print. Off. Washington, DC.

Taylor, B., A. M. Goodliffe, and F. Martinez (1999), How continents break up: insights from Papua New Guinea, *J. Geophys. Res.*, *104*(B4), 7497–7512.

Thatcher, W., and J. N. Brune (1969), Higher mode interference and observed anomalous apparent Love wave phase velocities, *J. Geophys. Res.*, *74*(27), 6603–6611, doi:10.1029/JB074i027p06603.

Tian, Y., and M. H. Ritzwoller (2015), Directionality of ambient noise on the Juan de Fuca plate: implications for source locations of the primary and secondary microseisms, *Geophysical Journal International*, *201*(1), 429–443, doi:10.1093/gji/ggv024.

VanDecar, J. C., and R. S. Crosson (1990), Determination of teleseismic relative phase arrival times using multi-channel cross-correlation and least squares, *Bull. Seismol. Soc. Am.*, *80*(1), 150–169.

Walck, M. C. (1984), The P-wave upper mantle structure beneath an active spreading centre: the Gulf of California, *Geophysical Journal International*, *76*(3), 697–723, doi:10.1111/j.1365-246X.1984.tb01918.x.

Wallace, L. M. (2004), GPS and seismological constraints on active tectonics and arc-continent collision in Papua New Guinea: Implications for mechanics of microplate rotations in a plate boundary zone, *J. Geophys. Res.*, *109*(B5), B05,404, doi:10.1029/2003JB002481.

Wallace, L. M., S. Ellis, T. Little, P. Tregoning, N. Palmer, R. Rosa, R. Stanaway, J. Oa, E. Nidkombu, and J. Kwazi (2014), Continental breakup and UHP rock exhumation in action: GPS results from the Woodlark Rift, Papua New Guinea, *Geochem. Geophys. Geosyst.*, pp. 4267–4290, doi:10.1002/2014GC005458.

Webb, L. E., S. L. Baldwin, T. A. Little, and P. G. Fitzgerald (2008), Can microplate rotation drive subduction inversion?, *Geology*, *36*(10), 823–826, doi:10.1130/G25134A.1.

Webb, L. E., S. L. Baldwin, and P. G. Fitzgerald (2014), The Early-Middle Miocene subduction complex of the Louisiade Archipelago, southern margin of the Woodlark Rift, *Geochem. Geophys. Geosyst.*, *15*(10), 4024–4046, doi:10.1002/2014GC005500.

Wei, S. S., D. A. Wiens, Y. Zha, T. Plank, S. C. Webb, D. K. Blackman, R. A. Dunn, and J. A. Conder (2015), Seismic evidence of effects of water on melt transport in the Lau back-arc mantle, *Nature*, *518*(7539), 395–398, doi:10.1038/nature14113.

Wielandt, E. (1993), Propagation and Structural Interpretation of Non-Plane Waves, *Geophys. J. Int*, *113*(1), 45–53.

Yang, Y., and D. W. Forsyth (2006), Regional tomographic inversion of the amplitude and phase of Rayleigh waves with 2-D sensitivity kernels, *Geophys. J. Int*, *166*(3), 1148–1160,

doi:10.1111/j.1365-246X.2006.02972.x.

Yang, Y., and M. H. Ritzwoller (2008), Teleseismic surface wave tomography in the western U.S. using the Transportable Array component of USArray, *Geophys. Res. Lett.*, *35*(4), L04,308, doi:10.1029/2007GL032278.

Yang, Y., W. Shen, and M. H. Ritzwoller (2011), Surface wave tomography on a large-scale seismic array combining ambient noise and teleseismic earthquake data, *Earthquake Science*, *24*(1), 55–64, doi:10.1007/s11589-011-0769-3.

Yao, H., G. Xu, L. Zhu, and X. Xiao (2005), Mantle structure from inter-station Rayleigh wave dispersion and its tectonic implication in western China and neighboring regions, *Phys. Earth Planet. Inter.*, *148*(1), 39–54, doi:10.1016/j.pepi.2004.08.006.

Zandt, G., S. C. Myers, and T. C. Wallace (1995), Crust and mantle structure across the Basin and Range-Colorado Plateau boundary at 37 N latitude and implications for Cenozoic extensional mechanism, *J. Geophys. Res.: Solid Earth*, *100*(B6), 10,529–10,548.

Zhou, Y., F. A. Dahlen, G. Nolet, and G. Laske (2005), Finite-frequency effects in global surface-wave tomography, *Geophysical Journal International*, *163*(3), 1087–1111, doi:10.1111/j.1365-246X.2005.02780.x.

Zhou, Y., G. Nolet, and F. A. Dahlen (2006), Global upper-mantle structure from finite-frequency surface-wave tomography, *Journal of Geophysical ...*, *111*(B4), B04,304, doi:10.1029/2005JB003677.

Zhu, H., E. Bozdağ, D. Peter, and J. Tromp (2012), Structure of the European upper mantle revealed by adjoint tomography, *Nature Geoscience*, *5*(7), 493–498, doi:10.1038/ngeo1501.

Zhu, L., and H. Kanamori (2000), Moho depth variation in southern California from teleseismic receiver functions, *J. Geophys. Res.*, *105*(B2), 2969–2980, doi:10.1029/1999JB900322.

Zirakparvar, N. A., S. L. Baldwin, and J. D. Vervoort (2011), Lu–Hf garnet geochronology applied to plate boundary zones: Insights from the (U)HP terrane exhumed within the Woodlark Rift, *Earth Planet. Sci. Lett.*, *309*(1-2), 56–66, doi:10.1016/j.epsl.2011.06.016.